

Elevated Temperature Biaxial Fatigue

Eric H. Jordan
*University of Connecticut
Storrs, Connecticut*



October 1985

Prepared for the
Lewis Research Center
Under Contract NAG 3-160

TABLE OF CONTENTS

	Page
I. INTRODUCTION	1
II. THEORIES OF MULTIAXIAL FATIGUE	3
a. Gamma Plane Theory of Brown and Miller.	4
b. Plastic Work Theory	5
c. Gamma Plane Theory of Lohr and Ellison.	6
III. PHYSICAL CONSIDERATION OF FATIGUE MECHANISM.	7
IV. EXPERIMENTAL METHODS	9
V. EXPERIMENTAL FACILITIES.	11
1. The Testing Machine	11
2. Specimen and Material	12
3. The Grips	13
4. The Heating System	13
5. Extensometer	14
6. Capacitance Ring Probes	18
7. Computer Data Acquisition System	29
VI. EXPERIMENTS AND RESULTS	30
1. Check for Anisotropy	32
2. Check the Strain Distribution on Gage Section	32
3. Check the Elastic Poisson's Ratio	33
4. Check for Strain Rate Effects	33
5. Tests Using Induction Heater	34
6. Baseline Tests	35
7. Non-Proportional Loading Tests	36
Test (a)	36

Test (b)	38
Test (c)	40
VII. CORRELATION OF MULTIAXIAL FATIGUE THEORIES . . .	43
VIII. CRACKS OBSERVATION	46
VIV. CONCLUSIONS	48
TABLES	51
FIGURES	66
APPENDIX I	149
APPENDIX II	152
REFERENCES	154

Nomenclature

$G.L.$	= gage length
E	= Young's modulus
G	= shear modulus
ν	= Poisson's ratio
λ	= applied strain ratio
ϕ	= phase angle
N_f	= fatigue life
$\Delta\epsilon$	= applied axial strain range
$\Delta\gamma$	= applied torsional strain range
ΔP	= applied axial load range
ΔT	= applied torque range
ΔS	= applied normal stress range
$\Delta\tau$	= applied shear stress range
$\Delta\epsilon_p$	= applied plastic axial strain range
$\Delta\gamma_p$	= applied plastic torsional strain range
ΔW_p^E	= axial plastic work per cycle
ΔW_p^Y	= torsional plastic work per cycle
ΔW_p	= total plastic work per cycle
ΔW_p^*	= modified total plastic work per cycle
$\Delta\gamma_{oct}$	= octahedral shear strain range
$\Delta\gamma_{max}$	= maximum shear strain range
$\Delta\gamma_{max}^P$	= maximum plastic shear strain range
$\Delta\epsilon_n$	= normal strain range on the plane of maximum shear strain range
ψ_{max}	= angle of the plane of maximum shear strain range

$\Delta\epsilon_1$	= maximum normal strain range
$\Delta\gamma_\epsilon$	= shear strain range on the plane of maximum normal strain range
α_{\max}	= angle of the plane of maximum normal strain range
$\Delta\sigma_1$	= maximum principal stress range
$\Delta\tau_\sigma$	= shear stress range on the plane of maximum principal stress range
$\Delta\tau_{\max}$	= maximum shear stress range
$\Delta\sigma_n$	= normal stress range on the plane of maximum shear stress range
$\Delta\tau_{\text{oct}}$	= octahedral shear stress range
$\Delta\sigma_{\text{oct}}$	= octahedral normal stress range
$\Delta\sigma_{\text{eq}}$	= equivalent stress range
ΔLohr	= Lohr-Ellison's parameter range

INTRODUCTION

Biaxial fatigue is often encountered in the complex thermo-mechanical loading present in gas turbine engines. Engine strain histories can involve non-constant temperature, mean stress, creep, environmental effects, both isotropic and anisotropic materials and non-proportional loading. Life prediction for the general case involving all the above is not a tractable research project. This research program was limited to isothermal fatigue at room temperature and 649°C of Hastelloy-X for both proportional and non-proportional loading.

Completely adequate life prediction methods for non-proportional loading have yet to be decisively demonstrated. Unusual non-proportional loading fatigue tests were run in this program.

Data for multiaxial fatigue at elevated temperature is quite limited. This program produced new data on the biaxial fatigue behavior at elevated temperature. Multiaxial fatigue testing is a complex and difficult task. The data in the literature is characterized by contradictory conclusions even when nominally similar materials are tested (1). We feel strongly that great care must be exercised to avoid certain practices pointed out in a recent literature review (1) that degrade data. Accordingly specimen gage section strain distribution, material anisotropy and deformation re-

sponse were all carefully studied prior to running the test program.

The goal of the project was to select the best fatigue failure parameters of the existing theories to predict the fatigue life or modify it if necessary. This goal was achieved in part, by employing an experimental set-up with several unique features that were expected to give improved data quality. In pursuing this goal 32 specimens were tested. A number of tests were designed to answer specific questions that helped direct the search for a good parameter.

In the remainder of this report relevant fatigue theories are first reviewed. This is followed by an extensive description of the test hardware the development of which consumed a substantial part of the total effort. The test results are described including baseline tests and tests designed to answer specific questions. Finally the data is used to select the best parameter.

THEORIES OF MULTIAXIAL FATIGUE

Life prediction in multiaxial fatigue depends on the use of one or more appropriate parameters to characterize the damaging nature of the applied loading. A complete review of the literature is inappropriate here as two recent reviews are available (1,3). Only certain relevant points will be discussed. It is convenient to present first the parameters based on classical failure theory and then to present the more complicated parameters. The classical failure theory approach required fatigue data from only uniaxial fatigue tests to predict fatigue lives for various multiaxial stress states while the more complicated theories generally require data from tests at several different stress states (tension and torsion for example).

The three parameters based on classical failure theories that are used for correlating multiaxial fatigue data are maximum normal stress theory, maximum shear stress theory and octahedral shear stress theory (Von Mises' theory). The above classical failure theories were characterized by contradictory conclusions even when nominally similar materials are tested (1). The more complicated failure theories (2,8) have been shown to be considerably more accurate in predicting fatigue lives. For example, in one set of biaxial experiments, fatigue lives predicted from uniaxial data using octahedral shear theory were nonconservative by a factor of 10

and 100 (4). More recently, some success has been achieved using an energy based parameter that requires damage to be calculated incrementally along the stress-strain path. Three recently developed theories which use two or more independent parameters have also been shown to give better life prediction. They will be described as follows.

(a). Gamma Plane Theory of Brown and Miller

This theory is based on the physical quantities that control fatigue crack growth, namely the maximum shear strain and the tensile strain normal to the plane of maximum shear. The direction of cracks initiated was measured during the tests. The cracks were found to initiate on the planes of maximum shear strain regardless of the maximum normal strain. Crack initiation is on the maximum shear strain plane driven mostly by shear. Secondly, initiation is affected by the tensile strain normal to the plane of maximum shear. For the crack growth process, the mode I component is the most important. The only influence of maximum normal strain on crack direction occurred for the case where every plane was a maximum shear plane, then the planes which also had maximum normal strain amplitudes tended to initiate cracks. It is worth noting that these crack direction results are different from those predicted by Findley's (5,6) theory in which the worst combination of shear and normal strain will produce cracking first.

Kanazawa, Miller and Brown (7) conducted and analyzed in-phase and five types of out-of-phase tension-torsion tests of a Cr-Mo-V steel. Results were presented in terms of the maximum shear strain theory, octahedral shear strain theory and the gamma plane theory of Brown and Miller (2). The results presented indicated that neither maximum shear strain theory nor octahedral shear strain theory did a good job at correlating the data. It was shown that the gamma plane theory of Brown and Miller did the best job at correlating the data. The chief drawback of the gamma approach is the large amount of multiaxial fatigue data that is required unless a mathematical form for constant life contours is available.

(b). Plastic Work Theory

Garud has found data that showed the shear strains in all directions resulted in the fatigue damage, not just on the shear critical plane. Accordingly he proposed a new plastic work theory of fatigue damage. The simple form of this theory states that fatigue life is a function of the plastic work done (8). The theory in its improved modified form sums plastic work where the plastic work done by applied shear stress only counts half as much as other plastic work. Analyzing the data of Kanazawa et al.(7), Garud's unmodified theory correlates all the various in-phase and out-of phase results to within a factor of three on life while the modi-

fied theory gets within a factor of about two on life. The modified version of this theory appears promising; Garud's theory obtained the same scatter as the theory of Brown and Miller when applied to the same data (7). Both of these theories look promising on the basis of the tests run. However, more data is needed to draw a final conclusion.

(c). Gamma Plane Theory of Lohr and Ellison

This approach hypothesises that the maximum shear strain γ^* , on planes driving the crack through the thickness, controls the fatigue crack propagation rate and hence the life (22). In the general cases, this shear strain γ^* does not equal the absolute maximum shear strain γ_{\max} . The direct strain ϵ_n^* acting normal to the plane of γ^* can exert a secondary modifying influence. Experimental results (9,10, 11,12,13) from several research laboratories have been analyzed in this manner with some success.

PHYSICAL CONSIDERATION OF FATIGUE MECHANISM

The two gamma plane theories mentioned above emphasize the importance of fatigue crack growth. Several investigators (14,15,16,17) had reviewed the process of crack initiation and propagation under biaxial loading. In metallic materials, cracks initiate on crystallographic planes of intensified slip. Being a slip process, the initiation mechanism will be controlled by the shear strain and occurs on the plane of maximum shear. Stage I cracks propagate on these shear planes, due to slip processes and decohesion ahead of the crack tip. For most materials, stage II propagation occurs by processes of slip and decohesion in the plastic shear ears at the crack tip. The slip and decohesion is again controlled by the maximum shear strain. On the other hand, stage II cracks may propagate by void formation ahead of the cracks, or by cleavage, particularly in brittle materials. A secondary but important effect will be that of the tensile strain across the maximum shear-strain plane. Furthermore, a law involving a combination of the maximum shear strain and the tensile strain will assist correlation of crack growth by cleavage in brittle materials, since cleavage may be primarily controlled by the maximum principal strain.

In this work efforts were directed to discover or develop a theory that can successfully predict multiaxial fatigue

life of Hastelloy-X at elevated temperature. In developing such a method consideration was given to what is known about the fatigue process. Additional guidance was taken from the results of critical experiments designed to settle certain issues and also utilized direct observation of the direction and mode of cracking in the failed specimens.

EXPERIMENTAL METHODS

Biaxial straining was produced by the application of combined tension and torsion at room temperature and 649°C. A servo hydraulic machine built using commercially made actuators and electronics combined with a University of Connecticut designed load frame. The specimens were thin walled tubes similar to those used by Kenazawa, Brown and Miller (2). The specimens were heated by band heaters on each end of the specimen and a cartridge heater inside the tubular specimen. The grip designed chosen used a disposable grip made of 304 stainless steel that was pressed on and welded.

Load and torque were measured with a commercial load-torque cell. Axial strain and angle of twist were measured using a high temperature capacitance probes mounted on a based extensometer attached directly to the gage section of the specimen. An attempt to measure through thickness strain and hoop strain was made using an external and internal capacitance ring probes. The primary reason for measuring these additional strains was to avoid possible errors in determining the maximum shear strain amplitude (see page 18). An ADAC LSI-11 based data acquisition system was used for generating the command signals and running the data acquisition system.

A major part of the project work was in developing and improving the hardware for high temperature biaxial fatigue.

At the time when this project started no commercial hardware existed for doing this type of testing . Numerous hardware items were designed and improved during the course of this project. Because a significant part of the effort was expended in developing the test hardware and a number of original pieces of equipment were developed, a detailed description of the experimental set-up will be presented.

EXPERIMENTAL FACILITIES:

1. The Testing Machine:

The testing machine (see Fig.1) uses MTS actuators and torque reaction plates and a Lebow thrust-torque sensor. Complete tension-torsion servo hydraulic tests systems are commercially available. Largely for financial reasons a similar test system was built in house. The resulting test system does however have superior alignment of the upper and lower crossheads due to the use of a large die set as a load frame. The die set chosen is similar to those used in stamping out sheet metal parts in the automotive industry. Because these die sets were produced in some volume they are much less expensive than any similar structure produced in a job shop as a special item. The key problem in making a die set into a load frame is holding the upper crosshead stationary when it is usually designed to slide up and down the frame columns for operation as a die press. This was accomplished by using large collars that clamp the cross head of the die set to the side posts. The die set load frame is shown in Fig. 1 where the collars are clearly visible. The design of such collars is largely empirical and the services of a collar manufacturer was utilized in arriving at suitable dimensions. The hydraulic actuators, lower load frame and electronics (Fig. 4) are standard components purchased from the leading manufacturer of tension-torsion ser-

vo hydraulic materials testing systems. The die set according to the manufacturer gives parallelness of the crossheads to be within 0.0833 mm/m of separation of the cross heads. This excellent alignment is obtained on a load frame that costs much less than a commercial frame.

2. Specimens and Material:

The alloy chosen is specially processed Hastelloy-X 28.6 mm dia. bar stock. This material was processed to obtain a grain size of ASTM 5-6 to simulate the condition of rolled material used in aircraft engines. The specimens used were tubes, the geometry of which is shown in Fig. 2. These specimens are sufficiently thin walled to allow for a reasonable calculation of stress from load but also resist buckling well at large strains at elevated temperature. Since the extra length of specimens were only needed for the band heaters, the specimens of room temperature tests were made shorter to save the material costs.

3. The Grips:

Design of the grips for elevated temperature tension-torsion fatigue tests is both difficult and important. Since the material chosen is generally expensive and difficult to machine, the grips were sought that would allow a simple axisymmetric specimen design with a short overall specimen length. This was achieved by using a specimen grip combination shown in Fig. 3. The grip design chosen used a disposable grip made of 304 stainless steel that was pressed on with a shrink fit with about 0.0254 mm interference. Following the shrink fit the flange was welded on the Hastelloy specimen using 310 welding rod. Following welding the specimen flange combination was put on centers and faced off at both ends in a lathe. The thickness of welded grips was reduced from 25.4 mm early in the program to 19.1 mm and both worked successfully. These grips cost roughly \$30/pair which is small compared to other costs associated with this type of testing.

4. The Heating System:

Specimen heating can be accomplished by a variety of methods including induction heating, direct resistance heating, furnace heating, radiant heating and heating by direct contact with heating elements. The specimens here were heated using coiled resistance heaters clamped on each end of the specimen (Fig. 3) and the temperatures were cont-

rolled individually by two triac controllers. The band heaters that supply 675 watts do not have sufficient power to get the specimen to 649°C without a heat shield that is currently used. The band heaters were wrapped around the specimen outside of the gage length. It was further found that it was necessary to add more energy to the gage section of the specimen to make up for gradients caused by radiation and convection losses. The center of the gage length was found about 28°C cooler than the ends. This energy was provided by using an internal cartridge heater which was 12.6 mm diameter, 25.4 mm long, and rated at 50 watts. The voltage to the cartridge heater was adjusted by a variac to apply a predetermined power to the cartridge heater which from calibration tests was shown to give the most uniform gage section temperature. With this combination of heaters and a three layer round heat shield which was made of 304 stainless steel and has an open bottom end, the temperature in the gage length was uniform within 4.4°C to 5.6°C and easily reached 649°C. Note that the K type thermocouple wire used has an error which is 2.7°C at 649°C

5. Extensometer:

Extensometry is acknowledged to be the most troublesome aspect of elevated temperature tension-torsion fatigue testing (18). The extensometer developed here is partly an adaptation of that described in References 19 and 20. In de-

signing this extensometer it was decided that avoiding the need for cooling was desirable because cooling hoses tend to cause vibration problems and exert undesirable force on extensometers. To avoid the need for cooling the extensometer, high temperature commercial capacitance displacement probes were used (Fig. 5). The probes are rated by the vendor to 788°C. Since the probes are not at the specimen surface the probe temperature is much less than the specimen temperature as long as furnace heating is not used. Measurement of the temperature near the probes in 649° C tests utilizing the heating method described above, the probe temperature was less than 371°C. Thus using the commercial probes tests far in excess of 788°C should be possible with this extensometer.

The extensometer has been modified twice to improved its performance. The configuration of extensometer is shown in Fig. 5. Axial displacement was measured using two axially mounted probes measuring the distance to axial targets. The output of the two axial probes was summed to cancel out cross talk caused by imperfect alignment and false strains caused by rigid body wobble of the extensometer. The angle of twist was measured by two probes measuring the distance to radially mounted targets. The final excellent version of torsional targets were made of two seperate pieces which will assure the targets remain square with the extensometer.

The displacement of the radial targets is related to the angle of twist by the following equation.

$$d \approx R(\sin\theta) \approx R\theta$$

d : The displacement of torsional target center relative to the torsional probe center.

R : The distance between the specimen center and the target center.

θ : The angle of twist, in radians.

It is clear that the response of the probes is nonlinear. However for the largest strains measured were 2% and the nonlinearity was estimated to be 2.4% which is accepted as part of the error.

A jig with a known gage length shown in Fig. 6 was developed to ensure proper alignment and concentricity when mounting the extensometer. By adjusting inwards or outwards the three 6.35 mm x 28 screws of extensometer, the extensometer can be used for different specimen O.D. A special jig was also built and used to ensure the angles between each screw being 120 degrees.

The extensometer was attached to the specimen using tungsten carbide conical points. To avoid attachment induced failure the gage length of the extensometer was increased to 33 mm to move the attachment slightly up the transition. Comparison with strain gage data showed that the calibration factor change due to the non-constant thickness in the gage

section was only 0.5% compared to that expected for a perfectly uniform gage section. Computer monitoring of the axial and torsional probes individually showed that for the axial probes, two probes are necessary to cancel out the effects of small imperfections in the mounting alignment and small wobbling problems. In the case of the torsional probes that have a full scale range of 6.35 mm the use of two probes is much less critical.

An attempt was made to measure cross talk between the torsion and tension strain channels. This was done by subjecting a specimen in load control to pure torsion and measuring the apparent strain on the axial extensometer. The axial channel was in load control with a static zero load command. In this test for a 1% torsional strain the false apparent strain in tension was 53 micro strains (Fig. 7). Interchanging the role of tension and torsion when 1% strain was applied axially there was an apparent torsional strain of 29 micro strains (Fig. 8). The measurement of cross talk is somewhat problematical as it is very difficult to produce pure twist with no axial strain or vice versa. It is well known that there is a second order effect called the Poynting effect that will give axial strain in a pure torsion test and vice versa. In Reference 21, OFHC copper was tested in torsion and at 1% strain the axial strain due to the Poynting effect is comparable to the strain attributed to cross talk in the experiments done here. We can conclude

that the extensometer may have far less cross talk than measured cross talk is probably an upper bond. Having used this extensometer for several years it is basically satisfactory. However a second generation extensometer is ^{now} under design and it will include stiffer supports for the carbide points and axial probes with 1.27 mm full scale range as compared with the current 0.51 mm full scale which is small. Any misalignment during set up cuts the usable range down forcing careful time consuming alignment that would be less important for the larger full scale range.

6. Capacitance Ring Probes:

In biaxial testing two strains are ordinarily measured. However in order to solve for principal strain and other quantities it is necessary to know the full strain tensor. Usually this is done by assuming an equivalent Poisson's ratio (22). The assumptions made about the Poisson's ratio significantly affect the calculated values of various parameters used to correlate fatigue data (23). The actual behavior of the two non-measured normal strains would be derivable from a constitutive equation. If classical plasticity is assumed to govern the inelastic strains and a Tresca flow rule is used all plastic deformation occurs by slip on maximum shear planes only and there would be no circumferential plastic strain and volume would be conserved by a large through thickness strain. This behavior would be very dif-

ferent than that assumed in most equivalent Poisson's ratio approaches. Given the significant effect of assumptions made about the unmeasured normal strains it seemed appropriate to measure the through thickness strain and circumferential strain if possible. The work described herein was primarily for the study of elevated temperature response at large cyclic strains so that conventional strain gage approaches were only useful at room temperature. The attempt to measure through thickness strain with capacitance ring probes was not successful. However a great deal was learned about the behaviors of these probes and the required design changes to make the system work were determined but not implemented due to lack of time and funds. The following description of the ring probes is of interest to those desiring to make such measurements. At room temperature the hoop strain was measured with strain gages and in spite of what is predicted by maximum shear stress flow rules, effective Poisson's ratio formula (Eq. 5) was quite accurate in describing the deformation.

An attempt was made to measure the average change in outside diameter and inside diameter of the tension-torsion specimen. Assuming that the tube remains circular half of the difference of these two diameters is directly related to the through thickness strain if the tubes are assumed to be thin. The change in the sum of the outside diameter and inside diameter divided by two is the change in the average

diameter and for circular thin tube this is proportional to the circumferential strain. Capacitors were formed for measuring the O.D. using the specimen as one side of the capacitor and a toroidal shaped ring probe as the other side of the capacitor. The outer ring probe which is 50.8 mm O.D., 33 mm I.D. and 3.18 mm thick is shown in Fig. 9. The capacitance of this geometry is related to the distance between the inside of the ring probe and the specimen O.D. To measure the change in inside diameter a capacitance probe was placed in the center of the tubular specimen (Fig. 9) forming another annular gap capacitor as on the O.D. The sensor disc of this inner ring probe is 8.89 mm diameter and 1.27 mm thick. Again the capacitance is some function of the average diameter difference of the probe and the specimen.

Tests were done to adjust the linearity of this set up using a three slope linearizing circuit built in to the signal conditioner and to access the probes sensitivity to imperfections in the concentricity of the probe and specimen and to study the effect of inevitable lateral (concentricity destroying) motions of the ring probes. In order to study the behavior of the capacitance probes calibration jigs were built as shown in Figs. 10 and 11. The three diameters of the outer ring probe calibration gage are 17.78 mm, 18.034 mm and 18.415 mm while they are 12.573 mm, 12.7 mm and 12.827 mm for the inner ring probe. The calibration fixtures were moved relative to the probe using a servo hydrau-

lic fatigue test machine where the axial motion was measured with an LVDT. By this means it was possible to plot the ring probe output versus the position of the probe relative to the calibration fixture and get three readings of probe output for the three diameters involved. The representative output are shown in Figs. 12 and 13. An edge effect was found to extend up to 25.4 mm from a free end and up to 11 mm from a step of diameter change. Using this set up the probe linearity was adjusted with the built in linearizer. It is worth noting that the probe senses the steps in the calibration fixture gradually over a distance (Figs. 12 and 13). The probe calibration factor of the O.D. was 0.424 mm/volt while for the I.D. it was 0.170 mm/volt.

It is also important to see how sensitive the probe capacitance was to disturbing the concentricity of the probe and target. By setting up the outer ring probe vertically it was possible to plot the change in the probe output versus change in the position of the calibration fixture along a radial line away from the perfectly centered position. This result is shown in Figs. 14 and 15. Here it is apparent that the probe output is maximum when the probe and target are concentric and that as the target is moved from the concentric position the probe output changes in a parabolic way. The sensitivity of the probes to changes in concentricity has important implications to the measurement of diameter change during a cyclic test. Specially if the probe - speci-

men concentricity changes cyclically during straining there will be a false diameter change recorded due to the effect of concentricity change. To get a feel for the sort of concentricity change that can be tolerated in measuring circumferential strain, a representative case will now be considered. If the specimen used in this experiment were strained 1% then the Poisson's strains would be roughly 0.5% resulting in a I.D. change of 0.0635 mm and an O.D. change of 0.0889 mm. If the toleratable error is to be 2% of the total change using the graphs Figs. 14 and 15 then the O.D. concentricity must be constant within 0.127 mm and the I.D. concentricity must be constant within 0.0381 mm. There is some small wobble in the extensometer frame that is well compensated for during axial and torsional strain measurement by the use of double sensors. However for the ring probes it is unclear if the wobble will cause serious errors in our set-up. Finally the noise of the outer ring probe is found to be approximately equivalent to 0.00305 mm O.D. change (Fig. 14) and for the inner ring probe it is equivalent to 0.000838 mm I.D. change (Fig. 15) which means that measuring a wall thickness change of 0.0127 mm is going to be very difficult to do with great accuracy.

It is also important to consider possible changes in the calibration constant due to static non-concentric arrangement of the probe and the target caused by imperfect set up. Using the outer ring probe the effect on calibration con-

stant was determined and is shown in Fig. 16. From this figure it is apparent that static set up induced eccentricity of 0.127 mm will result in less than a 1.5% change in the calibration factor. Identical experiments performed on the inner ring probe are shown in Fig. 17 where it is apparent that for 0.127 mm eccentricity the error is about the same as for the outer ring probe but for the larger eccentricity the error is larger than the corresponding error in the outer ring probe. Using the simple set-up procedure employed the eccentricity should be less than 0.127 mm for both probes so that this source of error is not expected to be serious.

Mounting the outer ring probe on the extensometer and fixing the extension of inner ring probe to the upper grip, one room temperature test using the ring probes was run at $\lambda = 0.2$, $\Delta\epsilon = 1\%$, and $\Delta\gamma = 0.2\%$. One resistance strain gage was mounted on the specimen gage section in the transverse direction to check the ring probes performance. At the maximum applied tensile strain, the circumferential strain measured by strain gage was -0.1669% and it is -0.2047% calculated by assuming a elastic Poisson's ratio of 0.3 and plastic Poisson's ratio of 0.5 and using Eq. 5. The circumferential strain and through thickness strain are expressed in terms of the polar components of displacement u and v by the following relationships:

$$\epsilon_r = \frac{\partial u}{\partial r} \quad (1)$$

$$\epsilon_\theta = \frac{u}{r} + \frac{1}{r} \frac{\partial V}{\partial \theta} \quad (2)$$

where u : displacement in the radial direction
 V : displacement in the tangential direction
 ϵ_r : through thickness strain
 ϵ_θ : circumferential strain

The second term $\frac{1}{r} \frac{\partial V}{\partial \theta}$ in Eq. (2) is ignored because the specimen response is axisymmetrical.

Let u_o = displacement of element at the outer surface
 u_i = displacement of element at the inner surface
 u_m = displacement of element at the middle surface
 r_o = outer radius
 r_i = inner radius
 r_m = radius of the middle surface
 OD = outer diameter
 ID = inner diameter
 ΔOD = O.D. change
 ΔID = I.D. change
 $u_o = \Delta OD/2$
 $u_i = \Delta ID/2$

Thus

$$\epsilon_r = \frac{\partial u}{\partial r} \approx \frac{\Delta u}{\Delta r} = \frac{u_o - u_i}{r_o - r_i}$$

$$\epsilon_r = \frac{\Delta OD - \Delta ID}{OD - ID} \quad (3)$$

consider the middle surface at a radius of r_m .

$$u_m \approx \frac{u_o + u_i}{2} = \frac{\Delta OD + \Delta ID}{4}$$

$$r_m = \frac{r_o + r_i}{2} = \frac{OD + ID}{4}$$

$$\epsilon_\theta = \frac{u_m}{r_m}$$

$$= \frac{\Delta OD + \Delta ID}{OD + ID} \quad (4)$$

The O.D. and I.D. changes recorded in this test were 0.04532 mm and 0.01287 mm respectively. Using Eqs. 3 and 4, the circumferential strain was found to be -0.1905% while the through thickness strain was -0.6432% at the peak value of applied tensile strain. The measured circumferential strain is in rough agreement with the strain gage however the through thickness strain is larger than the applied axial strain which is not at all likely to be correct. There appears to be a large error in through thickness strain. Random noise was 6.7% of the measured O.D. change and 6.5% of the measured I.D. change. The sum of the two noise signals is 12% of the measured wall thickness change. The noise al-

though significant does not appear to explain the large improbable value of through thickness strain measured. The most likely explanation of this error is that it is caused by some amount of wobble of the extensometer support rings to which the outer ring probe is attached. In this experiment the ring probes were unsuccessful in providing the desired measurement of strains. Possible improvement may be realized by mounting the outer ring probe from a holder attached to the lower cross head and/or making a new outer ring probe that fits more closely around the specimen.

The ring probes show satisfactory behavior with respect to linearity and effects of static eccentricity. The random noise present in the probe set up lead to errors on the order of 10% which is significant but does not completely destroy the system usefulness. More importantly the ring probes sensitivity to dynamic eccentricity changes seemed to prevent them from making the desired measurement.

From the investigation, the conclusions of ring probes behavior are drawn as follows:

- a) The output voltages of the ring probes is maximum when the ring probe is set concentrically with the specimen.
- b) For the 17.78 mm O.D. specimen and the existing outer ring probe, the allowable eccentricity is 0.127 mm which will cause 1.5% error of calibration factor.

- c) For the 12.7 mm I.D. specimen and the existing inner ring probe, the allowable eccentricity is 0.127 mm which will cause a 1.2% change in the calibration factor.
- d) The error of ring probes output due to the eccentricity is dependent on the gap between the specimen and ring probes. For a same eccentricity, the smaller gap between the specimen and ring probes, the smaller the error is (see Figs. 16 and 17).
- e) To mount ring probes for tests, they were moved around the specimen until the probe outputs reach the maximum value.
- f) For the existing ring probes, the outer ring probe has a larger noise level than that of inner ring probe. Due to these noise levels, the measurement of O.D. and I.D. changes is compromised.
- g) The wobbling of extensometer is the most serious problem to spoil the accuracy of measuring the O.D. changes. The outer ring probe should be mounted on a fixed point and not attached to the extensometer.

Having incomplete success with the ring probes and lacking funds for making new ring probes one additional experiment using resistance strain gages was conducted. Circumferential strain was measured as well as axial strain. The strain gage used had a 1.575 mm gage length and the specimen was subjected to a proportional load cycle with the torsion-

al strain range of 0.26% and an axial strain range of 1.3%. At the peak strain the Poisson's ratio was determined to be 0.423. Calculation of an equivalent Poisson's ratio by the usual formula given below resulted in a effective Poisson's ratio of 0.413 which is quite close to the measured one.

$$\nu_{\text{eff}} = \frac{\nu_e (\sigma/E) + \nu_p (\epsilon_{\text{tot}} - \sigma/E)}{\epsilon_{\text{tot}}} \quad (5)$$

where ν_{eff} = effective Poisson's ratio

ϵ_{tot} = total axial strain

σ = stress amplitude

E = Young's modulus

ν_e = elastic Poisson's ratio = 0.3

ν_p = plastic Poisson's ratio = 0.5

This result suggests that for this material at this temperature the effective Poisson's ratio approach is reasonable. Since this result depends essentially on the inelastic flow rule. The effective Poisson's ratio may not always be accurate and its validity should be verified on a case by case basis.

7. Computer Data Acquisition System:

An ADAC LSI-11 based data acquisition system was purchased by the University of Connecticut. Seven channels of data were recorded using the A/D converter and two channels of command signals were generated by the D/A converter. A master patch panel was made for the data acquisition and external feedback control of the testing machine (Fig. 4). Several programs for running the data acquisition and generating the command signals were written and run satisfactorily. The software system for running tests and data reduction was well developed and introduced briefly in Appendix I.

EXPERIMENTS AND RESULTS

All fatigue tests were fully reversed strain controlled tests. All waveforms of the axial and torsional strain cycles were sinusoidal. The following quantity was used to characterize the biaxial tests.

$$\lambda = \frac{\text{range of total applied shear strain}}{\text{range of total applied normal strain}}$$

The direction of cracking and the planes of maximum shear strain are often discussed. These plane orientations are defined by an angle which identifies the orientation of a plane on the surface of the specimen. This angle is measured from an axial (longitudinal) line on the specimen surface and counter clockwise is considered positive.

The testing conditions and results are shown in Tables 1A-6B. It is worth noting that the stresses given were calculated by treating the specimen as a thin-walled tube. The formulas used to compute the stresses are given below:

for normal stresses,

$$A = \pi(r_o^2 - r_i^2)$$

$$\sigma = \frac{P}{A} \tag{6}$$

where p = applied axial force

σ = normal stress amplitude

A = cross section area of specimen in the gage
length

for assuming constant through thickness shear stresses,

$$\tau = \frac{3T}{2\pi(r_o^3 - r_i^3)} \quad (7)$$

where τ = shear stress amplitude

T = applied torque

r_o = outer radius of specimen in gage section

r_i = inner radius of specimen in gage section

The applied stresses, applied strains, plastic strains and fatigue life parameters were determined from the hysteresis loops at approximately mid-life. Typical hysteresis loops of different test conditions are shown in Figs. 39 - 59.

Some typical plots of shear strain range and normal strain range vs. orientation of planes ($\psi = 0^\circ - 90^\circ$) are shown in Figs. 60 - 71, which will highlight the relative importance of shear strain and normal strain. In 90 degrees out of phase non-proportional loading the shear strain range is almost the same on all planes.

1. Check for Anisotropy

Unrecognized anisotropy could produce many unexplained results and scatter. Four uniaxial fatigue tests at two strain levels at 649°C were run on small specimens cut from both the longitudinal direction and the transverse direction to compare the properties in the two directions.

Using the maximum shear strain theory, the $\Delta\gamma_{\max}$ vs. N_f was plotted and is shown in Fig. 18. It correlated the results of the two orientations within a factor of about 1.5 on life. The factor of 1.5 is only slightly more than the expected scatter indicating that the material is nearly isotropic.

2. Check the Strain Distribution on Gage Section

Unrecognized strain gradients result in non-comparability of data between investigators and has an unknown effect on the relative size of the strain components. One 10 - element strain gage was mounted on the specimen gage section to check the strain distribution under the elastic and inelastic tension-compression loading at different strain levels.

The axial strains were found to be maximum in the middle of gage section. The strain distribution for an elastic tension-compression loading is shown in Fig. 19. For tension-compression inelastic loading, four cycles at different strain levels were run and the strain distribution is shown

in Fig. 20. The strain variation along the gage section is approximately ± 10 micro strain at an applied strain of 0.083%. The strain distribution is fairly uniform having a strain variation of $\pm 1.2\%$ about the mean value within the gage section.

3. Check the Elastic Poisson's Ratio

Two resistance strain gages were mounted on the middle of specimen gage section in the longitudinal and transverse directions. The axial strain and hoop strain were measured to be 560 and -172 micro strains respectively under an elastic tensile loading. For an elastic compressive loading, the hoop strain of 166 micro strains was obtained under an axial strain of -569 micro strains. The elastic Poisson's ratio was found to be .307 under the tensile loading, and .292 under the compressive loading.

4. Check for Strain Rate Effects

To determine the strain rate effect on the fatigue behavior, two tension-torsion in phase fatigue tests at a same axial and torsional strain range ($\Delta\epsilon = 0.6\%$, $\Delta\gamma = 0.9\%$) but different strain rates (axial strain rates of .003/sec and .0006/sec) were run at 649°C for $\lambda = 1.5$ (Tests # 34 and 35). The strain rate was found to have a small effect on the fatigue lives. The fatigue lives were 2,533 cycles and 2,150 cycles for the axial strain rates of .003/sec and .0006/sec

respectively. The larger strain rate produced a longer fatigue life . For the data correlation to fatigue theories, see Tables 6A - 6B and Figs 27 - 38.

5. Tests Using Induction Heater

One of the most convenient heating methods for elevated temperature fatigue is induction heating. In uniaxial testing it is possible to arrange the coil such that the current flow is parallel to the stage II mode I cracking direction. In multiaxial fatigue the crack direction is not in general known and the question of local crack tip heating due to the crack concentrating the induction field becomes a more important issue. A torsion fatigue test using audio frequency (10 KHz) induction heating was run for an applied torsional strain range of 2.36% at 649°C (Test # 36) to compare the performance of the induction heating system with band heaters. The fatigue life was found to be 2,308 cycles. Correlating this fatigue life and another three lives from pure torsion tests using band heaters (Tests # 10, 18 and 19) to fatigue theories with various parameters, it was found that all the points fell in a straight line with a small scatter in the log-log space (see Figs. 27 - 36).

The crack directions observed were 45 degrees which are on maximum normal strain planes and same as that of Tests # 10, 18 and 19 (Fig. 79). Based on the fatigue life and crack direction, the experimental results of test using in-

duction heating are well consistent with that of tests using band heaters.

It is worth noting that two factors probably contributed to the success of induction heating in this case. Firstly a low audio frequency heating was used which would presumably give a greater heating depth than the more usual radio frequency heaters and secondly the specimen wall thickness was 2.54 mm which is fairly thick compared to the crack length for most of the fatigue life. Use of induction heating of either higher frequency or on thinner walled specimens should be verified before it is assumed to be acceptable.

6. Baseline Tests

Designer rarely have biaxial data. Therefore, the ultimate goal of this program is to predict multiaxial fatigue from uniaxial fatigue data or uniaxial tension data combined with torsion data. To attempt such predictions torsion and tension data are needed. Strain controlled uniaxial tension and pure torsion fatigue tests were run at two strain levels at R.T. The two tests for checking the material anisotropy with small specimens cut from the longitudinal direction were used as the baseline tests for uniaxial tests at 649°C. Pure torsion fatigue tests using band heaters were run at three strain levels at 649°C.

Basic biaxial tests provide the first easy test for any proposed fatigue parameters. Tension-Torsion in phase fatigue tests at two strain levels were run at R.T. at $\lambda = 1.5$, and $\lambda = 4$ and 649°C for $\lambda = 1.5$. The waveforms of axial and torsional strain cycles are shown in Fig. 21.

The results of baseline tests are shown in Table 1A - 4B and the data correlation to the fatigue theories are shown in Figs. 27 - 38. Under the same test conditions, the fatigue lives at 649°C were much shorter than that of room temperature.

7. Non-Proportional Loading Tests

Non-proportional loading occurs in many real fatigue problems included aircraft engines. It is by far more difficult to successfully predict non-proportional than proportional loading. Non-proportional loading experiments are especially valuable because they provide a severe test of any life prediction method and can be used to quickly eliminate unsuitable theories. Three different groups of non-proportional loading tests were run in this program.

Test (a)

This test series involved a very special case of straining where the principal strains remain nearly constant but rotate with respect to the specimen axis. For this special case total strain amplitudes if taken without the considera-

tion of a critical plane are approximately zero. If such tests give a finite fatigue life then total strain theories that do not consider critical planes are ruled out from consideration. Secondly these tests were also run to see if straining path has a major effect on fatigue life.

Test were run at 649°C with $\lambda = 1.5$ and with a 90 degrees phase difference between the applied torsional strain and the applied axial strain. The tests were run at two strain levels, axial strain range of .512% and .909% (Tests # 20 and 21). For this type of test the magnitude of the principal strains remain constant while the orientation of the principal planes rotate at a constant angular velocity. The fatigue lives of Tests # 20 and 21 were 5,750 cycles and 522 cycles respectively. The waveforms of axial and torsional strain cycles are shown in Fig. 22.

Comparison of the fatigue lives between the in-phase, $\lambda = 1.5$ and 90 degrees out-of-phase biaxial loading depends on the fatigue parameters chosen (see Figs. 27 - 38). Of the various parameters, the modified plastic work theory did the best job correlating this data. The modified cyclic plastic work correlates the in-phase and out-of-phase results to factors of 1.1 and 1.9 on life for the applied axial strain range of 0.512% and 0.909% (Tests # 20 and 21) respectively while the maximum shear strain theory gets factors of 3 and 4 on life. This result indicates that the modified cyclic

plastic work could be the best parameter to correlate the fatigue lives under the out-of-phase non-proportional loading.

For the non-proportional loading tests with a phase angle of 90 degrees, the magnitude of the maximum shear strain remain constant while the orientation of the principal planes rotate at a constant angular velocity. The maximum shear strain amplitude versus time is shown in Fig. 26. If fatigue damage only depends on the amplitude of strain or stress regardless of critical planes, the fatigue life of this kind tests would be infinite. This test result shows that a total strain quantity computed without the consideration of a critical plane will not work well for non-proportional loading. More promising would be a strain quantity calculated for a critical plane or a quantity related to plastic flow such as plastic work both of which at least predict finite life for the out-of-phase tests described here.

Test (b)

These tests were designed to produce a mean tensile or compressive axial stress which is in general hard to sustain in low cycle strain controlled fatigue. The tests consisted of alternate fully reversed cycles of torsional and axial strain. The torsional strain was held at zero while the tension cycle was occurring and vice versa. Tension cycles end-

ing with increasing axial strain resulted in a tensile axial stress during the torsion cycle and also have a tensile mean stress. Cycles ending with a decreasing axial strain resulted in compressive axial mean stress. In Test # 27, immediately following the tensile excursion the tensile stress is 37.3% of the maximum stress in the cycle. This tensile stress present during the torsion part of the cycle relaxed steadily and at the end of the cycle it was only 22% of the maximum stress for the entire cycle. These stress values for the other tests are summarized in Table 9. These tests will show the effect of mean normal stress on the biaxial fatigue life. Four tests were run at 649° C, $\lambda = 1.5$, at two strain levels. The waveforms of axial and torsional strain cycles are shown in Fig. 23 and 24.

Tests # 25 and 29 were the first pair to produce a mean tensile and compressive axial stress respectively, at the same applied axial strain range of .512%. The fatigue lives were 7,589 cycles and 11,715 cycles respectively. It is clear to see that the mean tensile stress produced more damage and had a shorter life at this applied strain range. Similarly, at an applied axial strain range of .996% Tests # 27 and 28 produced a mean tensile and compressive axial stress and had fatigue lives of 1,119 cycles and 1,247 cycles respectively. Not much difference of fatigue lives was found at the larger applied strain.

Data correlation to the different fatigue parameters are shown in Figs. 27 - 36. These figures show that the mean compressive axial stress during the torsional cycle only make the fatigue life a little bit longer. In low cycle fatigue the effect of mean normal stress can be probably ignored.

Test (c)

Tension-Torsion fatigue tests were performed by applying intermittent axial half cycles with a period of one tenth or one fifth that of the applied torsion but of the same frequency. The different period ratio of axial straining to that of torsion will highlight the effect of straining path on the fatigue life. Four tests were run at different strain levels, at 649°C and $\lambda = 1.5$ (Tests 30 through 33). The waveforms of axial and torsional strain cycles are shown in Fig. 25.

Tests # 30 and 32 were a pair of tests which were run at the same applied strain levels (axial strain range of .703% and torsional strain range of 1.02%) but different period ratios (one tenth for Test # 30 and one fifth for Test # 32). The fatigue lives of Tests # 30 and 32 were 2,700 cycles and 2,300 cycles respectively. These results indicate that the larger period ratio of axial straining to that of torsion makes the fatigue life slightly shorter.

Test # 31 and 33 were the other pair of high cycle fatigue tests which were run at different applied strain levels (.381% axial strain range for Test # 31 and .497% axial strain range for Test # 33) and different period ratios (one tenth for Test # 31 and one fifth for Test # 33). The fatigue lives of Test # 31 and 33 came out to be 77,000 cycles and 10,279 cycles respectively. Due to the different applied strains, these two fatigue lives can not be compared directly. The plots of fatigue parameters versus life (Figs. 27 - 36) show that the test of larger period ratio (Test # 33) also has a shorter life at a same level of small strain.

Correlating the experimental data to the fatigue theories (Figs. 27 - 36) shows that the straining path had an effect on fatigue lives when the relative period of axial cycle to that of torsional cycle was changed. Having the same period of axial straining as that of torsion cycle (period ratio = 1), the two non-proportional loading tests with a phase angle of 90 degrees have the shortest fatigue lives compared with that of tests with period ratios of one fifth and one tenth (tests of this section (c)) and can be treated as the worst case of Tests (c). How much effect of the period ratio has on fatigue lives depends on the fatigue parameters chosen and the strain levels. For example, at a maximum shear strain range of 1% the normalized lives are 1, 1.3 and 1.6 for the period ratios of 1, 0.2 and 0.1 respectively. In contrast to other metals (24), the straining path in non-

proportional loading has only a small effect on fatigue lives for the material studied.

Looking back at all the non-proportional tests collectively in terms of the various parameters (Figs. 27 - 37). It is apparent that the fatigue lives are not decisively shorter than for proportional loading tests. This is in contrast to more damaging nature of non-proportional loading exhibited in most other materials (1)

CORRELATION OF MULTIAXIAL FATIGUE THEORIES

The test data has been plotted according to a number of popular multiaxial fatigue theories as below (See Figs. 27 - 38). All the formulas used to calculate the fatigue parameters are listed in Appendix II.

- (a). Plastic work theory
- (b). Modified plastic work theory
- (c). Maximum shear strain theory
- (d). Maximum plastic shear strain theory
- (e). Octahedral shear strain theory
- (f). Maximum normal strain theory
- (g). Gama plane theory
- (h). Maximum principal stress theory
- (i). Maximum shear stress theory
- (j). Octahedral shear stress theory
- (k). Lohr-Ellison's parameter

Each single parameter theory was least square fit as a straight line in log-log space. These linear regressions yielded correlation coefficients that are a measure of the success of the various theories. In Table 7 and 8 the correlation coefficients are reported and the theories are listed in order starting with the most successful theory. All tests were included in the correlation. When the correlation was also run without Tests 25, 27, 28 and 29 which involved alternate tension and torsion the correlation coefficient

was not greatly affected. The elimination of these tests from the correlation was explored as it is unclear whether in such tests one should count tension and torsion cycles additively or whether each block consisting of one tension and one torsion cycle should be counted as one cycle. In the graphs the tests were plotted counting the tension and torsion additively. From these tables the modified plastic work theory appear the most successful. But it is necessary to get the required constitutive model to compute the cyclic plastic work for each different test condition and like any energy based theory, the plastic work theory can not predict the crack growth direction. For lives in excess of 3000 cycles, the results appear to diverge, making life assessment difficult when cyclic plastic work are small. Unfortunately plastic work is one of the most uncertain quantities coming from structural analysis using an inelastic constitutive model. In Reference 25, the plastic work at a particular location was made to vary depending on the details of the constitutive model and finite element representation.

In light of the difficulty of determining the plastic work, the second most successful parameter might be used which was octahedral shear stress for elevated temperature tests, and was maximum normal strain for the room temperature tests. For the case of cyclic pressure loading, maximum normal strain theory would predict eventual fatigue failure which probably would not occur in a defect free ma-

terial because cyclic pressure should not produce any plastic strain. If hydrostatic cycling were important for a particular room temperature application then octahedral shear strain might be used as it is also reasonably good according to the data.

CRACKS OBSERVATION

Using a large Toolmaker's microscope, the direct observation of the direction and mode of cracking in the failed specimens were observed and is shown in Figs. 72 - 83. The microscope has a circular disc which can be moved in X, Y directions and rotated both clockwise and counter-clockwise by three micrometers. The failed specimens were set horizontally on the circular disc on two V-blocks. Cracks were found with the microscope and the specimen was rotated until the crack coincided with a fixed line which could be seen through the lens of microscope. The angle of rotation is the crack direction and was read from the circular disc. Since the crack direction for fatigue crack initiation is best indicated by the direction of small cracks, the main crack direction was not included in the data recorded and only the directions of small cracks were measured. Multiple small cracks were observed on most failed specimens.

In the room temperature tests the cracks are all on the maximum shear strain planes as reported by Kanazawa et. al. (7) but at 649° C all cracking is on the maximum normal strain planes. The direction of cracking at 649° C is suggestive of a fatigue mechanism change and also suggests that the theory of Brown and Miller may not be applicable.

Reuchet and Remy (26,27) investigated the influence of oxidation at high temperature fatigue of MAR-M 509. The

change in cracking direction surely indicates a change in initiation mechanism. Without detailed metallurgical investigation the new mechanism is a matter of speculation. A plausible mechanism is oxidation cracking of the small MC carbides present in this alloy. This mechanism has been observed in a number of other alloys including those in References 26 and 27.

CONCLUSIONS

From these experiments it has been possible to access the relative success for the various theories and the results are interesting but not surprising. The results have two major surprising aspects. First it was found that non-proportional loading even with a wide variety of loading paths was not significantly harder to predict the fatigue lives than that of proportional loading multiaxial tests. This is in sharp contrast to the findings of nearly all other investigations (1,3,24). Second fatigue crack initiation at elevated temperature was on maximum normal strain planes in contrast to the cracking on planes of maximum shear usually observed (1,3,24). The reason of the crack direction change is undoubtedly caused by a change in mechanism of initiation that occurs at elevated temperature. The reason for the lack of effect of non-proportional loading is unclear at this time. Specific conclusions are as follows:

1. The use of a large commercial die set as a load frame is both cost effective and results in excellent alignment of the upper and lower crossheads.
2. The biaxial extensometer based on capacitance displacement probes works well provided local heating methods (induction, band heaters ect.) are used. Test temperature up to the melting point of most aircraft engine alloys should be possible. Cross talk of the extensometer is less than 0.5% which is comparable to most of commercial load cells.

3. Specimen heating using clamp on band heaters outside of the gage length provides satisfactory temperature distribution up to 649°C if an internal heater is also used to improve the temperature profile.
4. A single experiment using induction heating in a torsion test showed no significant difference from the tests run using band heaters. It suggests that feared effect of crack tip heating was not significant for the specimen and life range considered.
5. The capacitance ring probes developed to measure circumferential strain and through thickness strain were not fully successful. The probable cause of the lack of success is the ring probe wobble causing false apparent diameter change. Possible improvement in the system success could be obtained by moving the outer ring probe mounting from the motion prone extensometer frame to a holder attached to the lower cross head.
6. Strain gage tests at room temperature suggest that at least for the limited conditions considered effective Poisson's ratio approach are reasonably accurate. Whether this is true of other materials and conditions is unknown.
7. The strain rate has a small effect on the fatigue lives.

8. Fatigue lives are not only a function of strain amplitude but also depend weakly on straining path.
9. The mean normal stress during the torsion cycle has little effect on the biaxial fatigue life at elevated temperature. The tensile mean stress during the torsional straining produces only slightly more fatigue damage than that of compressive axial mean stress during the torsion cycle.
10. Non-proportional loading was not significantly more damaging than proportional loading at 649 C.
11. The modified plastic work theory is the most successful theory for predicting the biaxial fatigue lives at elevated temperature if the required correct constitutive response is known. Unfortunately plastic work is a very difficult quantity to calculate in component analysis (25). Therefore, for the practical design purpose the most convenient theory to predict the fatigue life at elevated temperature is probably the octahedral shear stress theory and it is the octahedral shear strain theory for room temperature tests.
12. The cracking mode switched from primarily cracking on the maximum shear planes at room temperature to cracking on the maximum normal strain planes at 649°C is probably due to a fatigue-oxidation interaction.

TABLE 1-A

Spec. No.	1	2	3	4	5
Temp., °C	649	649	RT	RT	RT
Spec. O.D., mm	2.751	2.748	17.823	17.816	17.816
Spec. I.D., mm	.0	0	12.725	12.720	12.730
G.L., mm.			30.48	27.94	27.94
E, MPa $\times 10^3$	159	153	193	193	193
G, MPa $\times 10^3$	61	61	79.4	79.4	79.4
ν	0.4	0.4	0.4	0.4	0.4
λ	0	0	4.0	1.5	0
ϕ , degrees	0	0	0	0	0
N_f , cycles	39,318	2,057	6,084	4,115	40,641
$\Delta\epsilon$, %	.52	.95	.5511	1.145	.674
$\Delta\gamma$, %	0	0	2.130	1.630	0
ΔP , KN	4	5.2	56	98	107
ΔT , N·m	0	0	551	349	0
ΔS , MPa	660	858	455	802	875
$\Delta\tau$, MPa	0	0	583	371	0
$\Delta\epsilon_p$, %	.11	.41	.2511	.6636	.2292
$\Delta\gamma_p$, %	0	0	1.140	1.043	0
ΔW_p^E , KJ/m ³	510	2,689	827	3,833	1,931
ΔW_p^Y , KJ/m ³	0	0	4,999	2,916	0
ΔW_p , KJ/m ³	510	2,689	5,826	6,750	1,931
ΔW_p^* , KJ/m ³	510	2,689	3,330	5,295	1,931
$\Delta\gamma_{oct}$, %	.686	1.254	1.8847	2.0135	.8896
$\Delta\gamma_{max}$, %	.728	1.330	2.265	2.2857	.9436

TABLE 1-B

Spec. No.	1	2	3	4	5
$\Delta\gamma_{\max}^p$, %	.1865	.626	1.499	1.620	.3924
$\Delta\epsilon_n$, %	.156	.285	.1675	.3334	.2022
ψ_{\max} , degrees	45	45	80	68	45
$\Delta\epsilon_l$, %	.52	.95	1.298	1.486	.674
$\Delta\gamma_e$, %	0	0	.0273	.0293	0
α_{\max} , degrees	0	0	35	23	0
$\Delta\sigma_l$, MPa	660	858	853	945	875
$\Delta\tau_{\sigma}$, MPa	0	0	15	26	0
$\Delta\tau_{\max}$, MPa	330	429	626	544	437
$\Delta\sigma_n$, MPa	330	429	235	407	437
$\Delta\tau_{\text{oct}}$, MPa	311	405	522	483	412
$\Delta\sigma_{\text{oct}}$, MPa	220	286	151	267	292
$\Delta\sigma_{\text{eq}}$, MPa	660	858	1107	1025	875
ΔL_{ohr} , %	.3952	.7220	.8666	1.075	.5122

TABLE 2-A

Spec. No.	6	7	8	9	10
Temp., °C	RT	RT	RT	RT	649
Spec. O.D., mm.	16.528	17.790	17.808	17.821	17.762
Spec. I.D., mm.	12.667	12.649	12.644	12.70	12.667
G.L., mm.	30.48	25.4	25.4	25.4	27.94
E, MPa $\times 10^3$	193	193	193	193	156
G, MPa $\times 10^3$	79.4	79.4	79.4	79.4	61
ν	0.4	0.4	0.4	0.4	0.4
λ			0	1.5	
ϕ , degrees	0	0	0	0	0
N_f , cycles	3,830	30,000	2,382	16,169	1,908
$\Delta\epsilon$, %	0	0	1.35	.763	0
$\Delta\gamma$, %	2.111	1.568	0	1.07	2.361
ΔP , KN	0	0	127	95	0
ΔT , N·m	607	520	0	304	581
ΔS , MPa	0	0	1030	722	0
ΔT , MPa	987	550	0	322	621
$\Delta\epsilon_p$, %	0	0	.8124	.3435	0
$\Delta\gamma_p$, %	.967	.747	0	.5788	1.788
ΔW_p^E , KJ/m ³	0	0	6,329	1,862	0
ΔW_p^Y , KJ/m ³	7,391	2,875	0	1,351	6,171
ΔW_p , KJ/m ³	7,391	2,875	6,329	3,213	6,171
ΔW_p^* , KJ/m ³	3,696	1,438	6,329	2,537	3,089
$\Delta\gamma_{oct}$, %	1.9403	1.2806	1.7835	1.3322	1.9278
$\Delta\gamma_{max}$, %	2.3764	1.5684	1.892	1.511	2.361

TABLE 2-B

Spec. No.	6	7	8	9	10
$\Delta\gamma_{\max}^D, \%$	1.223	.879	1.247	.899	1.366
$\Delta\epsilon_n, \%$	0	0	.4054	.2181	0
$\psi_{\max}, \text{degrees}$	0	0	45	68	0
$\Delta\epsilon_1, \%$	1.188	.784	1.351	.9839	1.181
$\Delta\gamma_{\epsilon}, \%$	0	0	0	.0283	0
$\alpha_{\max}, \text{degrees}$	45	45	0	23	45
$\Delta\sigma_1, \text{MPa}$	934	550	1030	885	621
$\Delta\tau_{\sigma}, \text{MPa}$	0	0	0	24	0
$\Delta\tau_{\max}, \text{MPa}$	934	550	515	500	621
$\Delta\sigma_n, \text{MPa}$	0	0	515	383	0
$\Delta\tau_{\text{oct}}, \text{MPa}$	762	449	486	447	507
$\Delta\sigma_{\text{oct}}, \text{MPa}$	0	0	343	257	0
$\Delta\sigma_{\text{eq}}, \text{MPa}$	1617	953	1030	948	1075
$\Delta L_{\text{ohr}}, \%$.7129	.4705	1.0269	.7123	.7083

TABLE 3-A

Spec. No.	14	18	19	20	21
Temp., °C	RT	649	649	649	649
Spec. O.D., mm.	17.803	17.808	17.823	17.816	17.810
Spec. I.D., mm.	12.685	12.642	12.591	12.637	12.624
G.L., mm.	33.02	33.02	33.02	33.02	33.02
E, MPa $\times 10^3$	193	156	156	156	156
G, MPa $\times 10^3$	79.4	61	61	61	61
ν	0.4	0.4	0.4	0.4	0.4
λ	4.0			1.5	1.5
ϕ , degrees	0	0	0	90	90
N_f , cycles	22,124	15,920	3,000	5,750	522
$\Delta\epsilon$, %	.4085	0	0	.512	.9086
$\Delta\gamma$, %	1.567	1.165	2.059	.752	1.359
ΔP , KN	53	0	0	89	129
ΔT , N·m	453	415	517	375	571
ΔS , MPa	430	0	0	719	1040
$\Delta\tau$, MPa	481	437	538	394	600
$\Delta\epsilon_p$, %	.1701	0	0	.0886	.3141
$\Delta\gamma_p$, %	.8879	.4212	1.111	.0893	.4157
ΔW_p^E , KJ/m ³	483	0	0	462	2,620
ΔW_p^Y , KJ/m ³	2,916	1,386	4,847	248	1,931
ΔW_p , KJ/m ³	3,399	1,386	4,847	710	4,551
ΔW_p^* , KJ/m ³	1,944	696	2,427	586	3,585
$\Delta\sigma_{oct}$, %	1.387	.9514	1.682	.6992	1.2294
$\Delta\gamma_{max}$, %	1.667	1.165	2.059	.7667	1.381

TABLE 3-B

Spec. No.	14	18	19	20	21
$\Delta\gamma_{\max}^p$, %	1.028	.4565	1.193	.1169	.4342
$\Delta\epsilon_n$, %	.1234	0	0	.5138	.9047
ψ_{\max} , degrees	80	0	0	9	7
$\Delta\epsilon_l$, %	.955	.5826	1.030	.5153	.910
$\Delta\gamma_e$, %	.0245	0	0	.7613	1.37
α_{\max} , degrees	35	45	45	4	2
$\Delta\sigma_l$, MPa	741	437	538	719	1040
$\Delta\tau_{\sigma}$, MPa	50	0	0	42	39
$\Delta\tau_{\max}$, MPa	526	437	538	406	608
$\Delta\sigma_n$, MPa	214	0	0	124	150
$\Delta\tau_{\text{oct}}$, MPa	442	357	439	339	491
$\Delta\sigma_{\text{oct}}$, MPa	143	0	0	240	347
$\Delta\sigma_{\text{eq}}$, MPa	937	758	932	719	1041
ΔLohr , %	.6383	.3496	.6178	.2723	.4654

TABLE 4-A

Spec. No.	22	23	25	27	28
Temp., °C	649	649	649	649	649
Spec. O.D., mm	17.810	17.803	17.818	17.828	17.816
Spec. I.D., mm	12.611	12.621	12.649	12.639	12.639
G.L., mm.	33.02	33.02	33.02	33.02	33.02
E, MPa $\times 10^3$	156	156	156	156	156
G, MPa $\times 10^3$	61	61	61	61	61
ν	0.4	0.4	0.4	0.4	0.4
λ	1.5	1.5	1.5	1.5	1.5
ϕ , degrees	0	0	NP	NP	NP
N_f , cycles	1,763	21,364	7,589	1,119	1,247
$\Delta\epsilon$, %	.6497	.3975	.5117	.9962	.9962
$\Delta\gamma$, %	.9466	.5744	.7447	1.4676	1.4996
ΔP , KN	84	65	86	139	140
ΔT , N·m	267	234	361	594	610
ΔS , MPa	675	527	695	1,123	1,127
$\Delta\tau$, MPa	280	246	380	622	641
$\Delta\epsilon_p$, %	.2573	.0717	.0846	.3116	.2761
$\Delta\gamma_p$, %	.4322	.1391	.0863	.3739	.3618
ΔW_p^E , KJ/m ³	1,344	276	469	2,730	2,586
ΔW_p^Y , KJ/m ³	972	234	165	1,641	1,772
ΔW_p , KJ/m ³	2,317	503	634	4,371	4,357
ΔW_p^* , KJ/m ³	1,834	393	552	3,551	3,475
$\Delta\gamma_{oct}$, %	1.1545	.7037	.6755	1.3149	1.3149
$\Delta\gamma_{max}$, %	1.3128	.7997	.7447	1.4676	1.4996

TABLE 4-B

Spec. No.	22	23	25	27	28
$\Delta\gamma_{\max}^p$, %	.6135	.2169	.1476	.4871	.4732
$\Delta\epsilon_n$, %	.1981	.1198	0	0	0
ψ_{\max} , degrees	68	68	0	0	0
$\Delta\epsilon_1$, %	.8513	.5191	.5117	.9962	.9962
$\Delta\gamma_e$, %	.0271	.0164	0	0	0
α_{\max} , degrees	23	23	0	0	0
$\Delta\sigma_1$, MPa	774	622	695	1123	1127
$\Delta\tau_{\sigma}$, MPa	17	5	0	0	0
$\Delta\tau_{\max}$, MPa	437	359	380	622	641
$\Delta\sigma_n$, MPa	333	257	0	0	0
$\Delta\tau_{\text{oct}}$, MPa	390	318	328	529	531
$\Delta\sigma_{\text{oct}}$, MPa	225	176	232	374	376
$\Delta\sigma_{\text{eq}}$, MPa	828	674	695	1123	1127
ΔLohr , %	.6147	.3751	.3889	.7571	.7571

TABLE 5-A

Spec. No.	29	30	31	32	33
Temp., °C	649	649	649	649	649
Spec. O.D., mm.	17.810	17.770	17.803	17.828	17.813
Spec. I.D., mm.	12.639	12.614	12.631	12.690	12.708
G.L., mm.	33.02	33.02	33.02	33.02	33.02
E, MPa $\times 10^3$	156	156	156	156	156
G, MPa $\times 10^3$	61	61	61	61	61
ν	0.4	0.4	0.4	0.4	0.4
λ	1.5	1.5	1.5	1.5	1.5
ϕ , degrees	NP	NP	NP	NP	NP
N_f , cycles	11,715	2,700	77,000	2,300	10,279
$\Delta\epsilon$, %	.5117	.703	.3811	.7035	.4967
$\Delta\gamma$, %	.7377	1.021	.5738	1.0203	.7166
ΔP , KN	86	105	71	105	84
ΔT , N·m	366	444	299	447	350
ΔS , MPa	698	851	575	851	685
$\Delta\tau$, MPa	385	470	315	471	371
$\Delta\epsilon_p$, %	.0822	.1788	.0110	.2075	.0952
$\Delta\gamma_p$, %	.0913	.2073	.0605	.2112	.1136
ΔW_p^E , KJ/m ³	427	1,338	159	1,276	455
ΔW_p^Y , KJ/m ³	172	621	48	641	193
ΔW_p , KJ/m ³	600	1,958	207	1,917	648
ΔW_p^* , KJ/m ³	510	1,648	179	1,600	552
$\Delta\gamma_{oct}$, %	.6755	.930	.5049	.9308	.6577
$\Delta\gamma_{max}$, %	.7377	1.021	.5738	1.0203	.7166

TABLE 5-B

Spec. No.	29	30	31	32	33
$\Delta\gamma_{\max}^p$, %	.1468	.2776	.0788	.2842	.1340
$\Delta\epsilon_n$, %	0	.703	.3811	.703	.4967
ψ_{\max} , degrees	0	0	0	0	0
$\Delta\epsilon_1$, %	.5117	.7032	.3811	.7040	.4969
$\Delta\gamma_e$, %	0	1.02	.5734	1.02	.7162
α_{\max} , degrees	0	1	1	1	1
$\Delta\sigma_1$, MPa	698	851	575	851	685
$\Delta\tau_{\sigma}$, MPa	0	58	15	49	24
$\Delta\tau_{\max}$, MPa	385	478	315	480	374
$\Delta\sigma_n$, MPa	0	83	8	83	39
$\Delta\tau_{\text{oct}}$, MPa	329	401	271	401	323
$\Delta\sigma_{\text{oct}}$, MPa	233	284	192	284	228
$\Delta\sigma_{\text{eq}}$, MPa	698	851	575	851	685
ΔLohr , %	.3889	.4300	.1721	.4297	.3051

TABLE 6-A

Spec. No.	34	35	36
Temp., °C	649	649	649
Spec. O.D., mm.	17.785	17.805	17.810
Spec. I.D., mm.	12.611	12.677	12.713
G.L., mm.	33.02	33.02	33.02
E, MPa $\times 10^3$	156	156	156
G, MPa $\times 10^3$	61	61	61
ν	0.4	0.4	0.4
λ	1.5	1.5	1.5
ϕ , degrees	0	0	
N_f , cycles	2,533	2,150	2,308
$\Delta\epsilon$, %	.5977	.594	0
$\Delta\gamma$, %	.8790	.8704	2.3638
ΔP , KN	75	78	0
ΔT , N·m	273	279	541
ΔS , MPa	611	639	0
$\Delta\tau$, MPa	288	295	575
$\Delta\epsilon_p$, %	.2091	.2058	0
$\Delta\gamma_p$, %	.3771	.3728	1.4122
ΔW_p^E , KJ/m ³	1,027	1,069	0
ΔW_p^Y , KJ/m ³	834	841	6,357
ΔW_p , KJ/m ³	1,862	1,910	6,357
ΔW_p^* , KJ/m ³	1,448	1,489	3,178
$\Delta\gamma_{oct}$, %	1.066	1.058	1.930
$\Delta\gamma_{max}$, %	1.213	1.204	2.3638

TABLE 6-B

Spec. No.	34	35	36
$\Delta\gamma_{\max}^p, \%$.5413	.5180	1.4678
$\Delta\epsilon_n, \%$.1862	.1839	0
$\psi_{\max}, \text{degrees}$	68	68	0
$\Delta\epsilon_1, \%$.7858	.7801	1.1819
$\Delta\gamma_{\epsilon}, \%$.0292	.0265	0
$\alpha_{\max}, \text{degrees}$	23	23	45
$\Delta\sigma_1, \text{MPa}$	725	751	575
$\Delta\tau_{\sigma}, \text{MPa}$	24	12	0
$\Delta\tau_{\max}, \text{MPa}$	419	432	575
$\Delta\sigma_n, \text{MPa}$	300	308	0
$\Delta\tau_{\text{oct}}, \text{MPa}$	371	383	469
$\Delta\sigma_{\text{oct}}, \text{MPa}$	204	213	0
$\Delta\sigma_{\text{eq}}, \text{MPa}$	788	812	995
$\Delta L_{\text{ohr}}, \%$.5672	.5631	.7091

Table 7

(Tests at RT)

<u>Theories</u>	<u>Correlation Coefficient</u>
ΔW_p	-.9561
ΔW_p^*	-.9450
$\Delta \epsilon_1$	-.9326
$\Delta \gamma_{oct}$	-.8989
$\Delta Lohr$	-.8835
$\Delta \gamma_{max}$	-.8129
$\Delta \gamma_{max}^p$	-.7850
$\Delta \sigma_1$	-.6761
$\Delta \tau_{oct}$	-.6223
$\Delta \tau_{max}$	-.5120

Table 8

(Tests at 649°C)

<u>Theories</u>	<u>Correlation Coefficient</u>
ΔW_p^*	-.9364
ΔW_p	-.8967
$\Delta \tau_{oct}$	-.8873
$\Delta \epsilon_1$	-.8613
$\Delta \tau_{max}$	-.8602
$\Delta \gamma_{oct}$	-.7870
ΔL_{ohr}	-.7719
$\Delta \gamma_{max}$	-.7480
$\Delta \sigma_1$	-.6952
$\Delta \gamma_{max}^p$	-.6711

TABLE 9

Spec. No.	σ_B , Mpa	$\frac{\sigma_B}{\sigma_{max}}$, %	σ_C , Mpa	$\frac{\sigma_C}{\sigma_{max}}$, %	σ_{max} , Mpa
25	49	14.7	36	10.8	333
27	197	37.3	116	22	528
28	198	35	121	21.4	566
29	54	15.8	36	10.5	342

where

σ_B = tensile or compressive stress at the beginning of torsion cycle.

σ_C = tensile or compressive stress at the end of torsion cycle.

σ_{max} = the maximum tensile or compressive stress at the axial cycle.

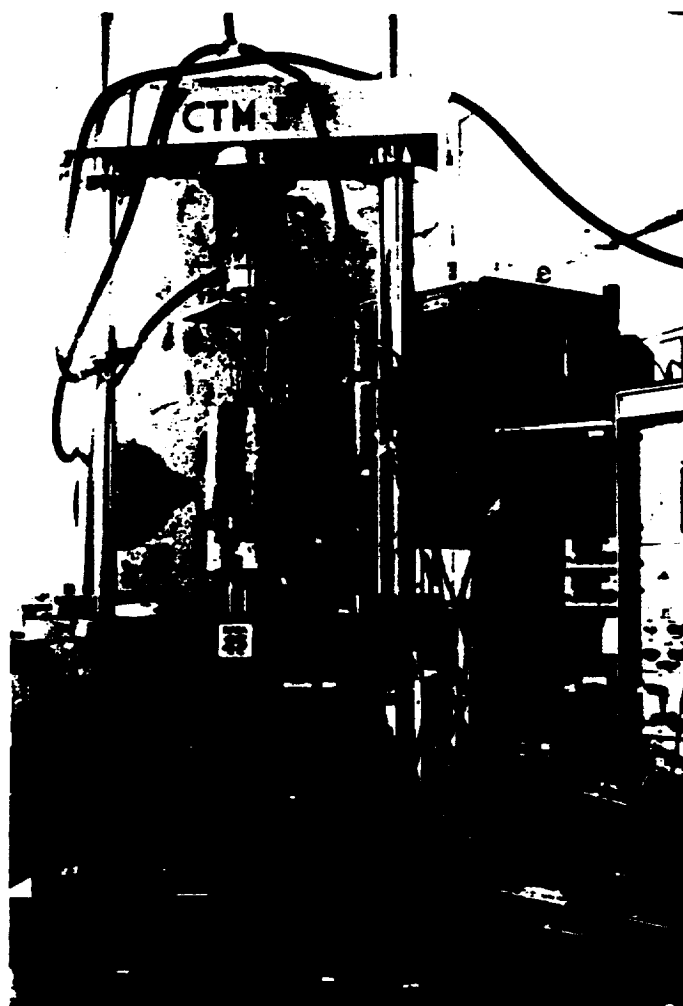


Figure 1. The testing machine

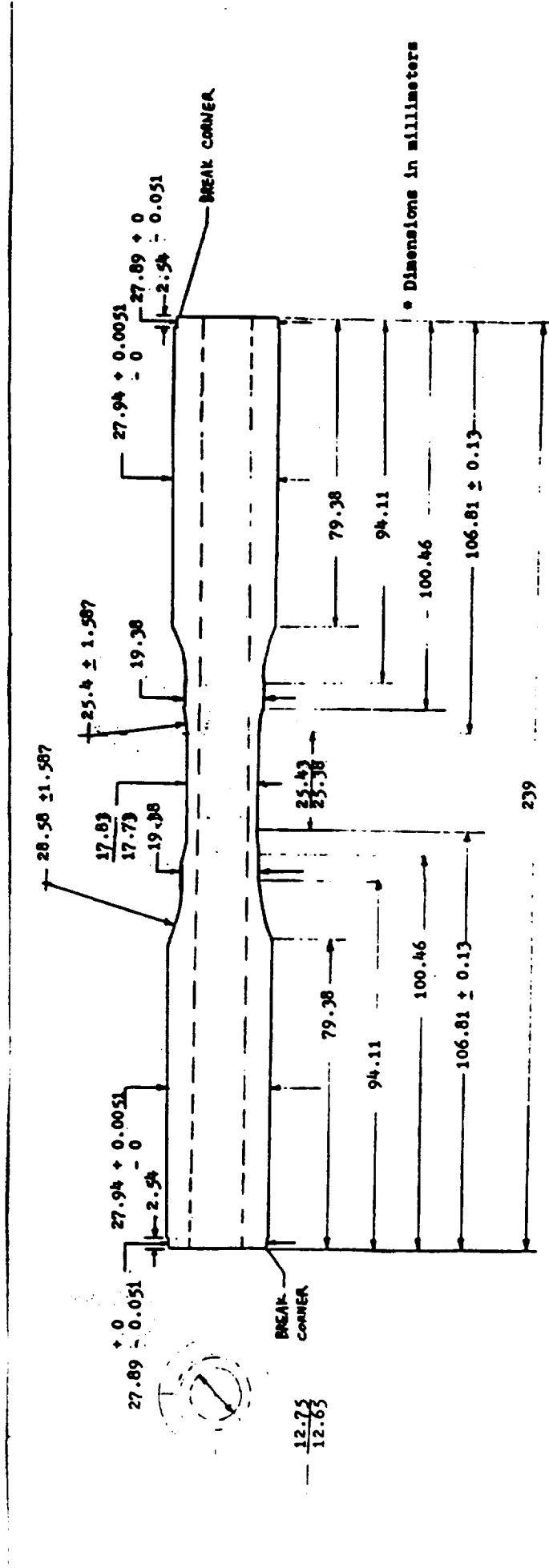


Figure 2. Specimen geometry

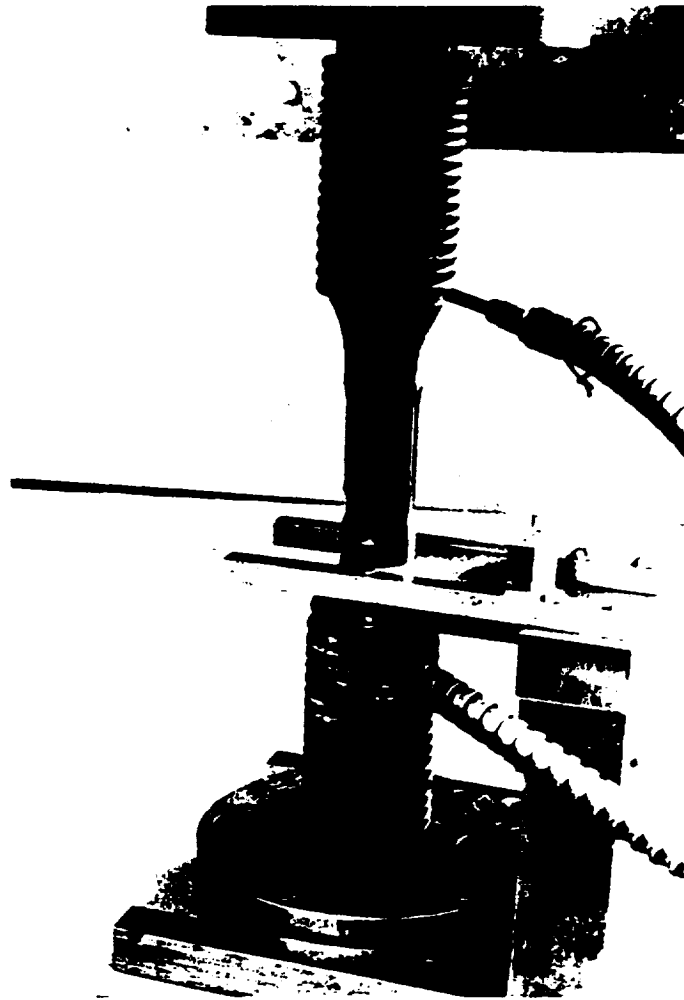


Figure 3. Specimen, grips, band heaters and jig for mounting the extensometer.

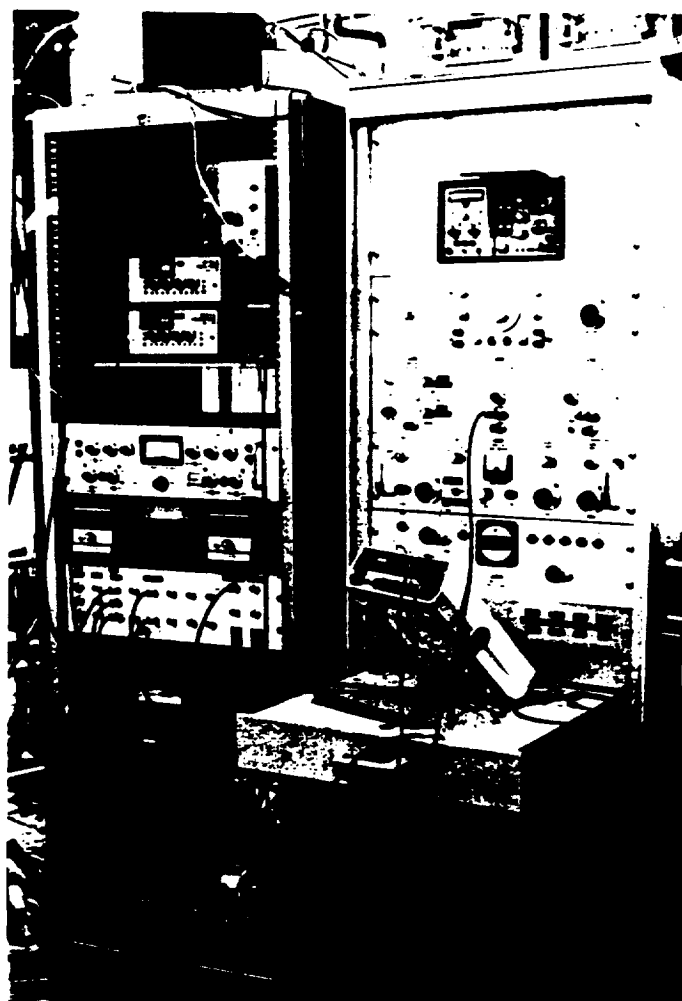


Figure 4. Servo-electronics

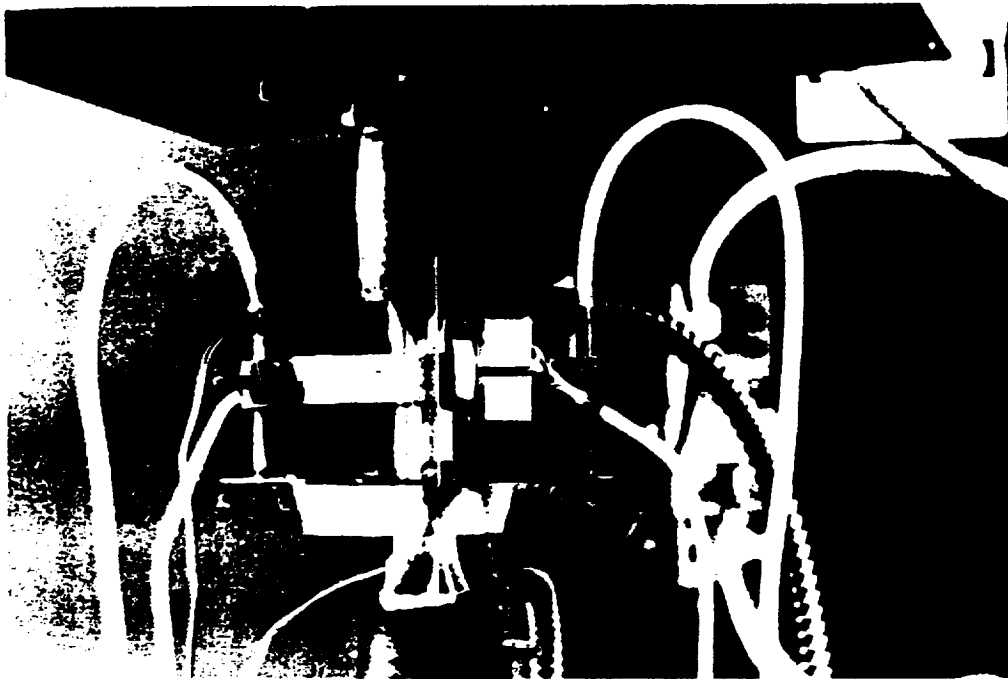


Figure 5. Extensometer with axial and torsional capacitance displacement probes.

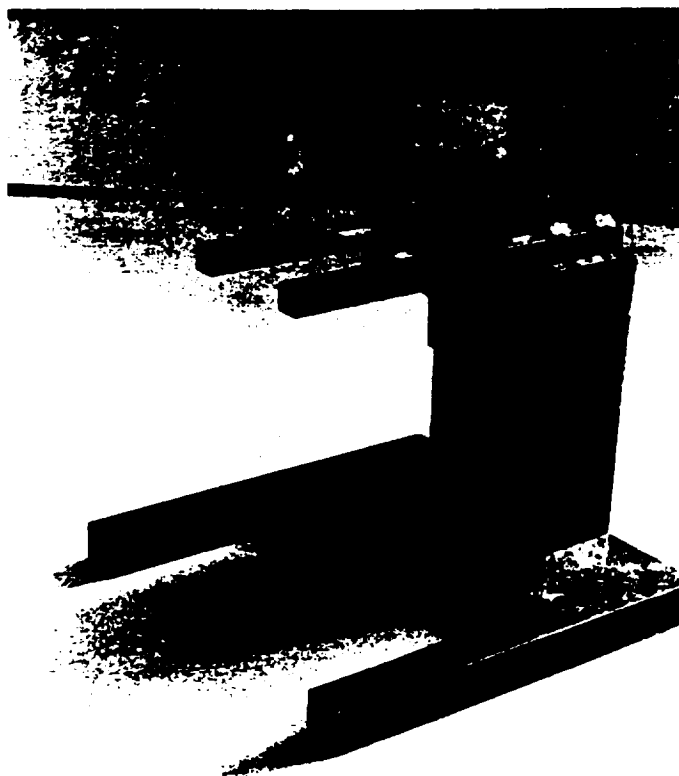


Figure 6. Jig for mounting the extensometer.

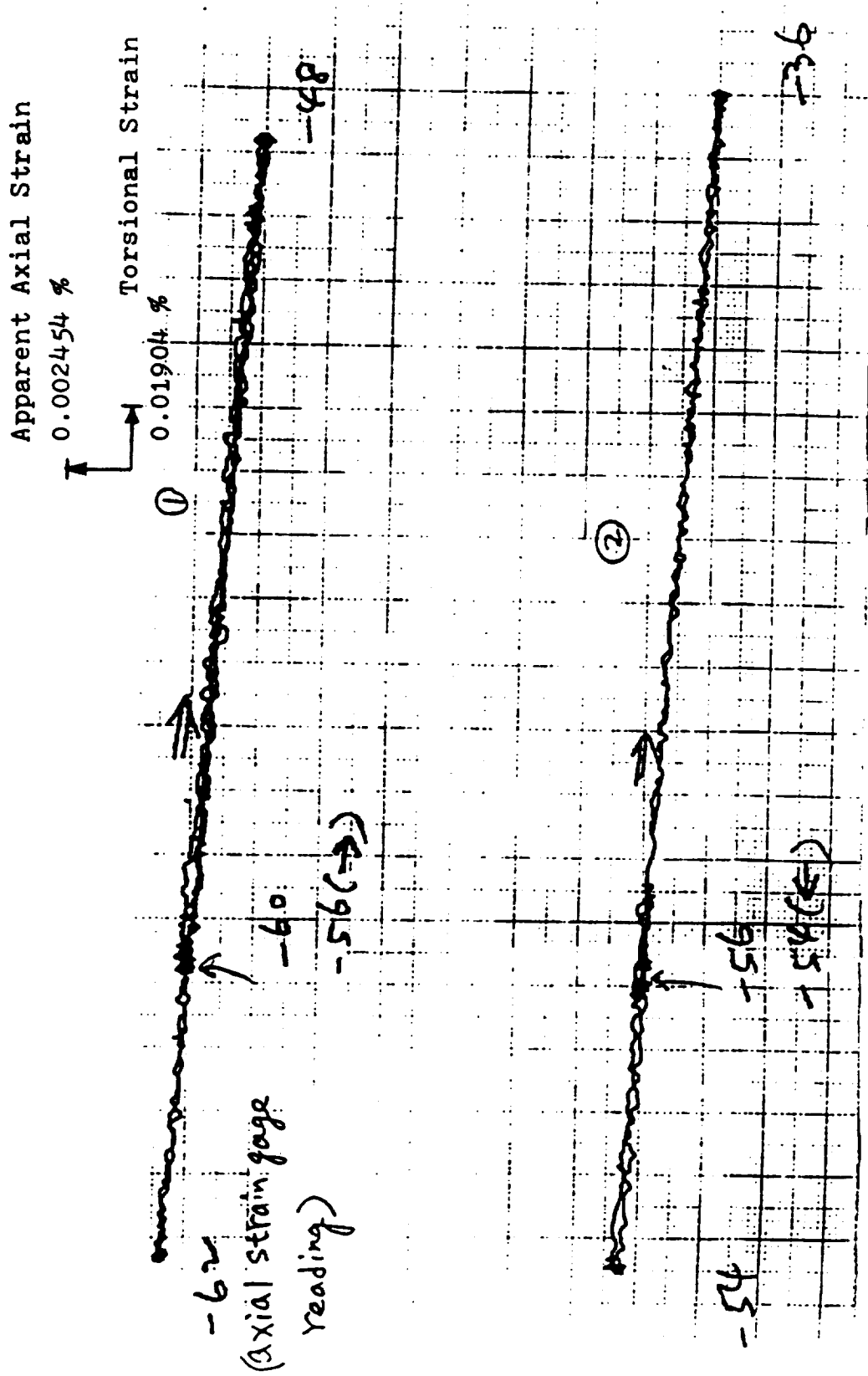


Figure 7. The cross talk to axial strain

Apparent Torsional Strain

0.0006416 %

Axial Strain

0.064231 %

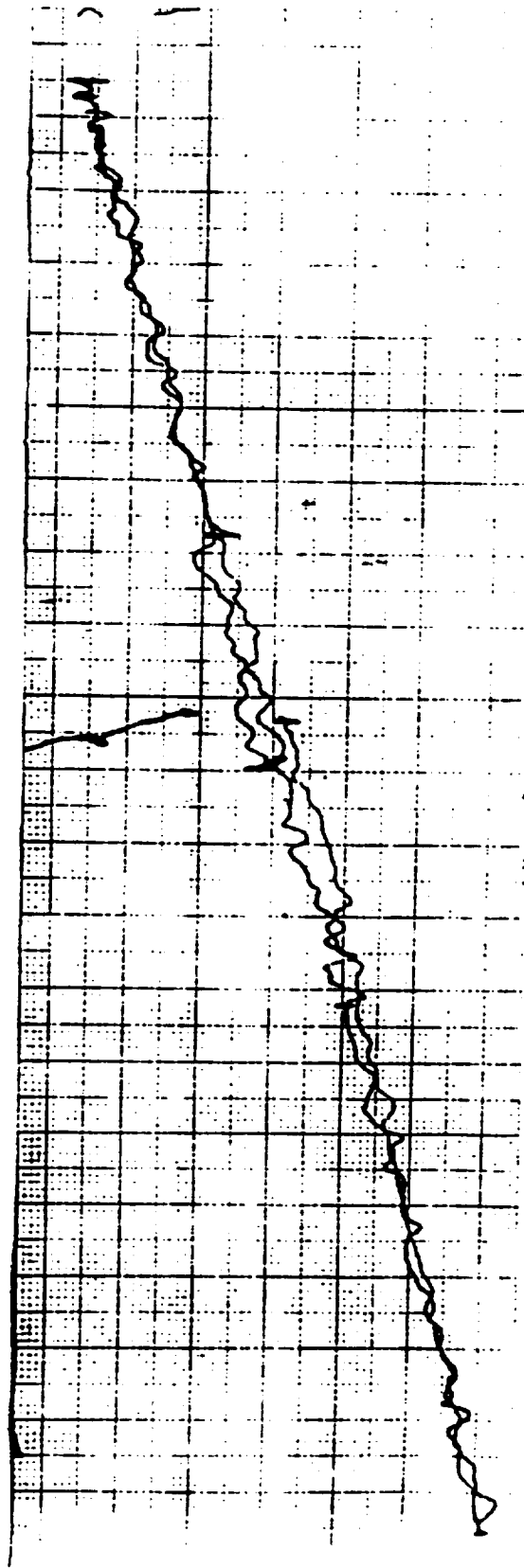


Figure 8. The cross talk to torsional strain

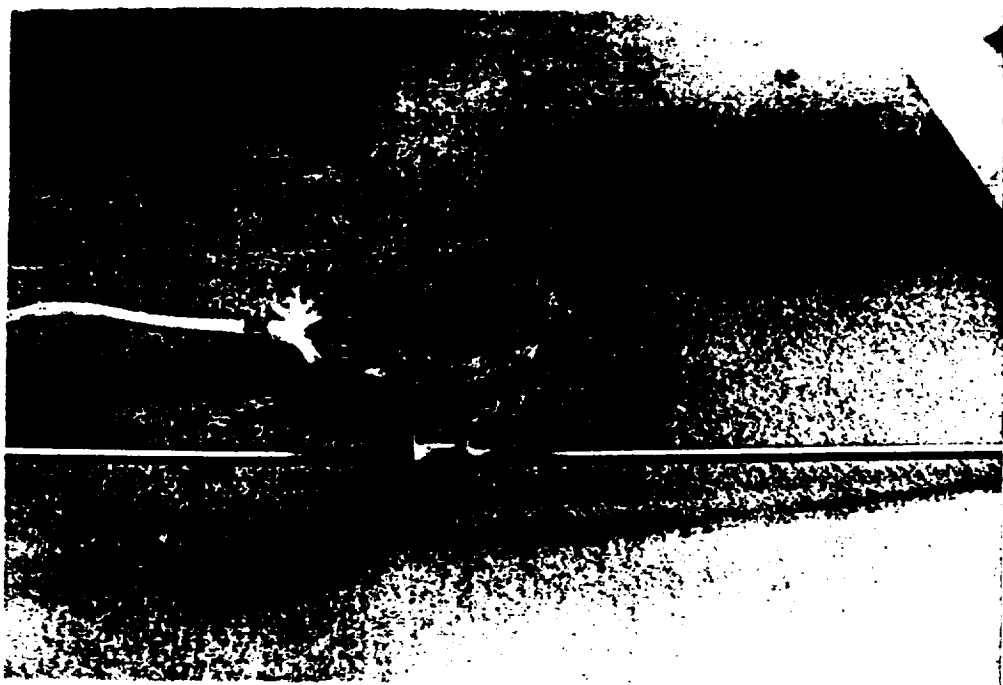


Figure 9. Outer and inner ring probes.

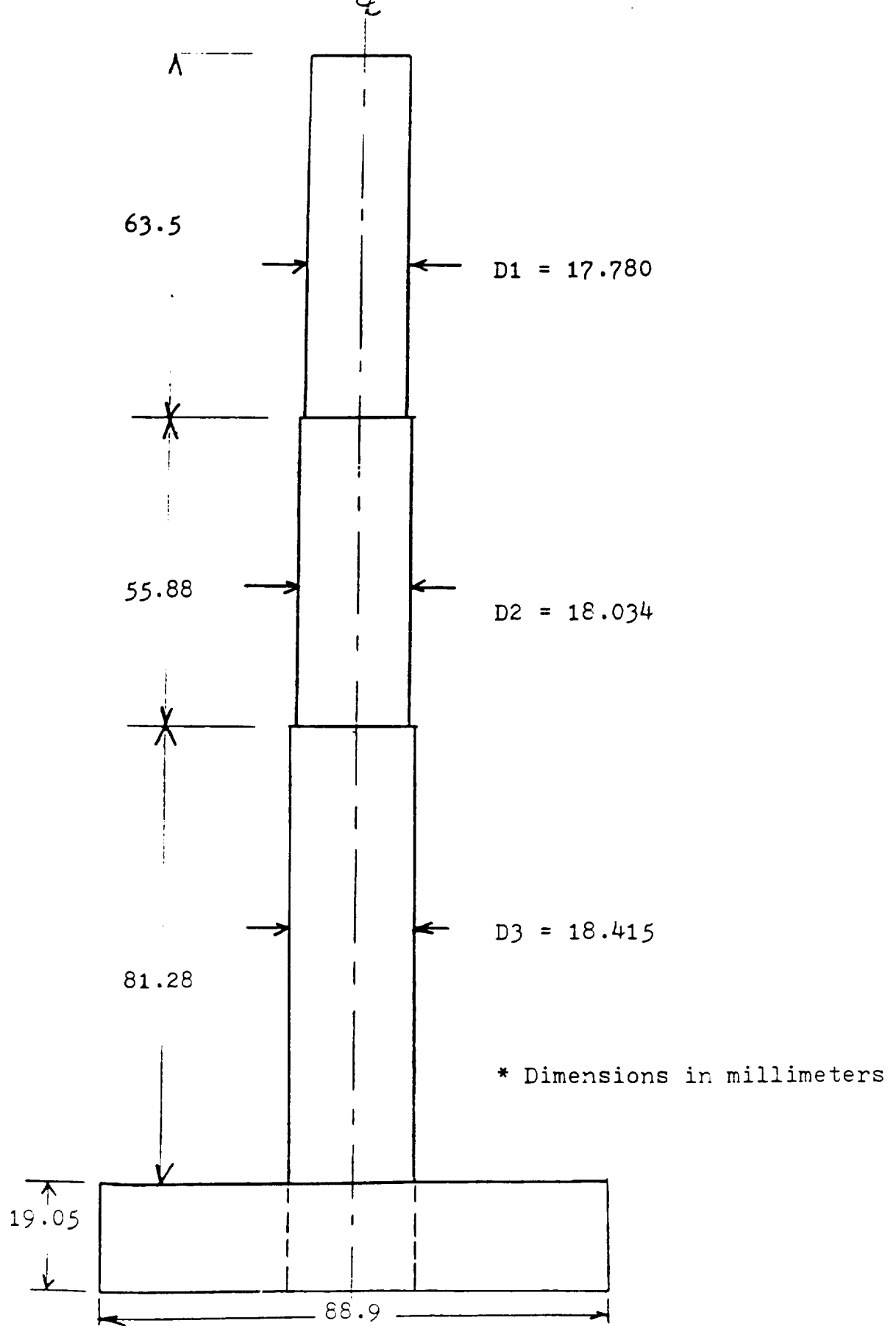


Figure 10. Calibration jig for outer ring probe.

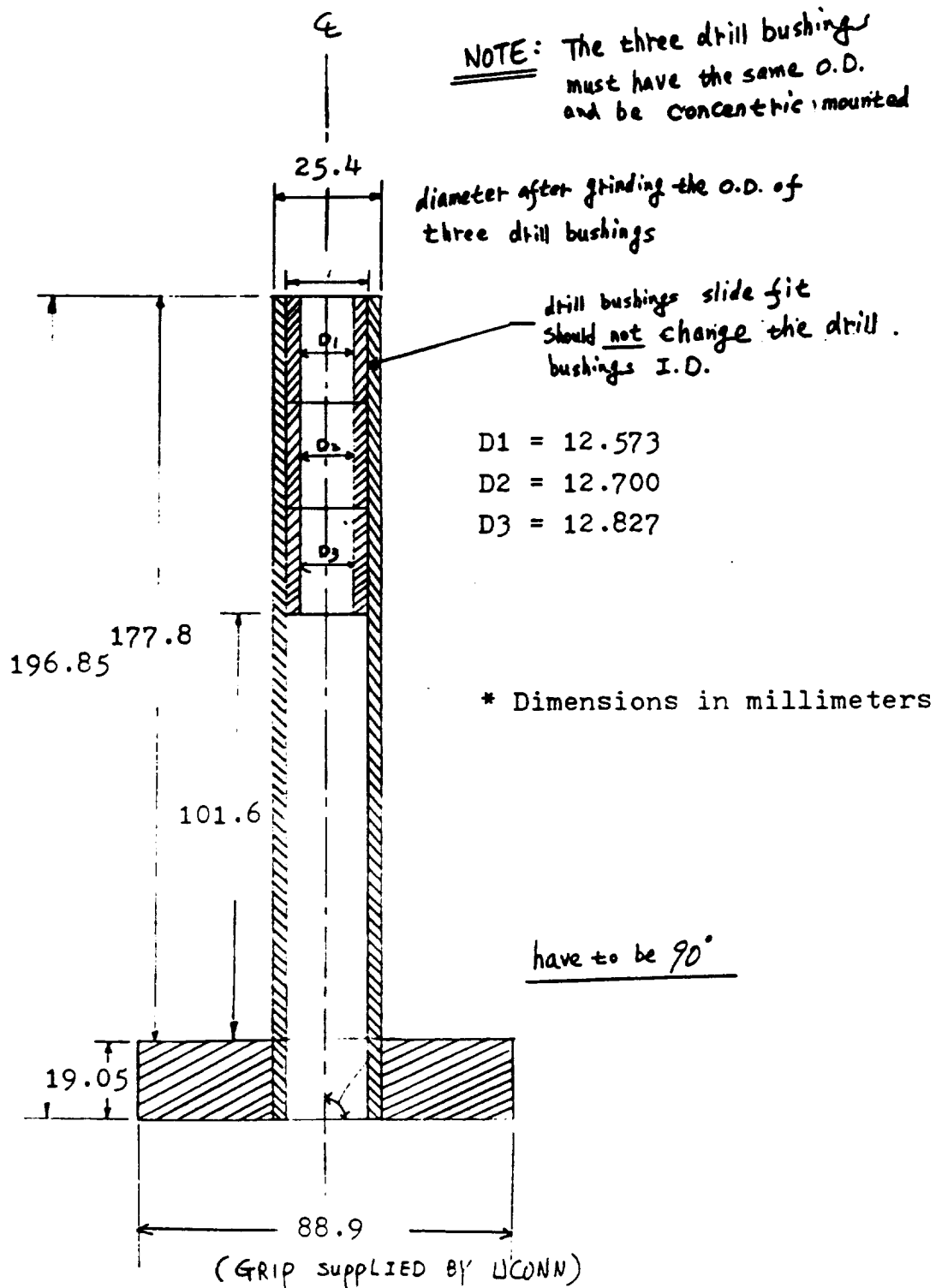


Figure 11. Calibration jig for inner ring probe.

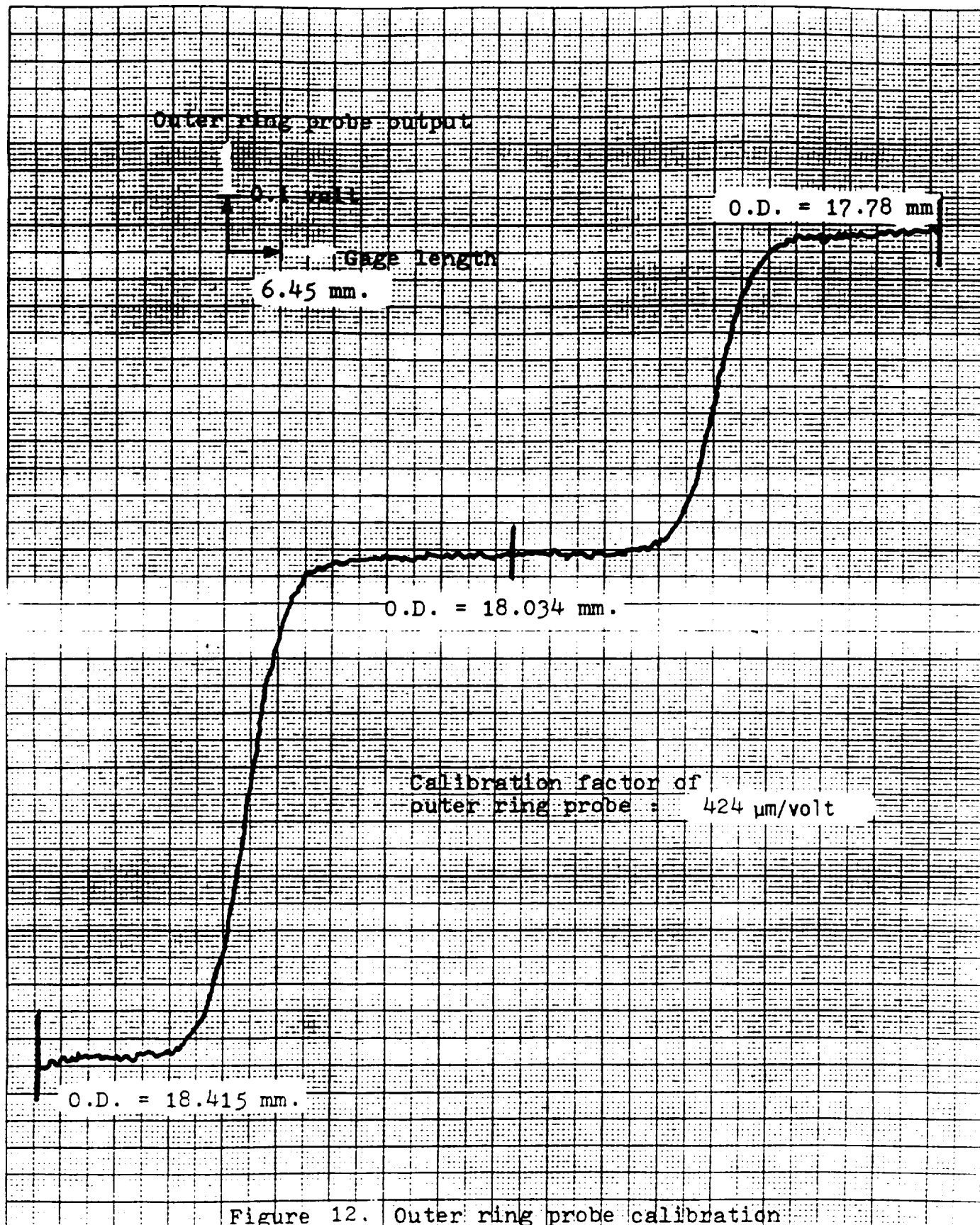


Figure 12. Outer ring probe calibration

1515
CENTIMETER
EL &
CO
1515

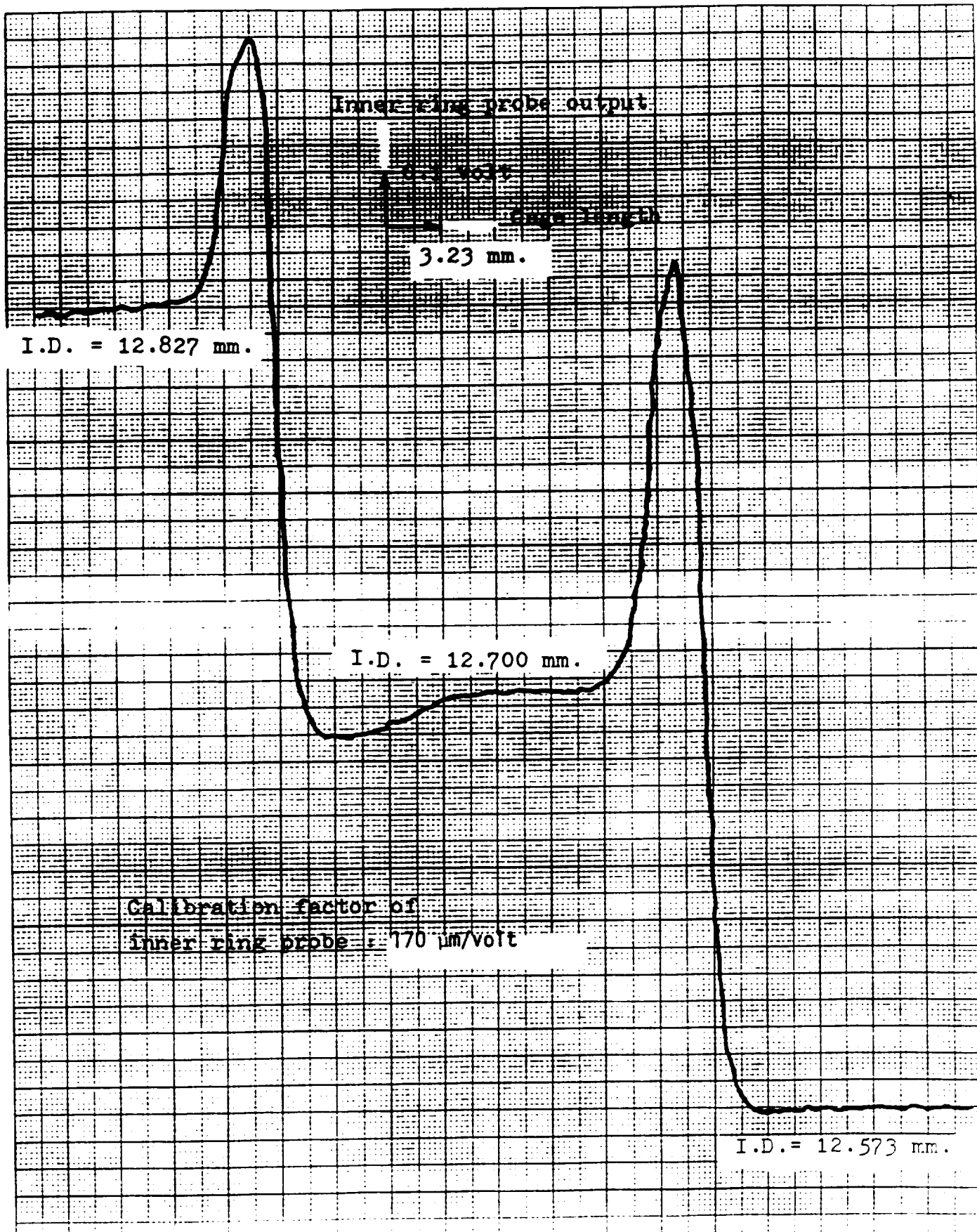


Figure 13. Inner ring probe calibration

Apparent O.D. change

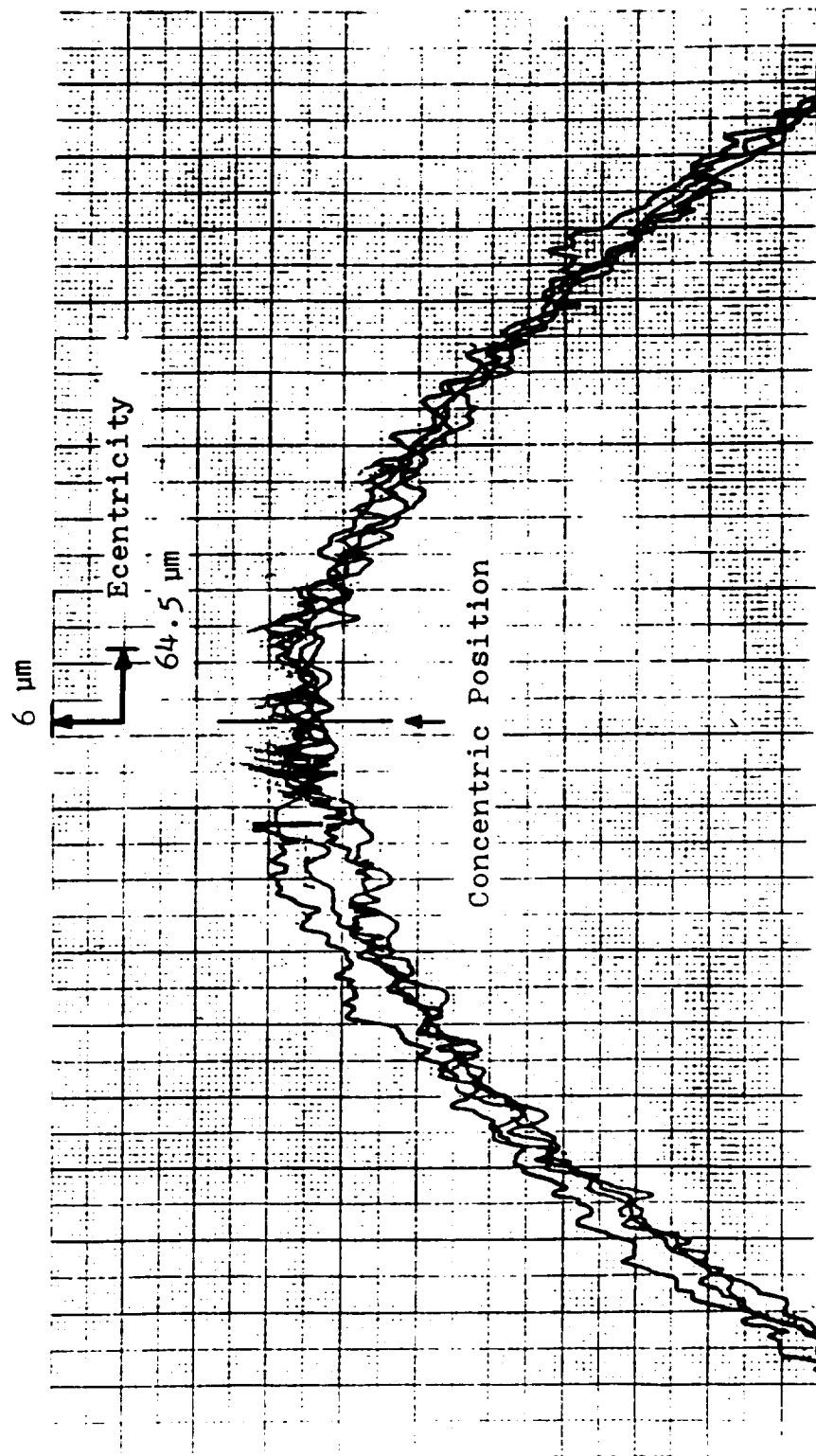


Figure 14. Apparent O.D. change due to eccentricity

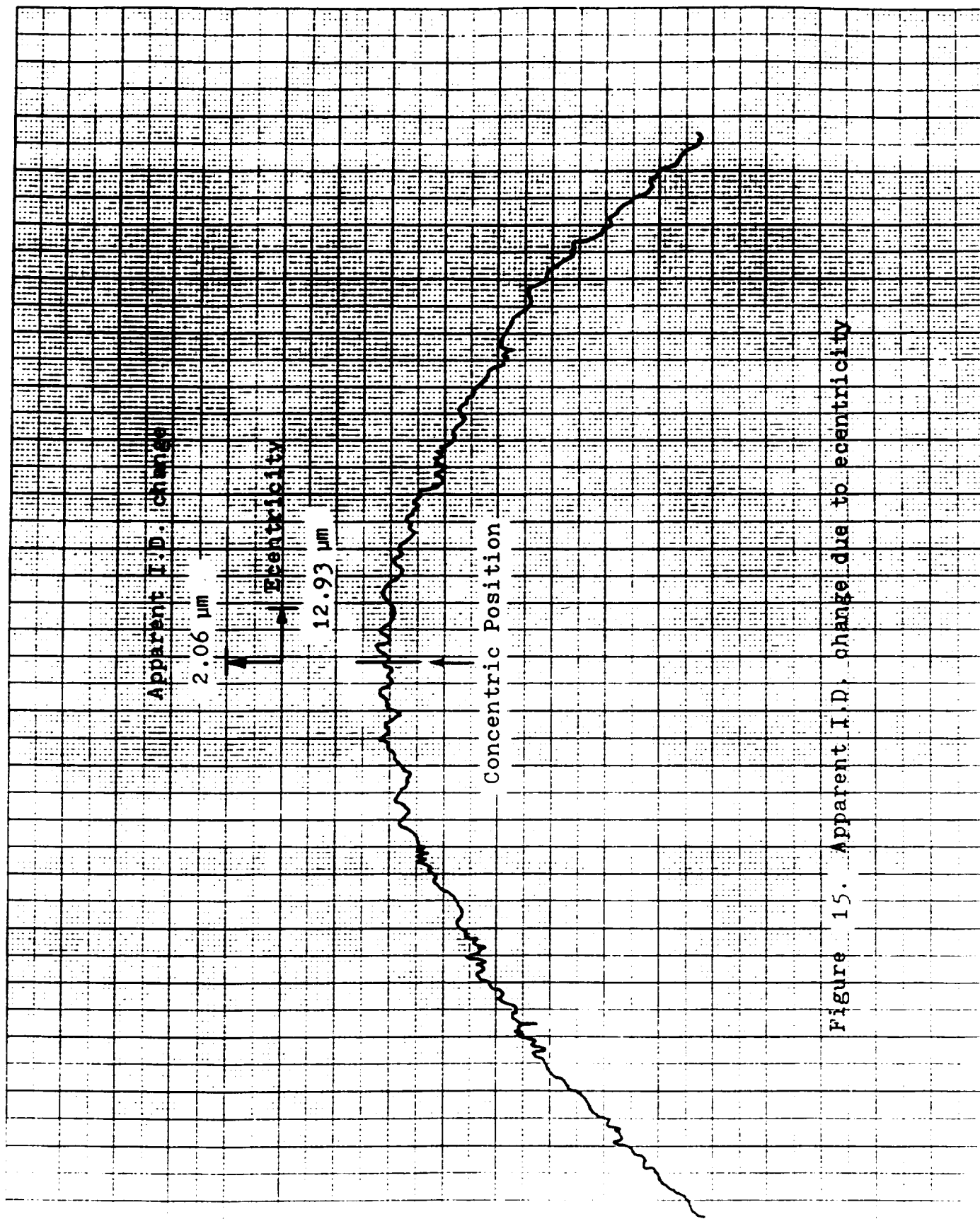


Figure 15. Apparent I.D. change due to eccentricity

① : Gage O.D. = 18.034 mm. & 17.780 mm.

② : Gage O.D. = 18.415 mm. & 18.034 mm.

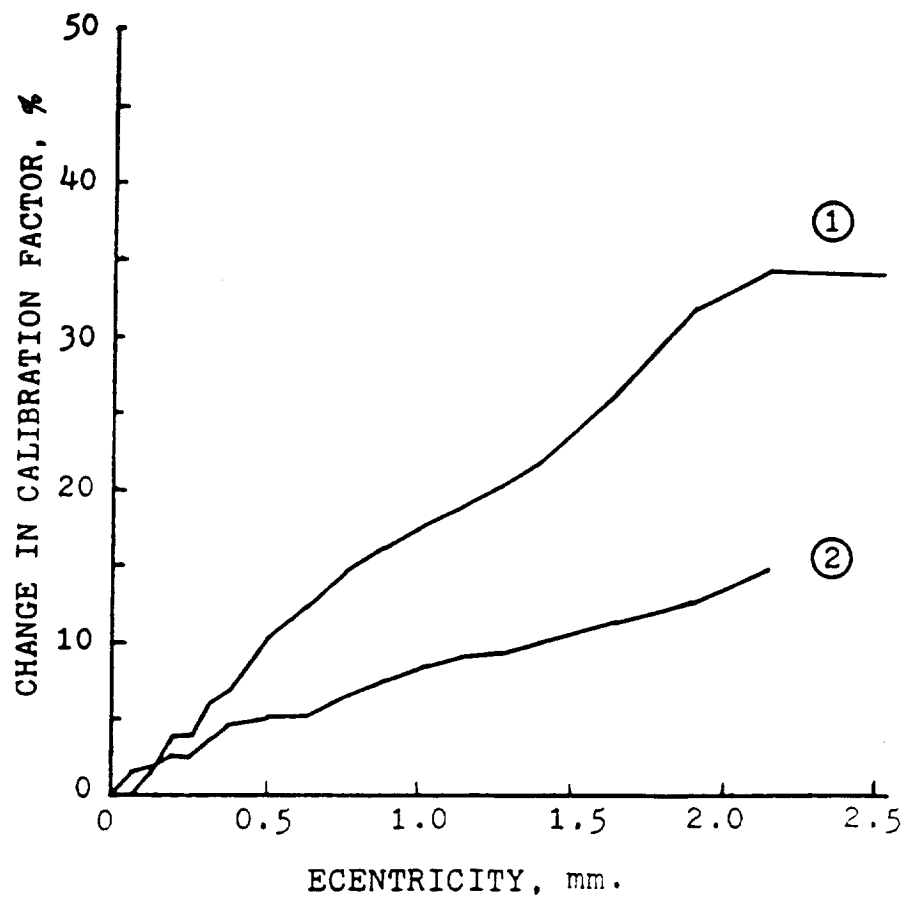


Figure 16. Effect on the calibration factor of outer ring probe due to eccentricity.

① : Gage I.D. = 12.7 mm. & 12.827 mm.

② : Gage I.D. = 12.573 mm. & 12.7 mm.

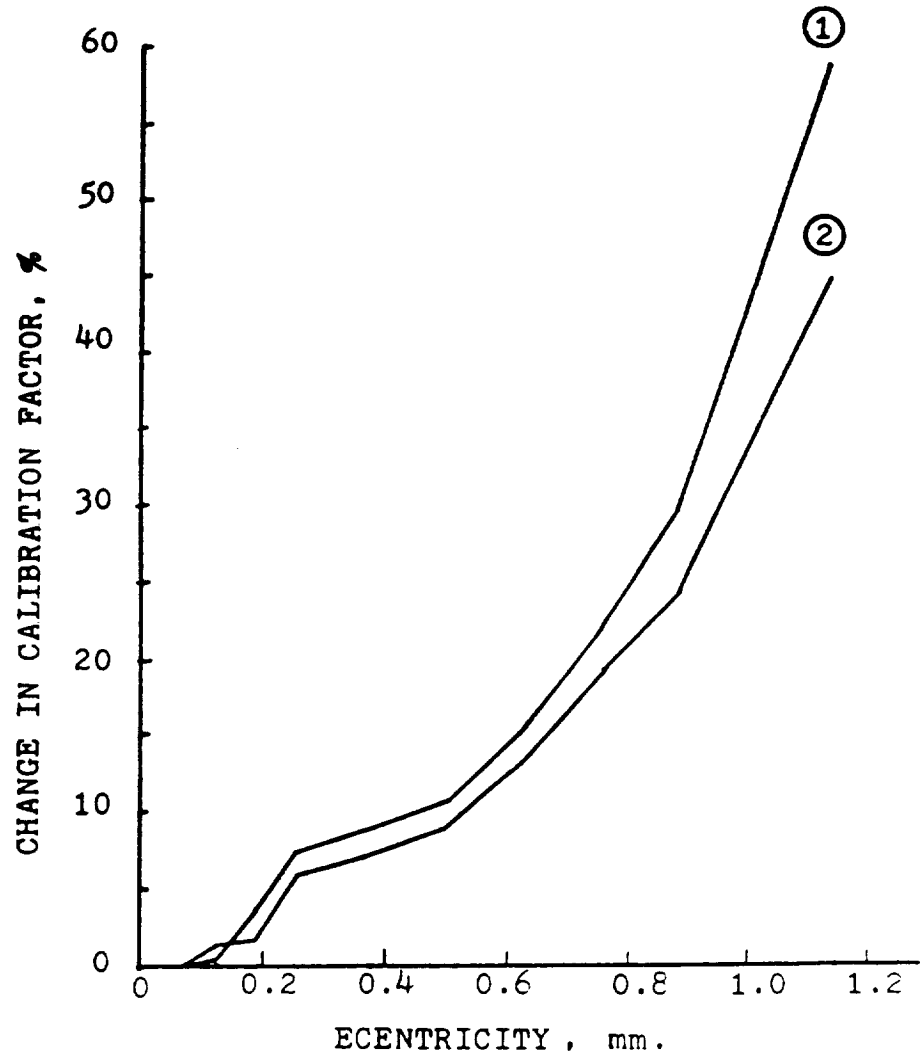


Figure 17. Effect on the calibration factor of inner ring probe due to eccentricity.

● : Specimens cut from the longitudinal direction

▲ : Specimens cut from the transverse direction

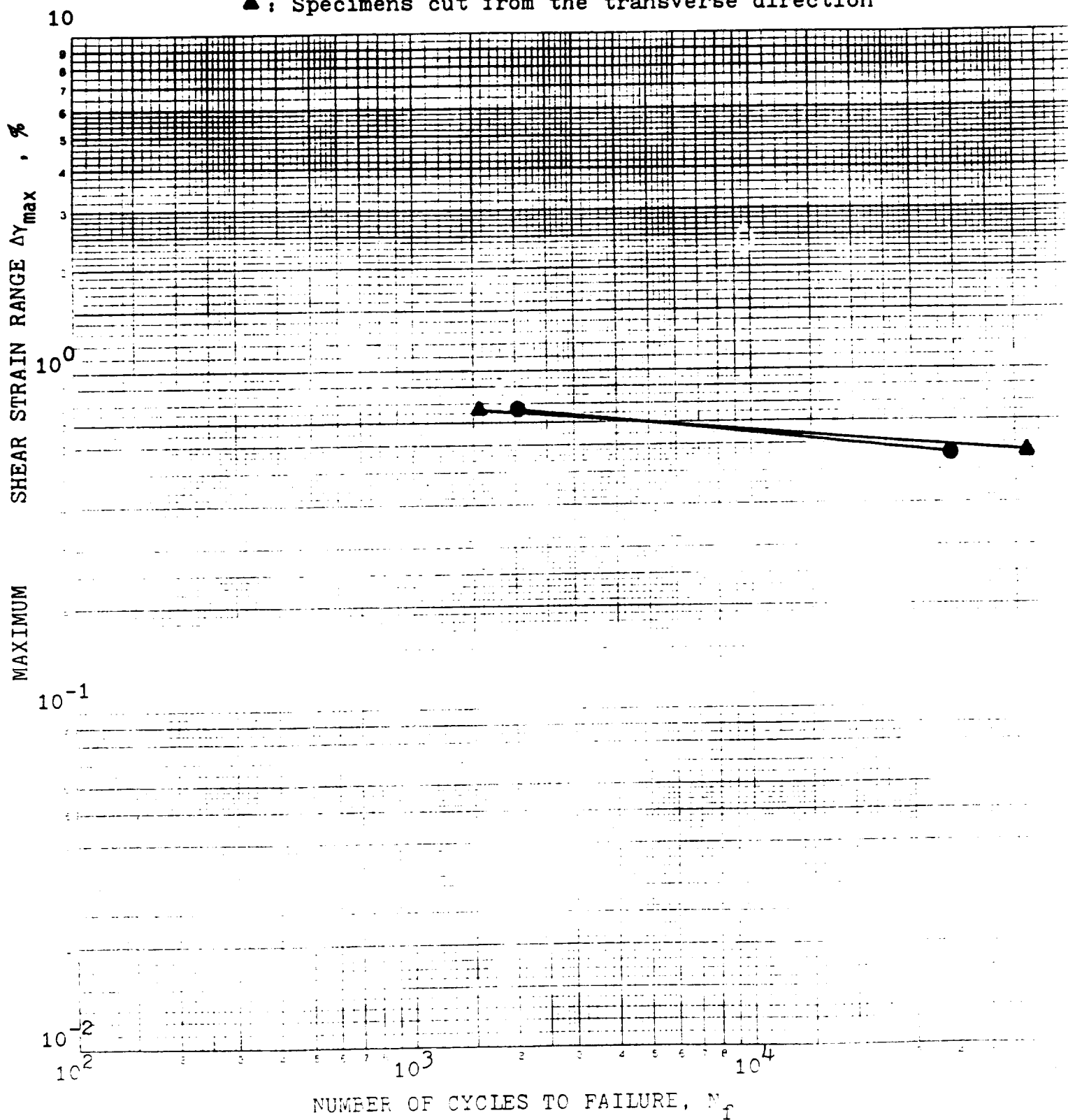


Figure 18. Maximum shear strain range versus cycles to failure

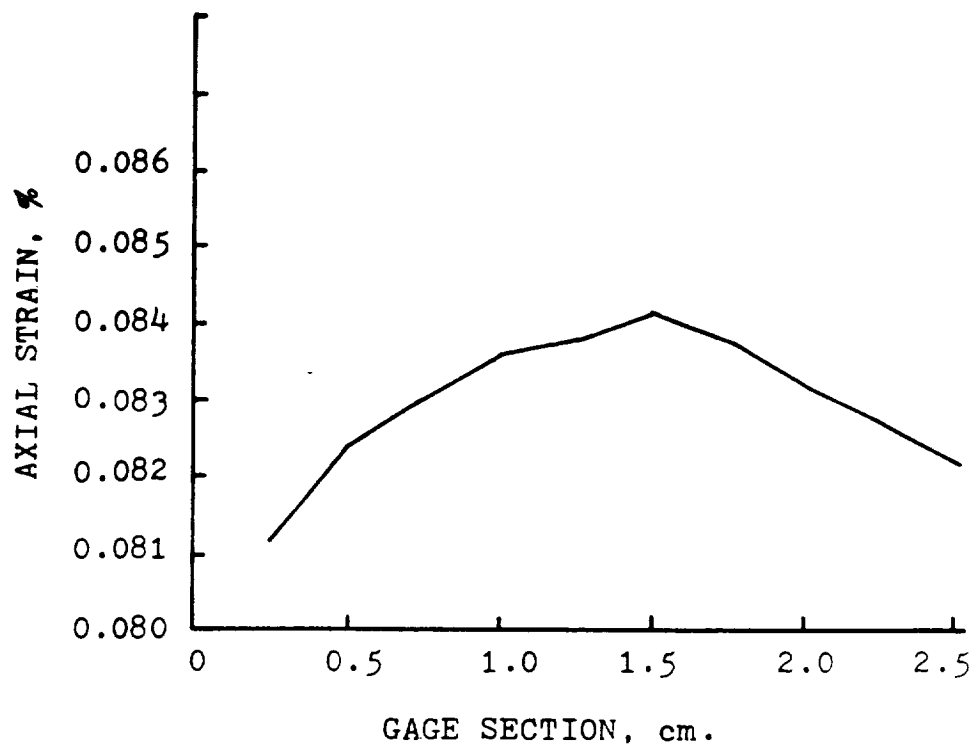


Figure 19. Strain distribution in the specimen gage section under an elastic tension-compression loading.

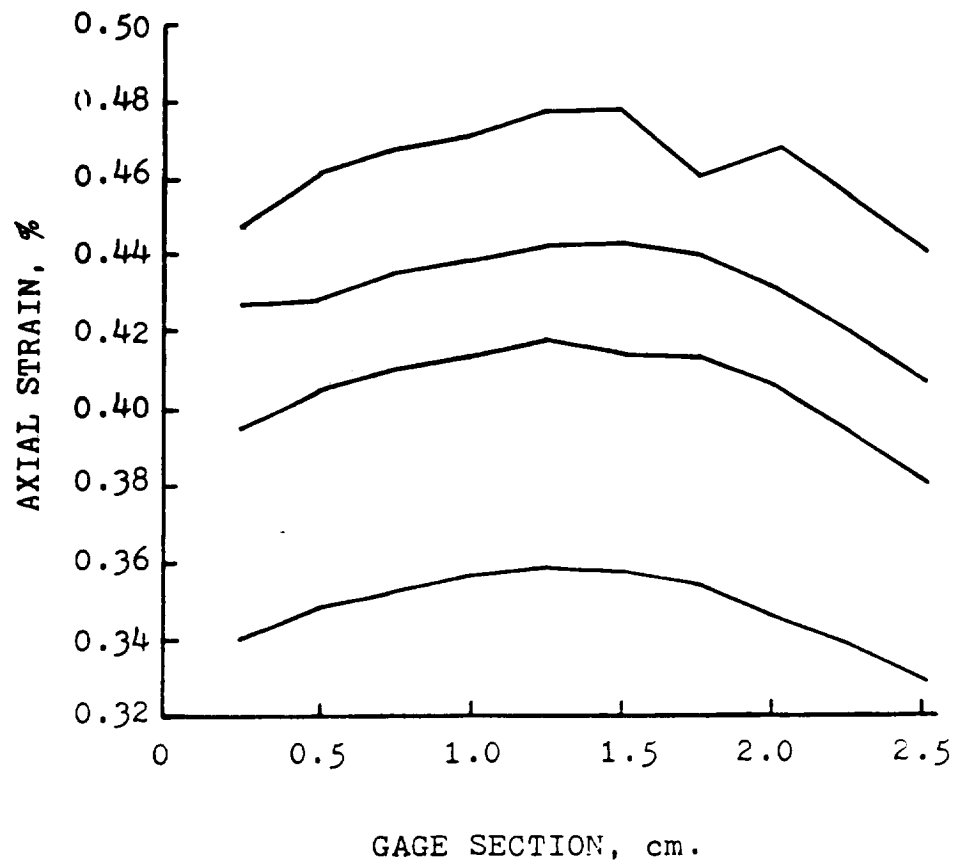


Figure 20. Strain distribution in the specimen gage section under four inelastic tension-compression loadings.

Biaxiality Ratio: $\lambda = \Delta\epsilon/\Delta\gamma = 1.5$
 Phase Angle: $\phi = 0$

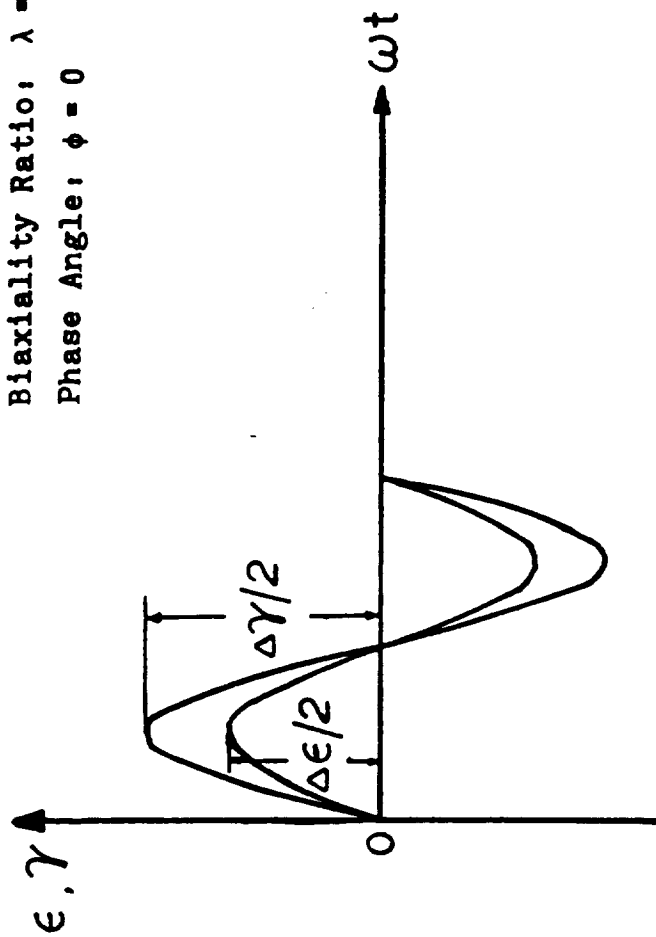


Figure 21. Strain versus time for in-phase biaxial straining

Specimen No. 20 & 21
 Temperature : 1200°F (649°C)
 Biaxiality Ratio: $\lambda = \Delta\epsilon/\Delta\gamma = 1.5$
 Phase Angle: $\phi = 90^\circ$

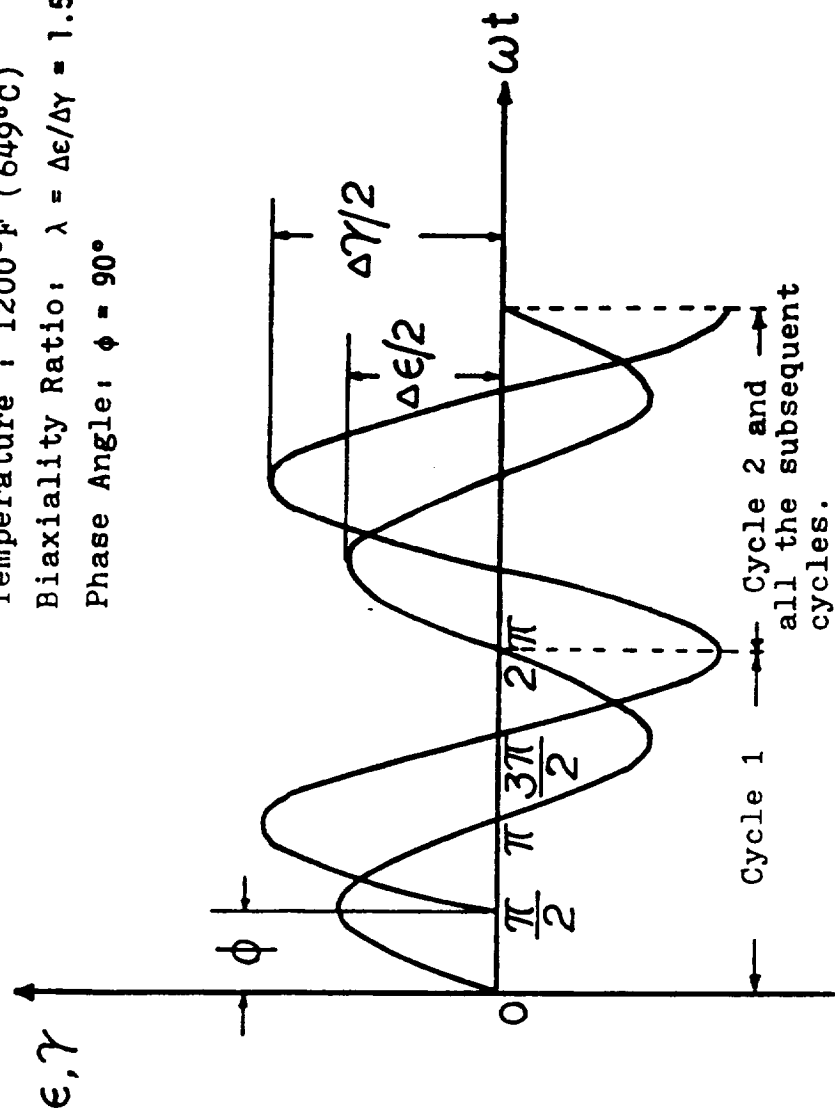


Figure 22. Strain versus time for out-of-phase biaxial straining

Specimen No. 25 & 27
 Temperature: 1200°F (649°C)
 Biaxiality Ratio: $\lambda = \Delta\epsilon/\Delta\gamma = 1.5$

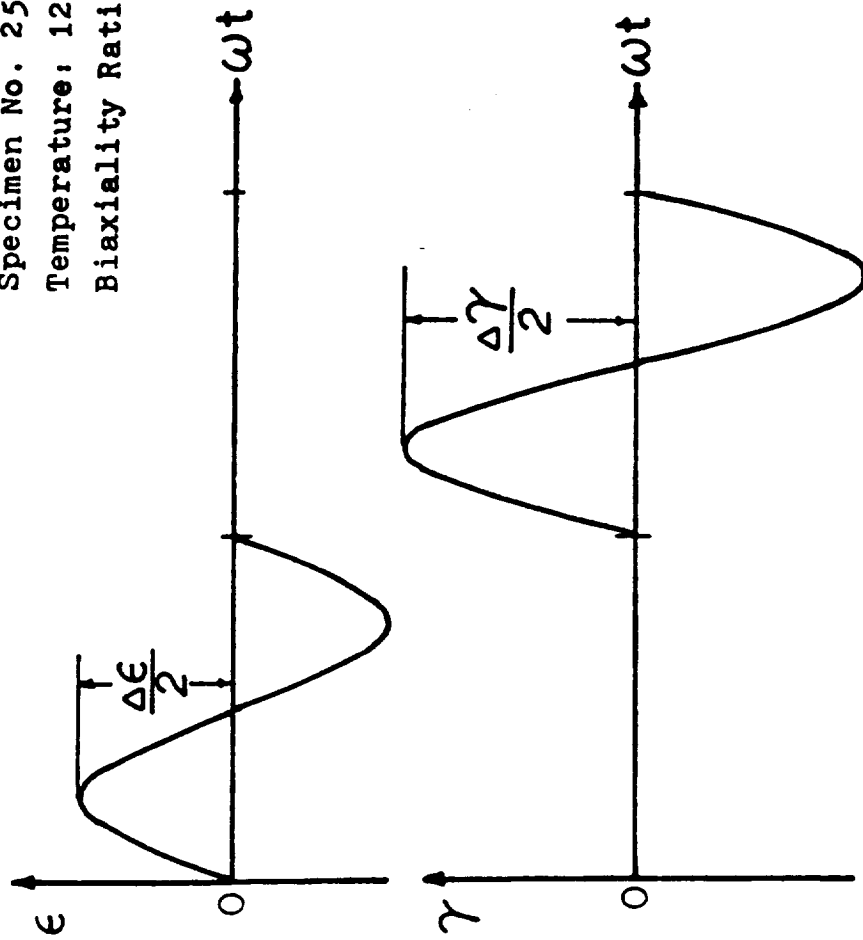


Figure 23. Strain versus time for biaxial straining which produces tensile mean stress during the torsion cycle

Specimen No. 28 & 29
 Temperature: 1200°F (649°C)
 Biaxiality Ratio: $\lambda = \Delta\epsilon/\Delta\gamma = 1.5$

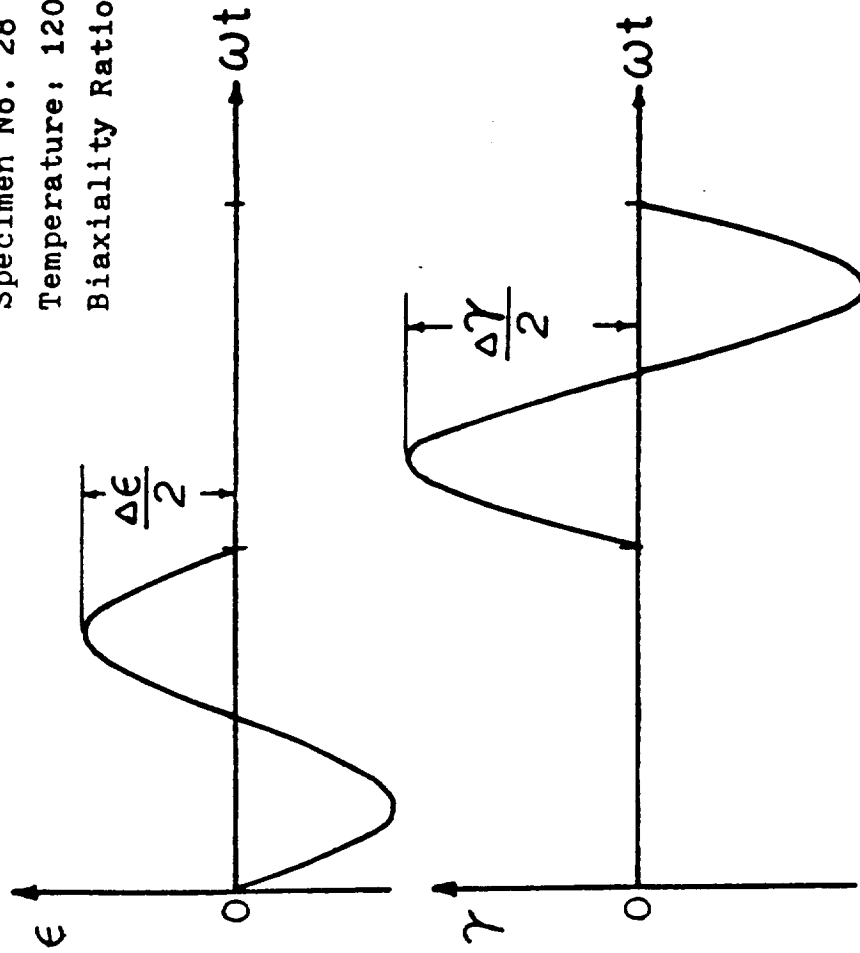


Figure 24. Strain versus time for biaxial straining which produces compressive mean stress during the torsion cycle.

Specimen No. 30, 31, 32 and 33
 Temperature: 1200°F (649°C)
 Biaxiality Ratio: $\lambda = \Delta\epsilon/\Delta\gamma = 1.5$

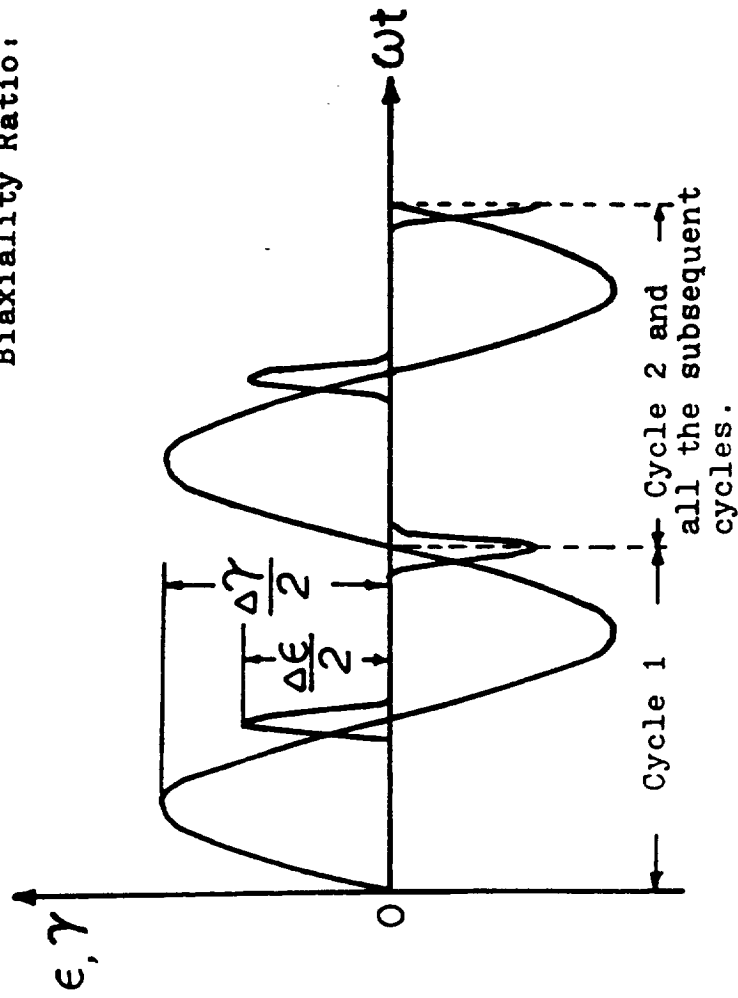


Figure 25. Strain versus time for biaxial straining by applying intermittent axial half cycles with a period of one tenth or one fifth that of the applied torsion but of the same frequency.

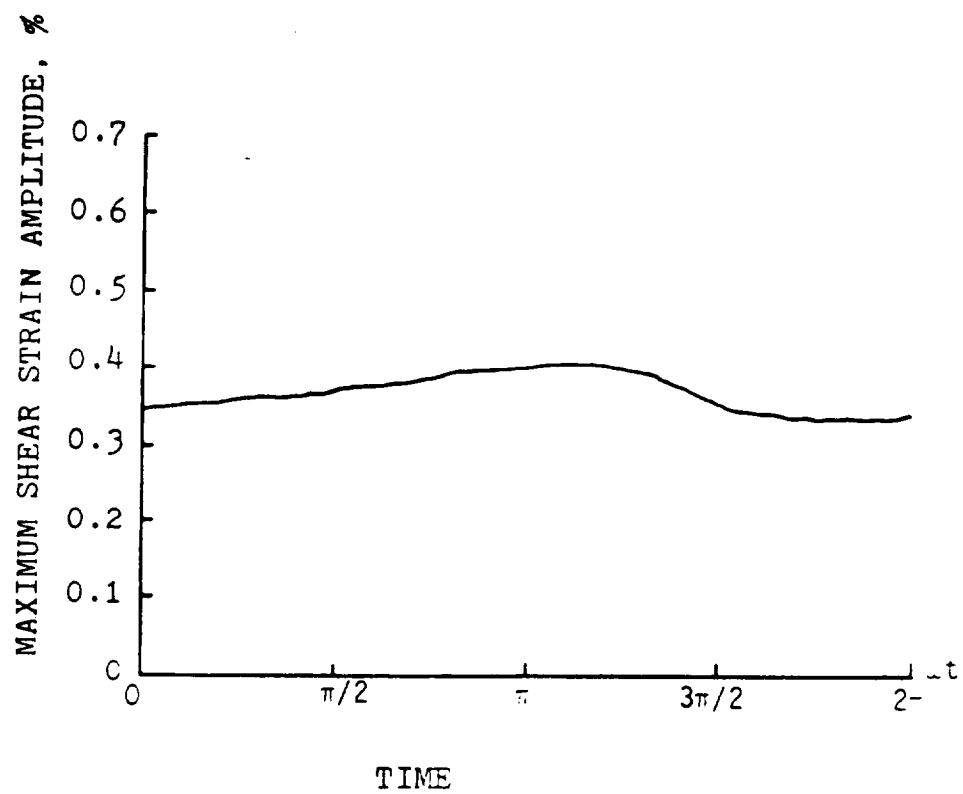


Figure 26. Maximum shear strain amplitude versus time for 90° out-of-phase non-proportional loading.

λ	ϕ	RT	(649°C) 1200°F
0		●	○
1.5	0	■	□
4.0	0	●	
∞		▲	△

◇ : $\lambda = 1.5, \phi = 90^\circ$ @ 1200°F (649°C)
 ⊗ : Specimen No. 25, 27
 ⊠ : Specimen No. 28, 29
 ⊙ : Specimen No. 30, 31
 ⊞ : Specimen No. 32, 33

@ 1200°F (649°C)

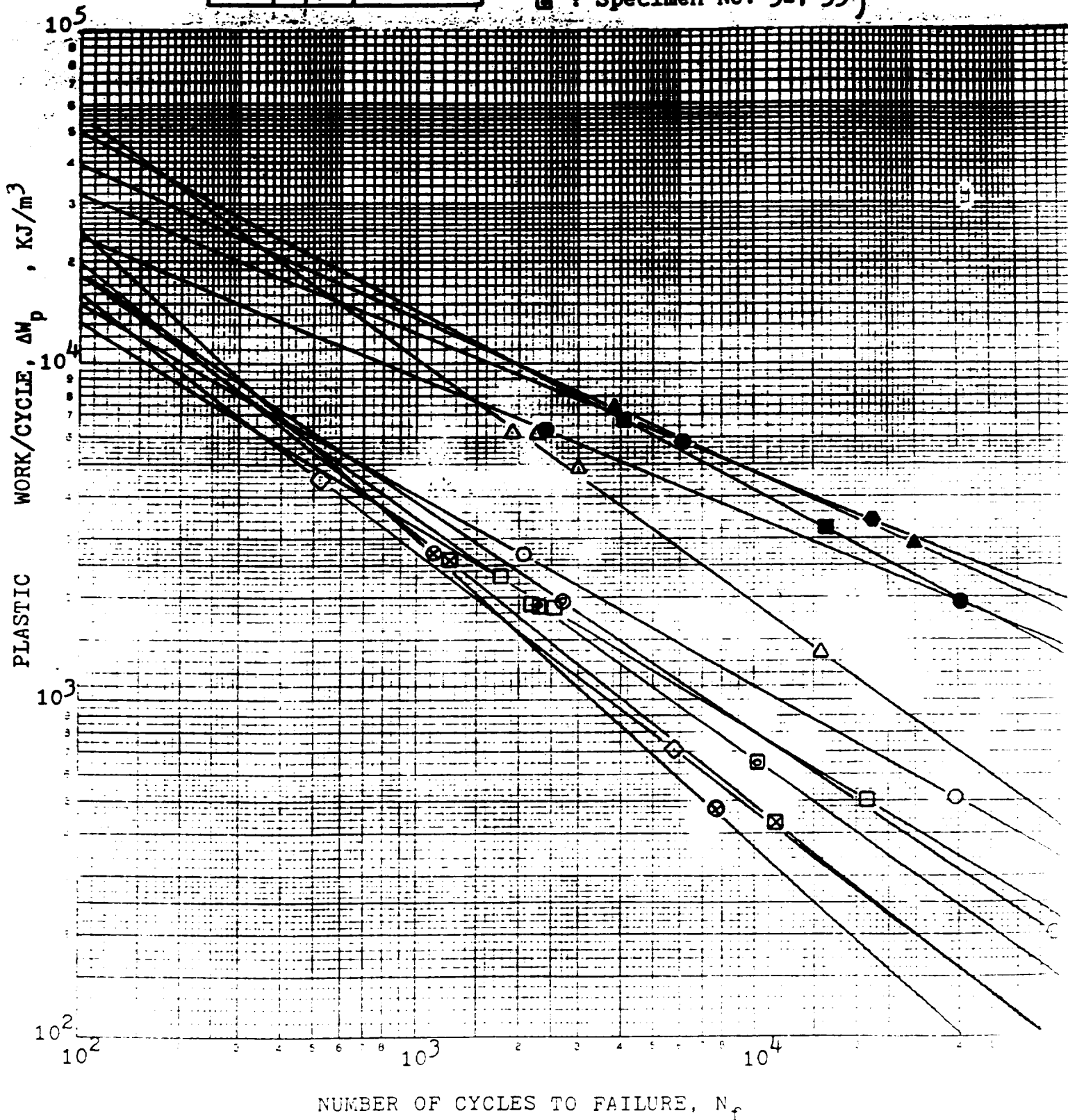


Figure 27. Plastic work per cycle versus cycles to failure

λ	ϕ	RT	(649°C) 1200°F
0		●	○
1.5	0	■	□
4.0	0	●	
∞		▲	△

◇ : $\lambda = 1.5, \phi = 90^\circ$ @ 1200°F (649°C)
 ⊗ : Specimen No. 25, 27
 ⊠ : Specimen No. 28, 29
 ⊙ : Specimen No. 30, 31
 ⊡ : Specimen No. 32, 33

@ 1200°F
(649°C)

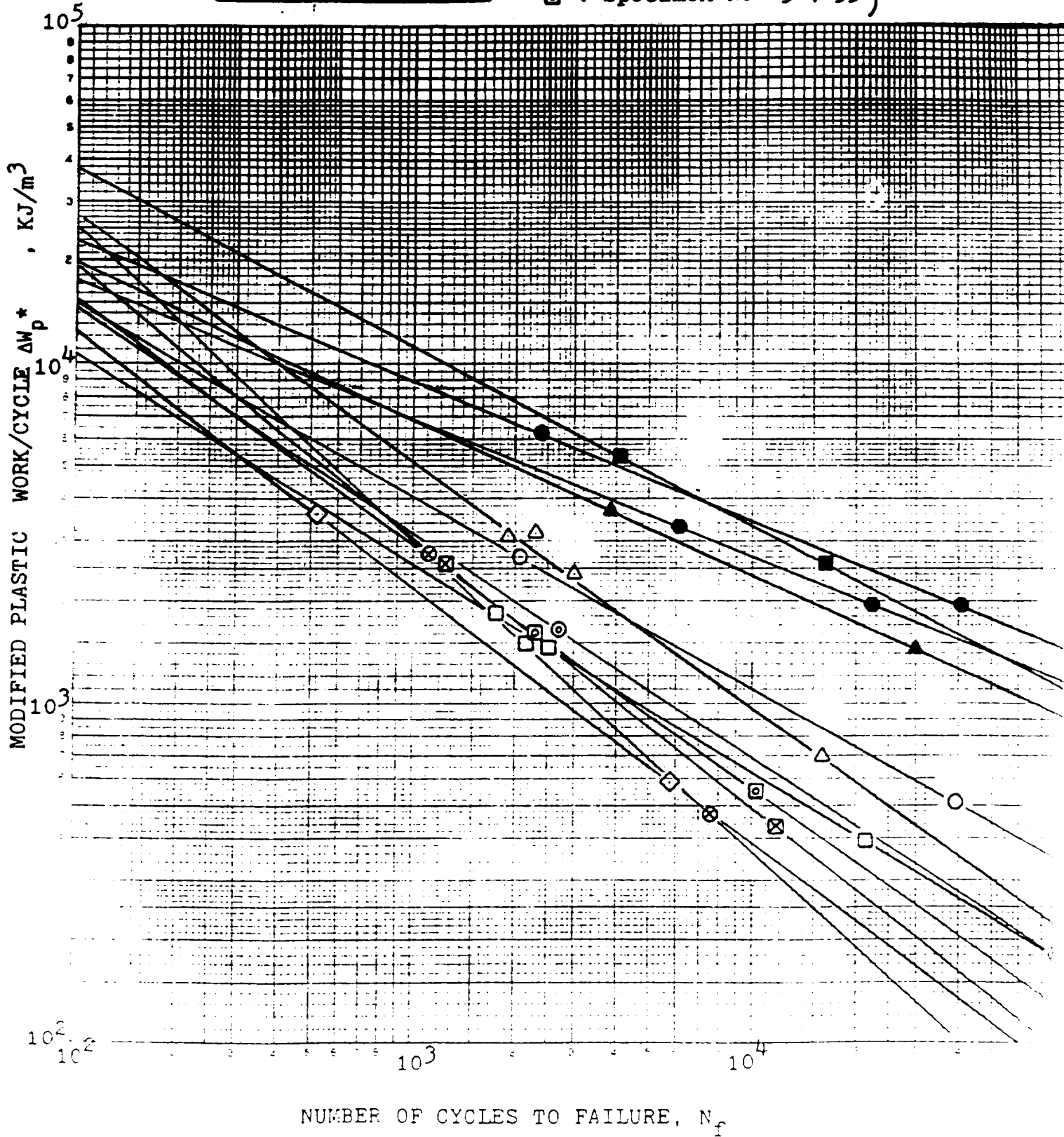


Figure 28. Modified plastic work per cycle versus cycles to failure

λ	ϕ	RT	(649°C) 1200°F
0		●	○
1.5	0	■	□
4.0	0	●	
∞		▲	△

◇ : $\lambda = 1.5, \phi = 90^\circ @ 1200^\circ\text{F} (649^\circ\text{C})$
 ⊗ : Specimen No. 25, 27
 ⊠ : Specimen No. 28, 29
 ⊙ : Specimen No. 30, 31
 ⊞ : Specimen No. 32, 33

} @ 1200°F
(649°C)

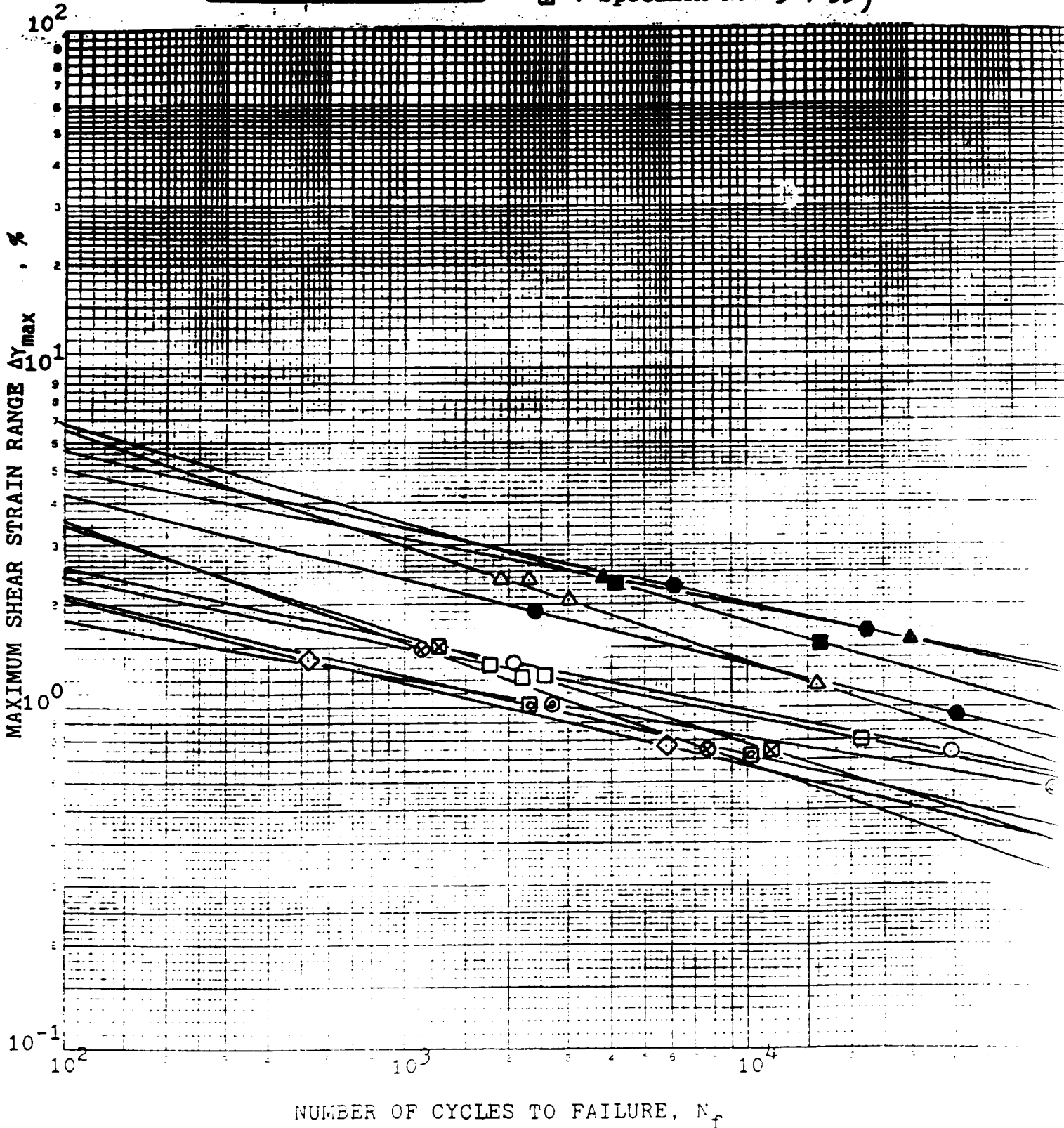


Figure 29. Maximum shear strain range versus cycles to failure

λ	ϕ	RT	(649°C) 1200°F
0		●	○
1.5	0	■	□
4.0	0	●	
∞		▲	△

◇ : $\lambda = 1.5, \phi = 90^\circ$ @ 1200°F (649°C)
 ⊗ : Specimen No. 25, 27
 ⊠ : Specimen No. 28, 29
 ⊙ : Specimen No. 30, 31
 ⊞ : Specimen No. 32, 33

} @ 1200°F (649°C)

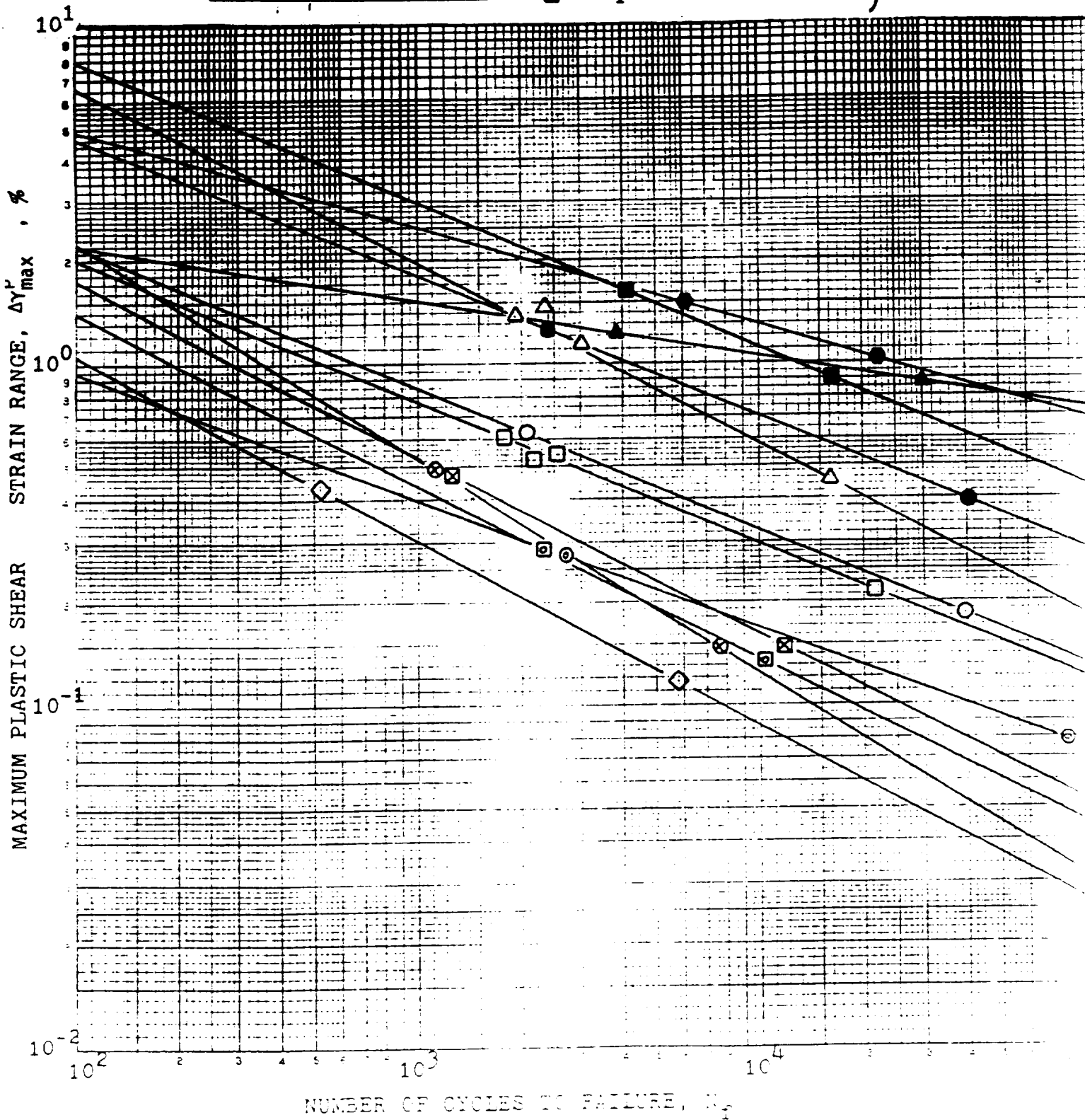


Figure 30. Maximum plastic shear strain range versus cycles to fail

λ	ϕ	RT	(649°C) 1200°F
0		●	○
1.5	0	■	□
4.0	0	●	
∞		▲	△

◇ : $\lambda = 1.5, \phi = 90^\circ$ @ 1200°F (649°C)
 ⊗ : Specimen No. 25, 27
 ⊠ : Specimen No. 28, 29
 ⊙ : Specimen No. 30, 31
 ⊞ : Specimen No. 32, 33

} @ 1200°F (649°C)

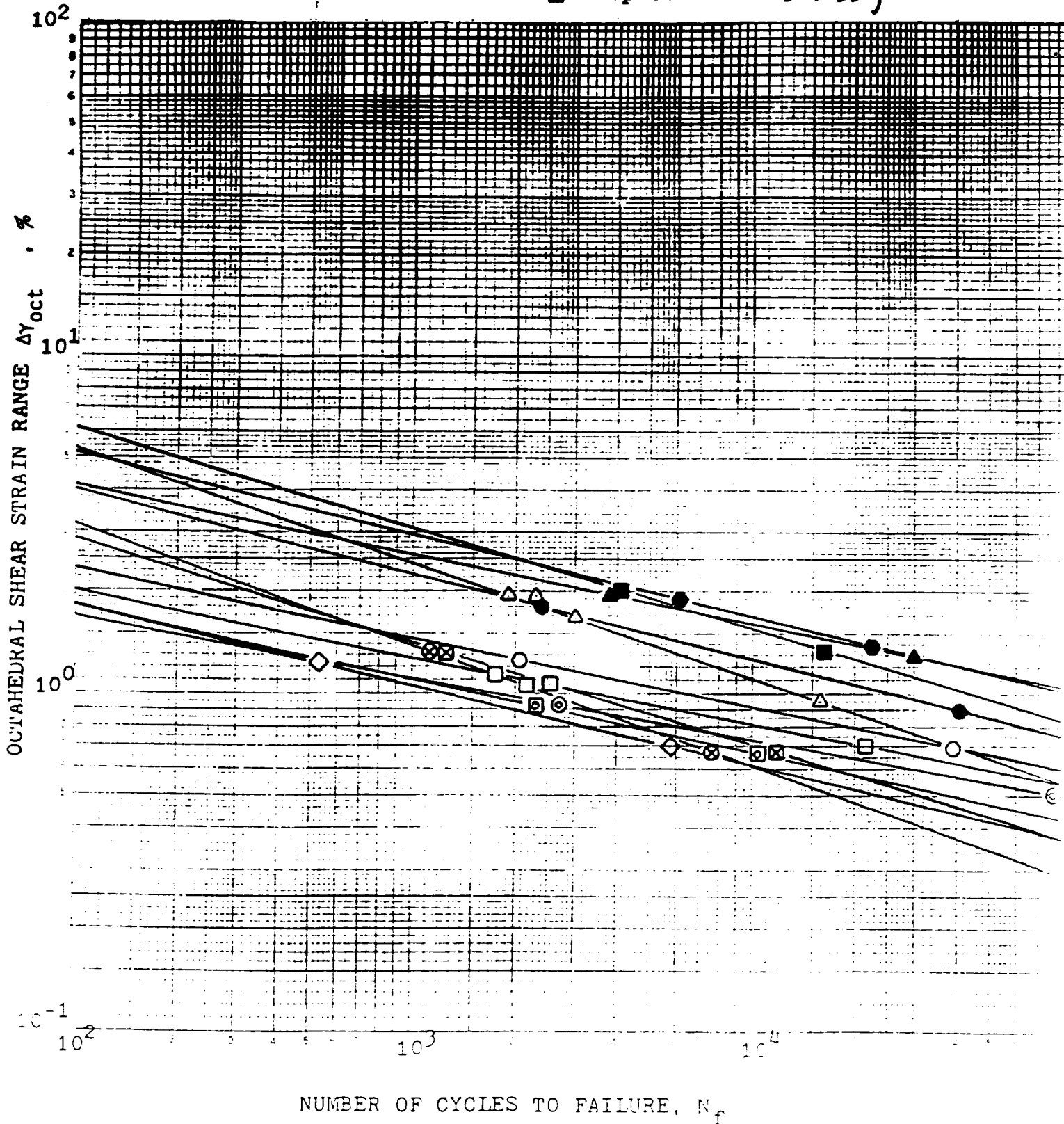


Figure 31. Octahedral shear strain range versus cycles to failure

λ	ϕ	RT	(649°C) 1200°F
0		●	○
1.5	0	■	□
4.0	0	●	
∞		▲	△

◇ : $\lambda = 1.5, \phi = 90^\circ$ @ 1200°F (649°C)
 ⊗ : Specimen No. 25, 27
 ⊠ : Specimen No. 28, 29
 ⊙ : Specimen No. 30, 31
 ⊞ : Specimen No. 32, 33

} @ 1200°F (649°C)

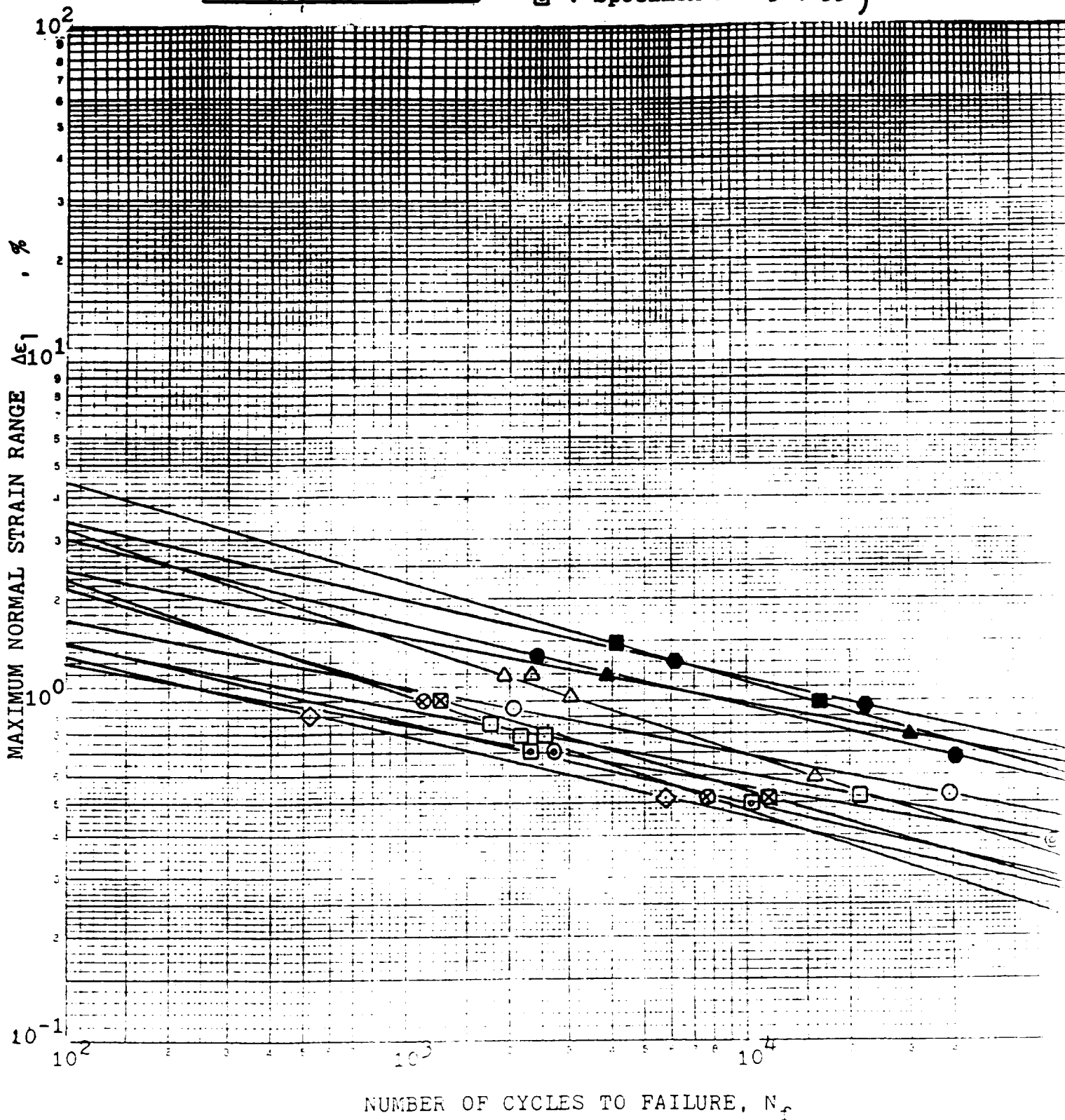


Figure 32. Maximum normal strain range versus cycles to failure

λ	ϕ	RT	(649°C) 1200°F
0		●	○
1.5	0	■	□
4.0	0	●	
∞		▲	△

◇ : $\lambda = 1.5, \phi = 90^\circ$ @ 1200°F (649°C)

⊗ : Specimen No. 25, 27

⊠ : Specimen No. 28, 29

⊙ : Specimen No. 30, 31

⊞ : Specimen No. 32, 33

@ 1200°F
(649°C)

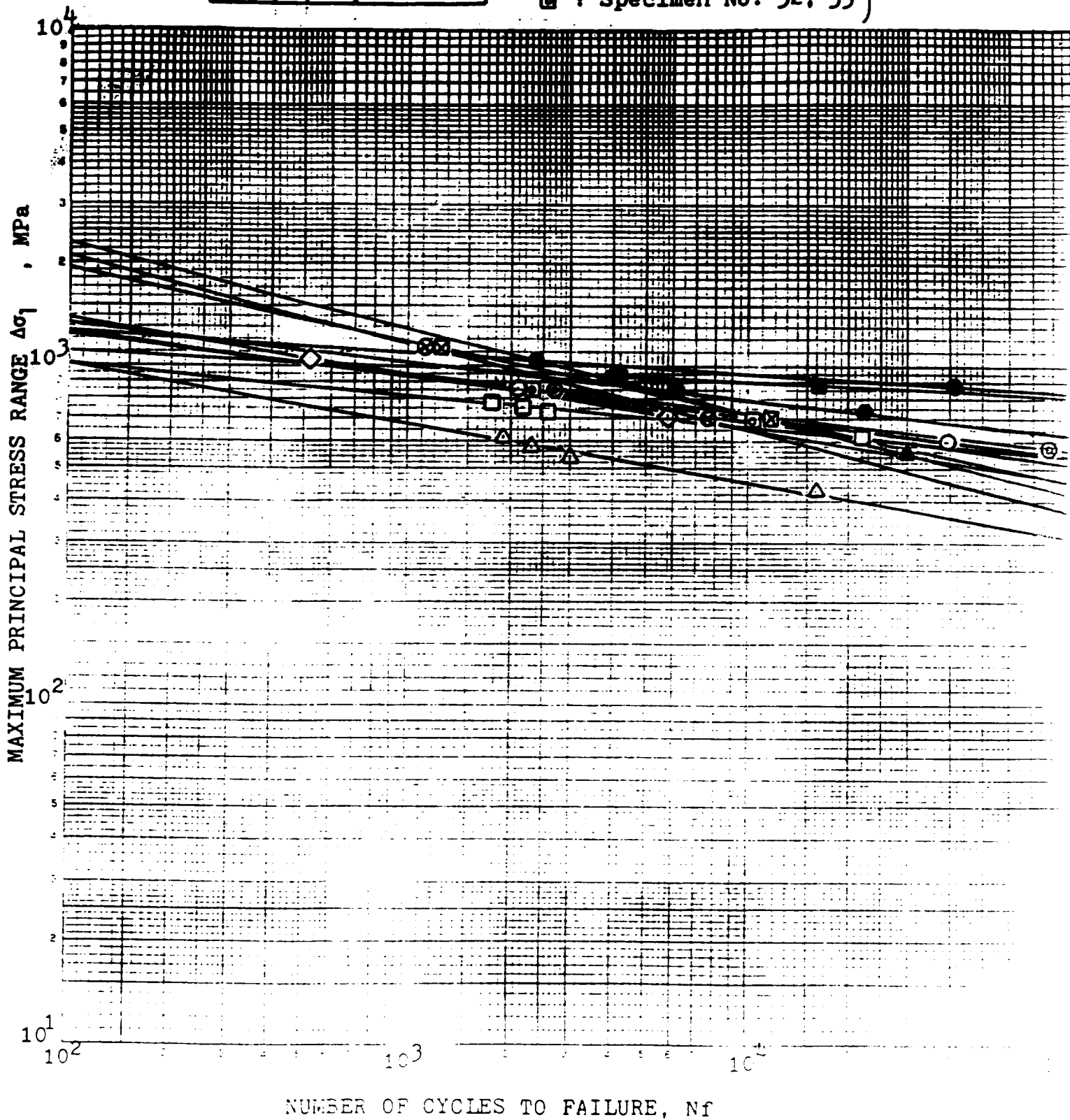


Figure 33. Maximum principal stress range versus cycles to failure

λ	ϕ	RT	(649°C) 1200°F
0		●	○
1.5	0	■	□
4.0	0	●	
∞		▲	△

◇ : $\lambda = 1.5, \phi = 90^\circ$ @ 1200°F (649°C)
 ⊗ : Specimen No. 25, 27
 ⊠ : Specimen No. 28, 29
 ⊙ : Specimen No. 30, 31
 ⊞ : Specimen No. 32, 33

} @ 1200°F (649°C)

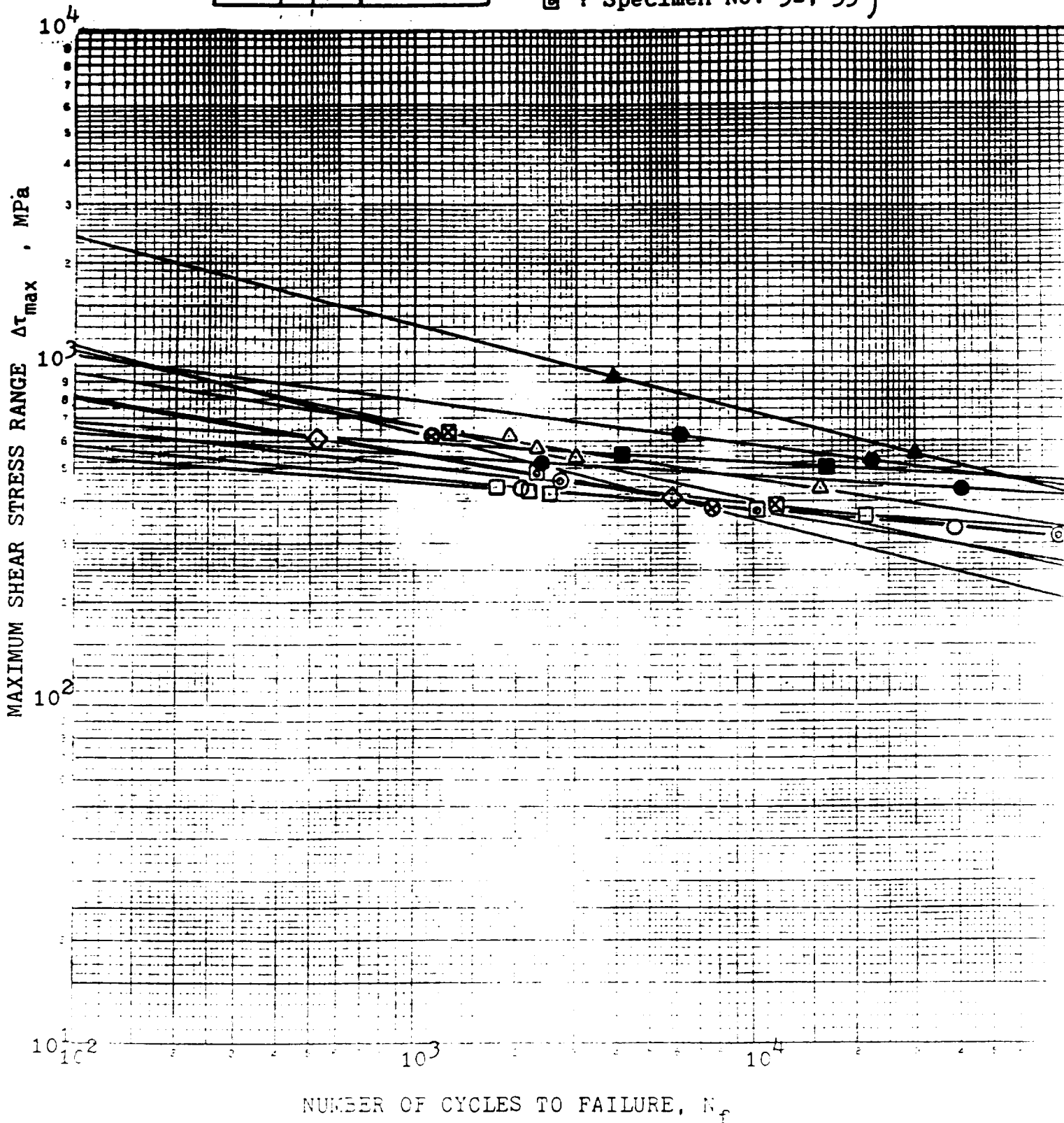


Figure 34. Maximum shear stress range versus cycles to failure

λ	ϕ	RT	(649°C) 1200°F
0		●	○
1.5	0	■	□
4.0	0	●	
∞		▲	△

◇ : $\lambda = 1.5, \phi = 90^\circ$ @ 1200°F (649°C)
 ⊗ : Specimen No. 25, 27
 ⊠ : Specimen No. 28, 29
 ⊙ : Specimen No. 30, 31
 ⊞ : Specimen No. 32, 33

@ 1200°F (649°C)

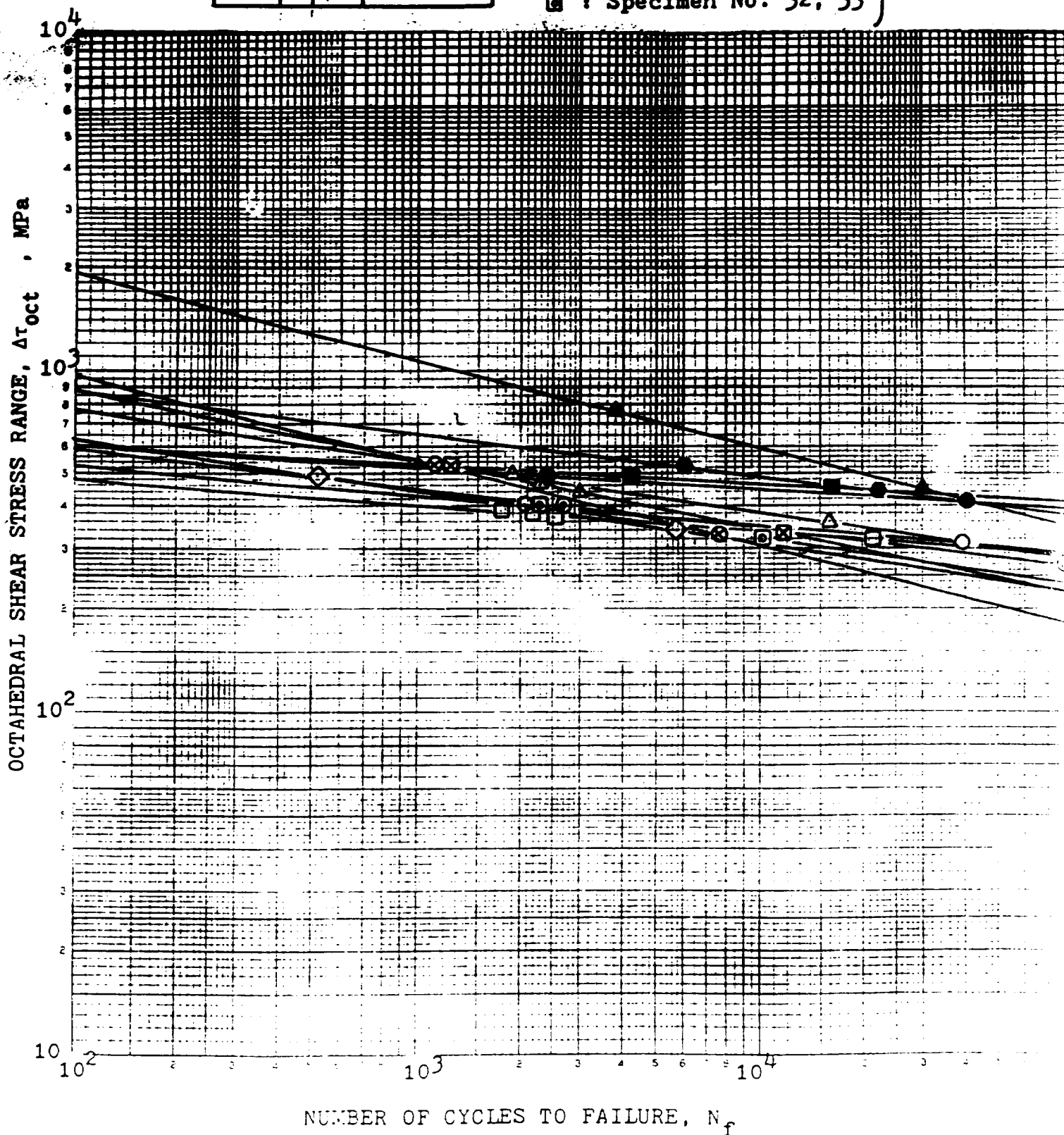


Figure 35. Octahedral shear stress range versus cycles to failure

λ	ϕ	RT	(649°C) 1200°F
0		●	○
1.5	0	■	□
4.0	0	●	
∞		▲	△

◇ : $\lambda = 1.5, \phi = 90^\circ$ @ 1200°F (649°C)
 ⊗ : Specimen No. 25, 27
 ⊠ : Specimen No. 28, 29
 ⊙ : Specimen No. 30, 31
 ⊞ : Specimen No. 32, 33

} @ 1200°F
(649°C)

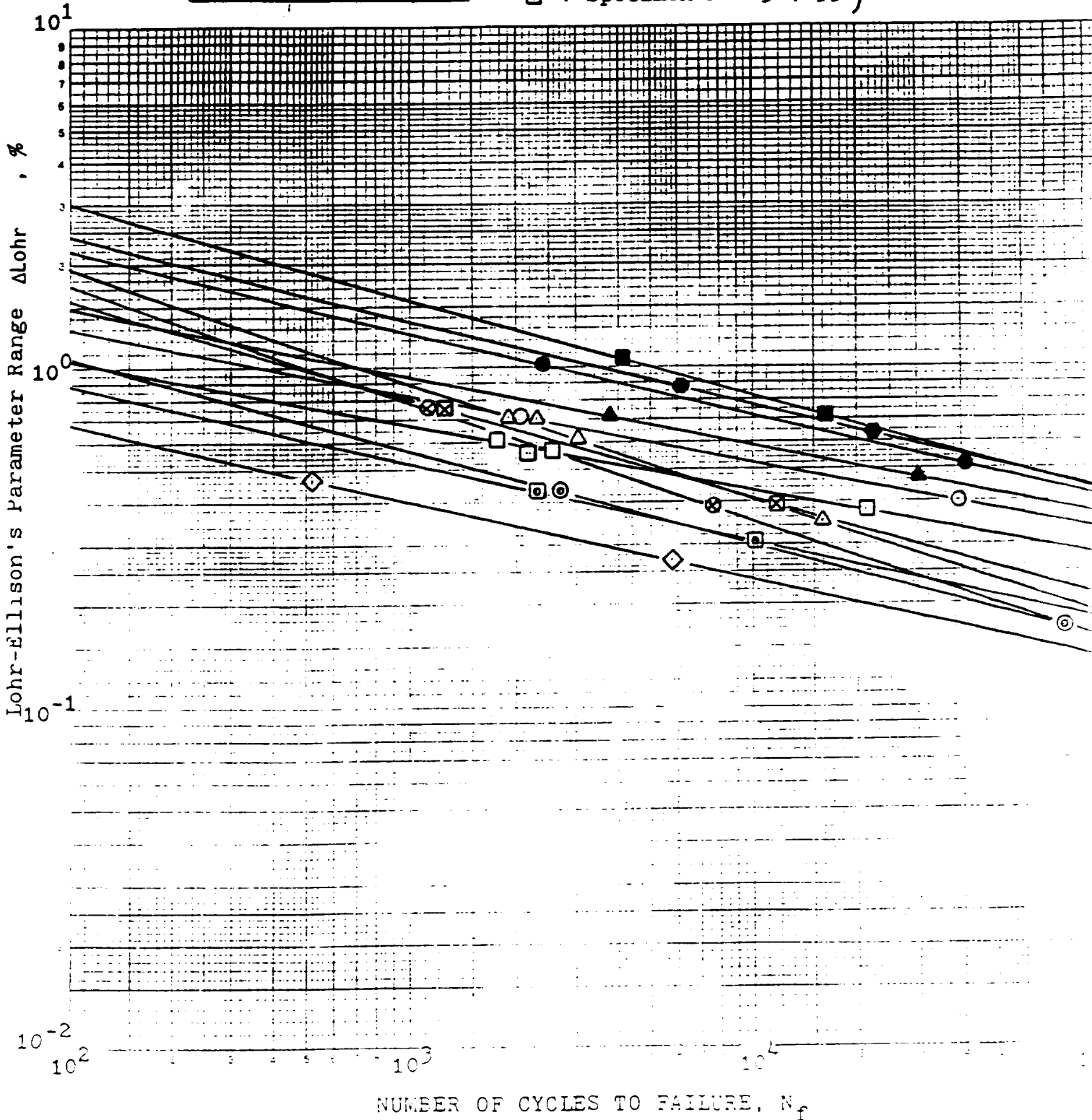
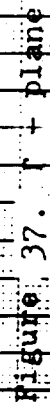
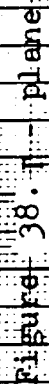


Figure 36. Lohr-Ellison's parameter range versus cycles to failure





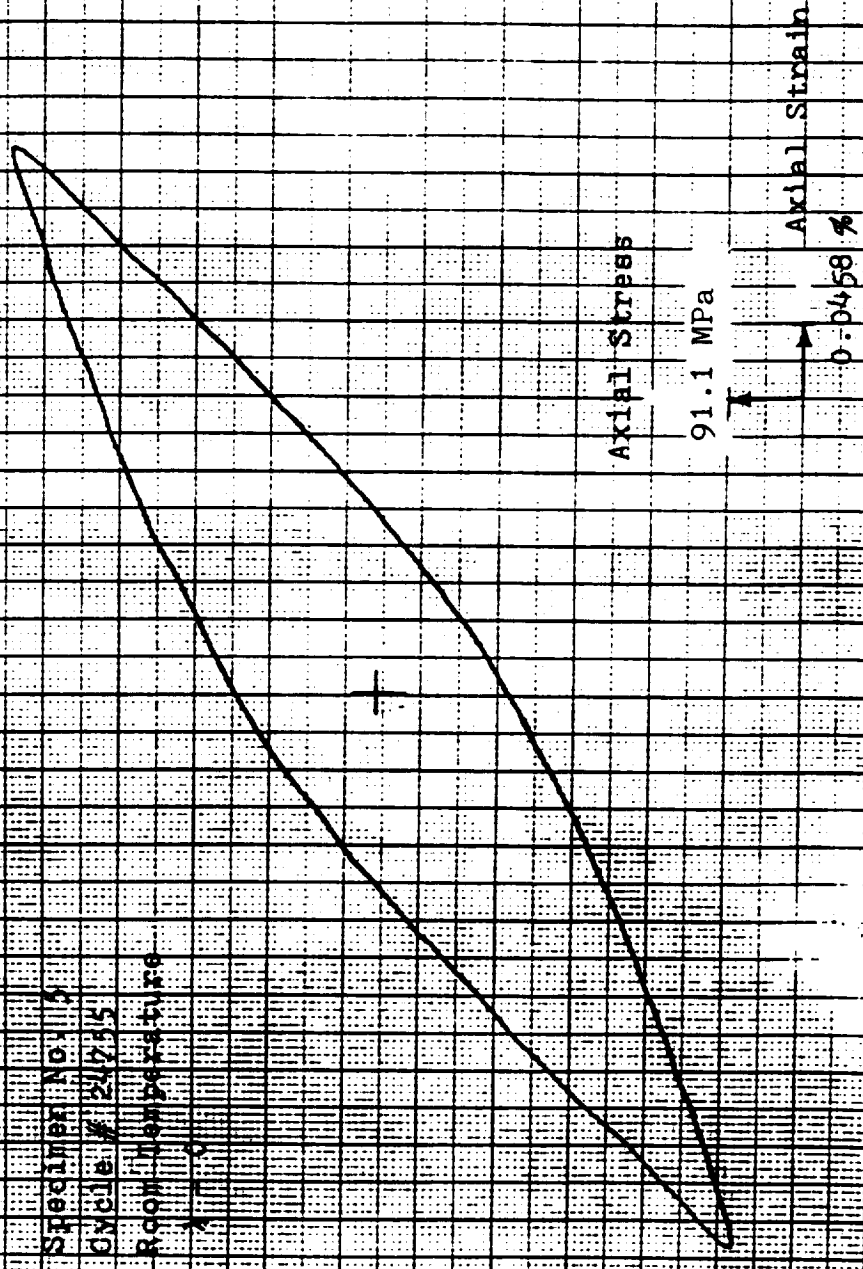


Figure 39. Axial Hysteresis Loop

Specimen No. 9
Cycle # 10,000
Room Temperature
 $\lambda = 1.5$
 $\phi = 0$

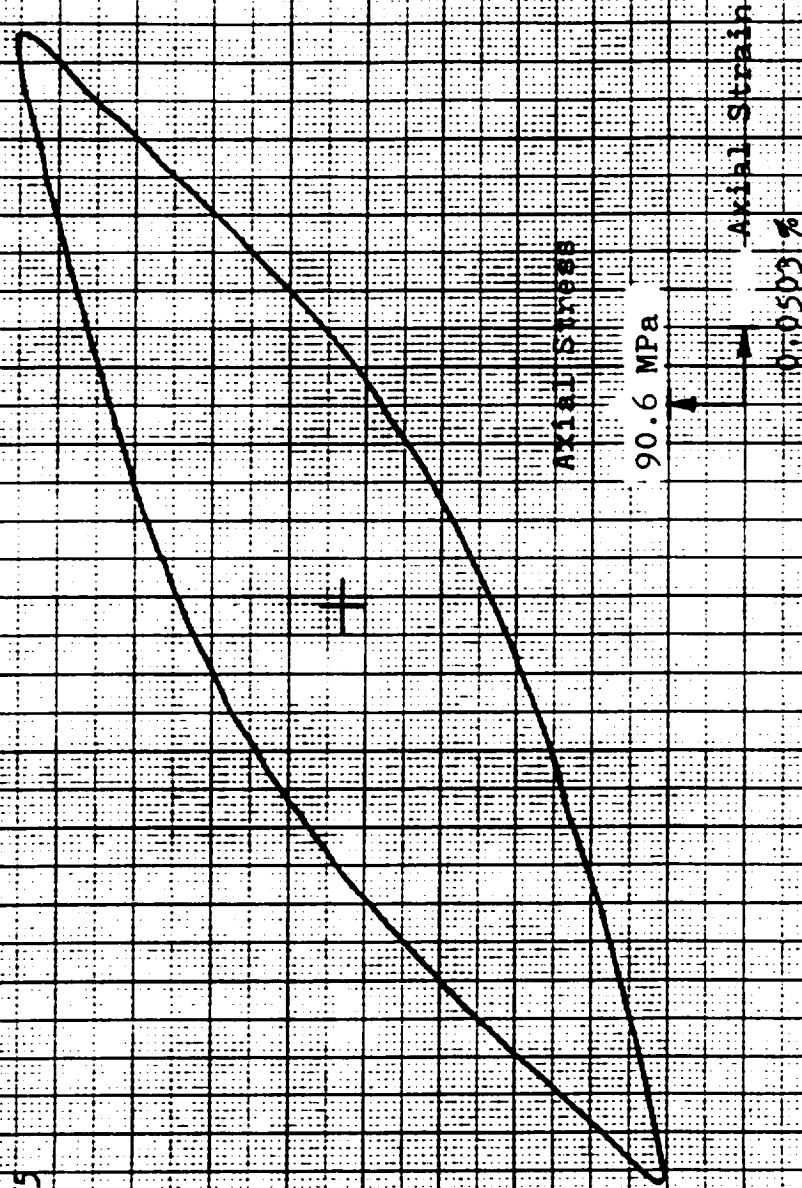


Figure 40. Axial Hysteresis Loop

Specimen No. 9
Cycle # 10,000
Room Temperature
 $\lambda = 1.5$
 $\nu = 0$

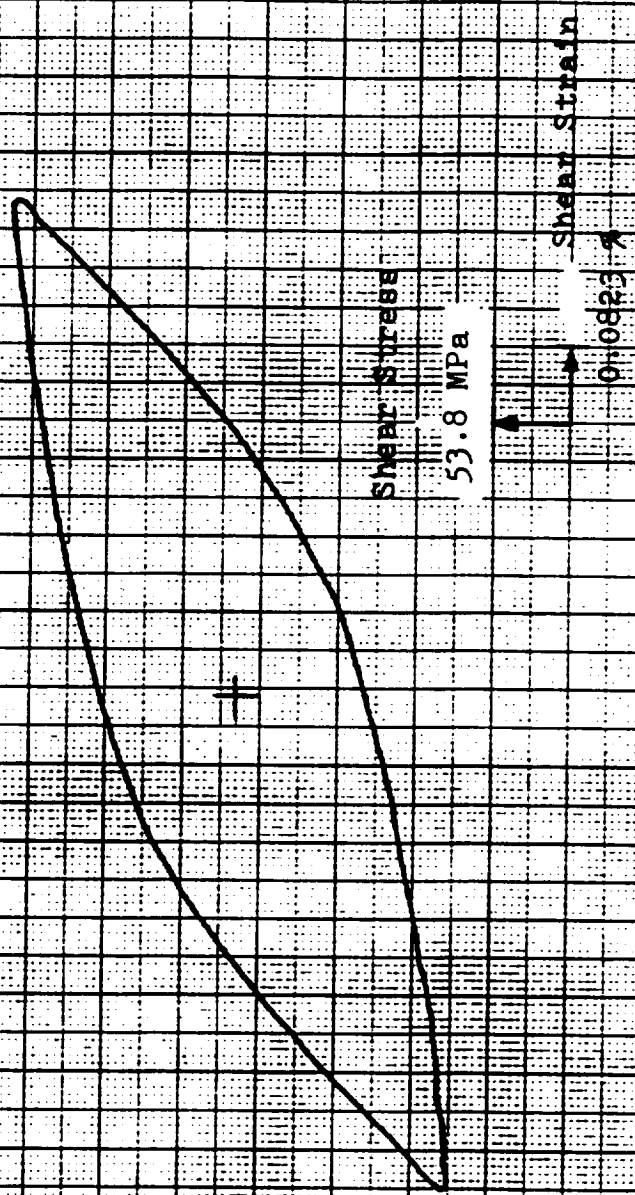


Figure 41. Torsion Hysteresis Loop

Specimen No. 14
Cycle # 10,000
Room Temperature
 $\lambda = 4.0$
 $\phi = 0$

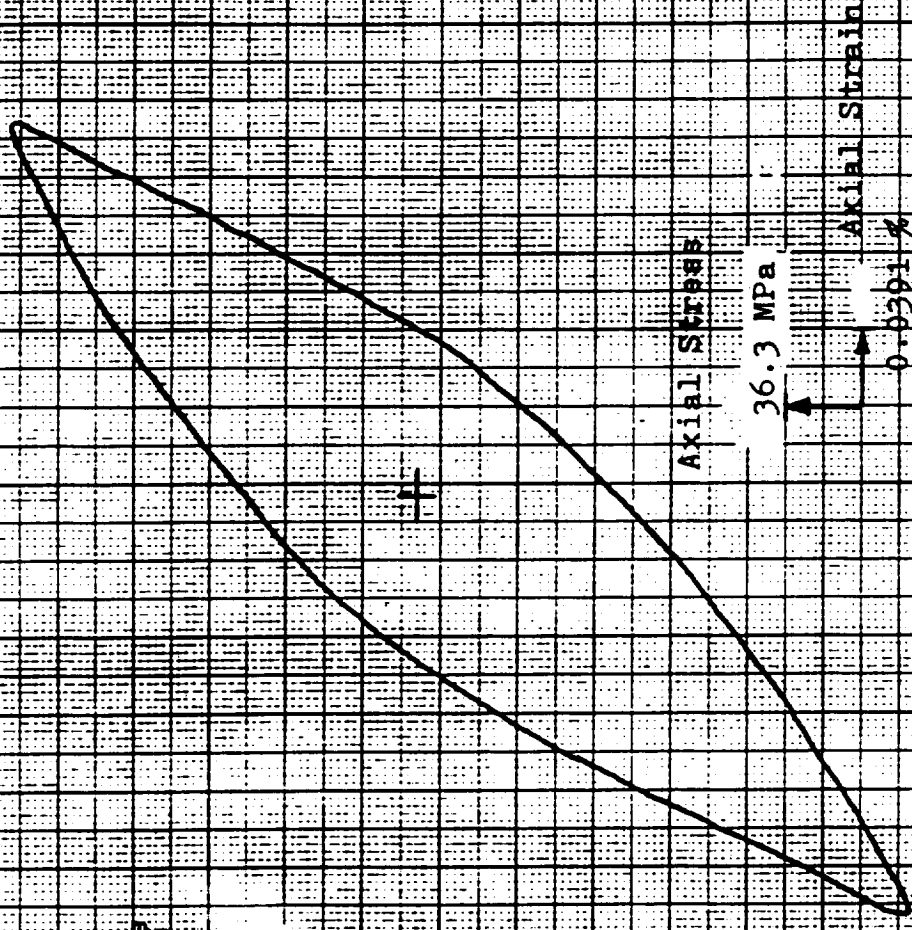
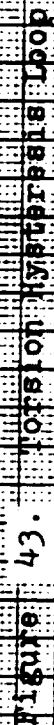


Figure 42. Axial Hysteresis Loop



Specimen No. 7
Cycle # 23,910
Room Temperature

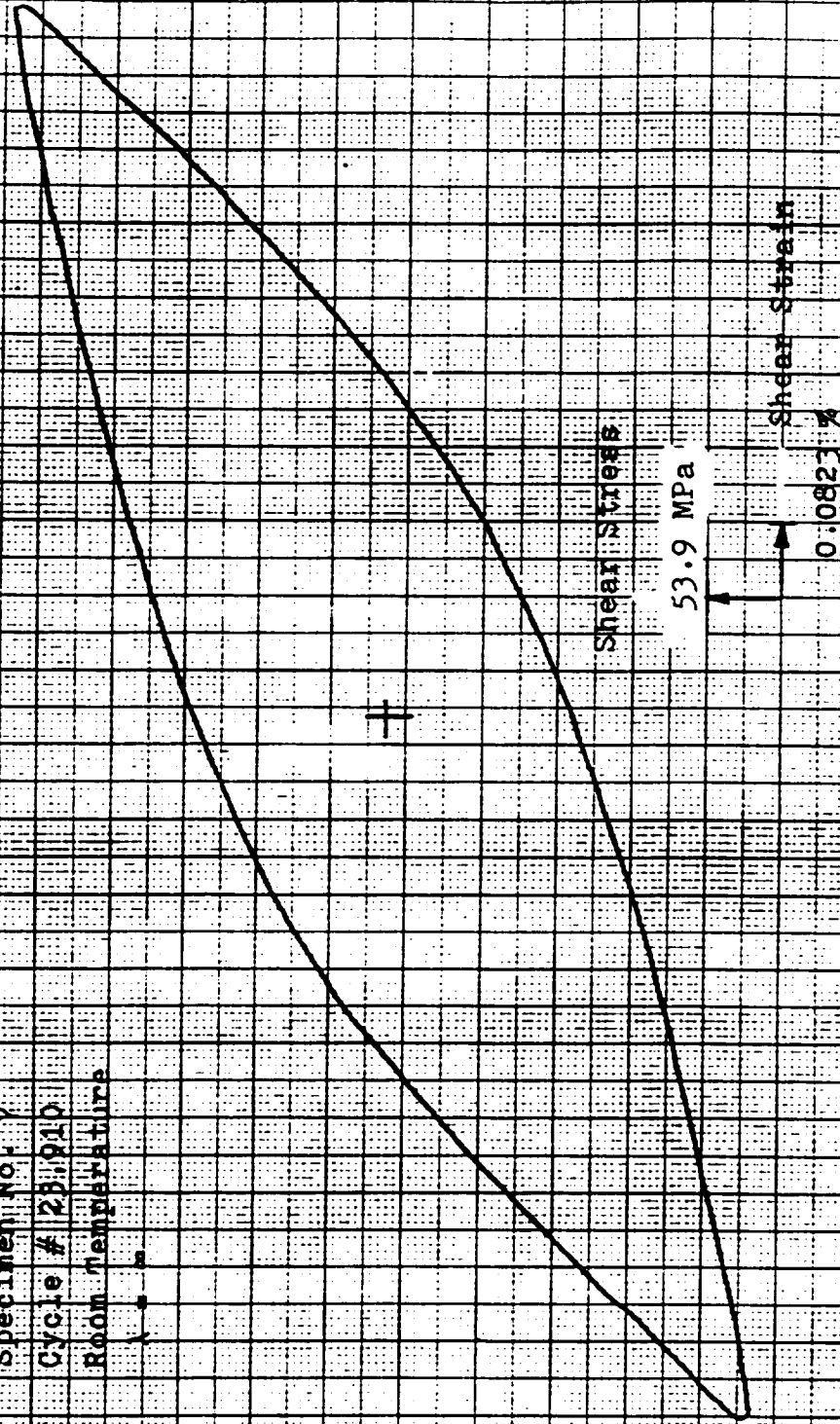
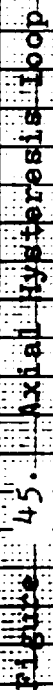


Figure 44. Torsion Hysteresis Loop



Specimen No. 34

Cycle # 1,000

Temperature: 1200°F (649°C)

$\lambda = 1.5$

$\phi = 0$

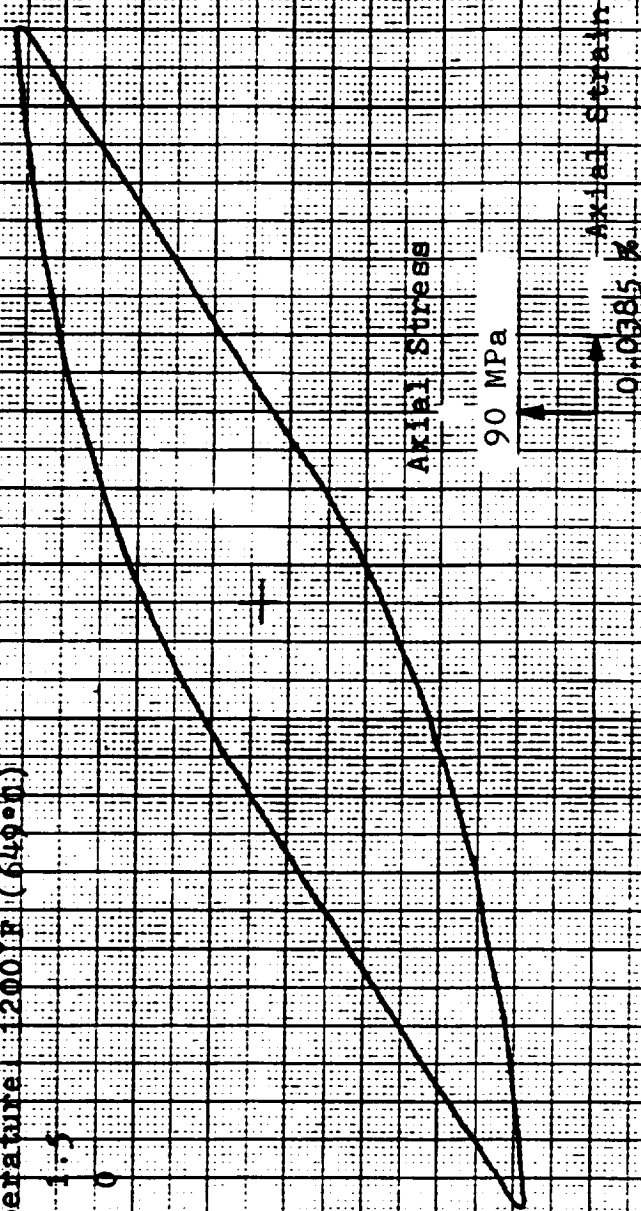


Figure 46. Axial Hysteresis Loop

Specimen No. 34

Cycle # 1,000

Temperature 200°F (649°K)

$\lambda = 1.5$

$\phi = 0$

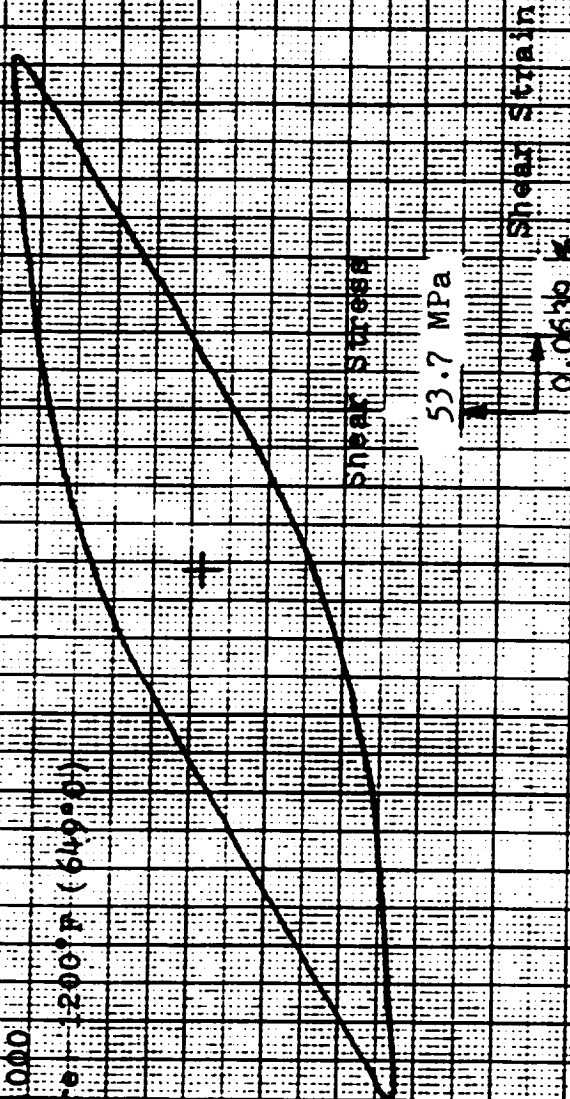


Figure 47. Torsion Hysteresis Loop

Specimen No. 19

Cycle # 1,500

Temperature: 1200°F (649°C)

$\lambda = \infty$

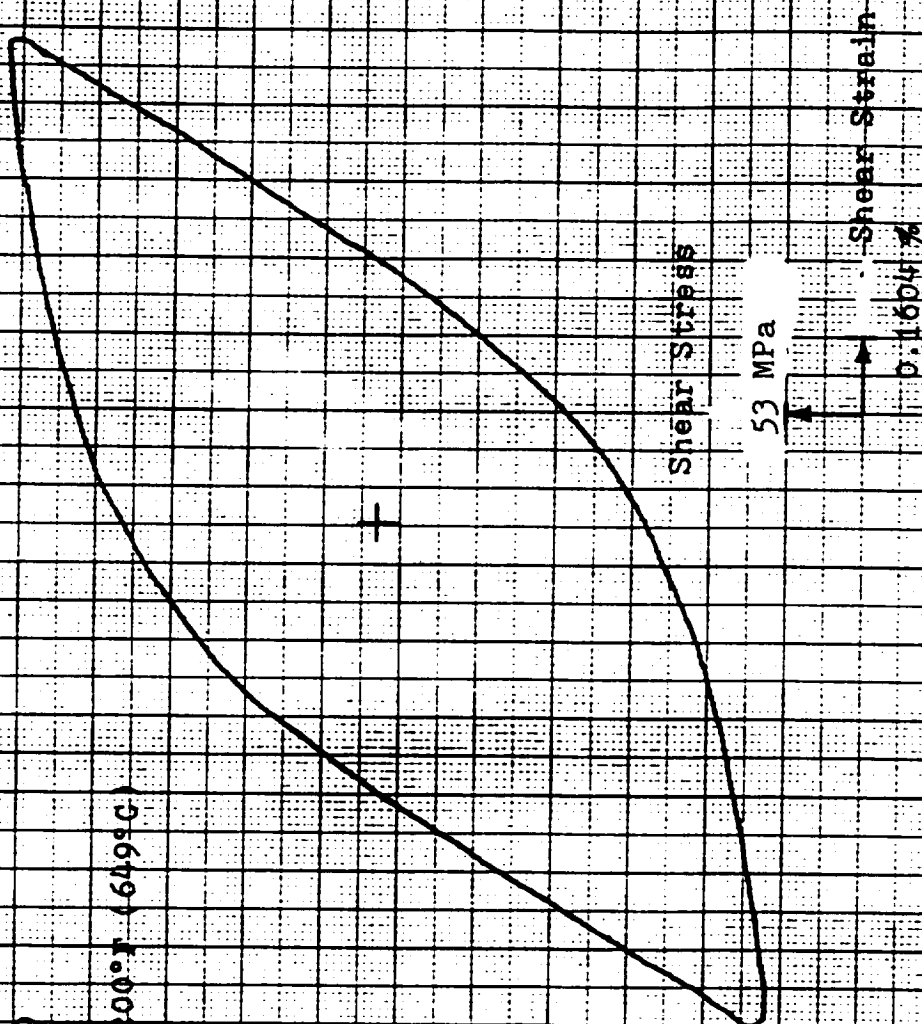


Figure 48. Torsion Hysteresis Loop

Specimen No. 36

Cycle # 1,000

Temperature: 1200 °F (649 °C)

Using Induction Heater

 $\lambda = 0$

Shear Stress

54.1 MPa

Shear Strain

0.1598 %

Figure 49. Torsion Hysteresis Loop

Specimen No. 20

Cycle # 2,120

Temperature: 1200°F (649°C)

$\lambda = 1.5$

$\theta = 90^\circ$

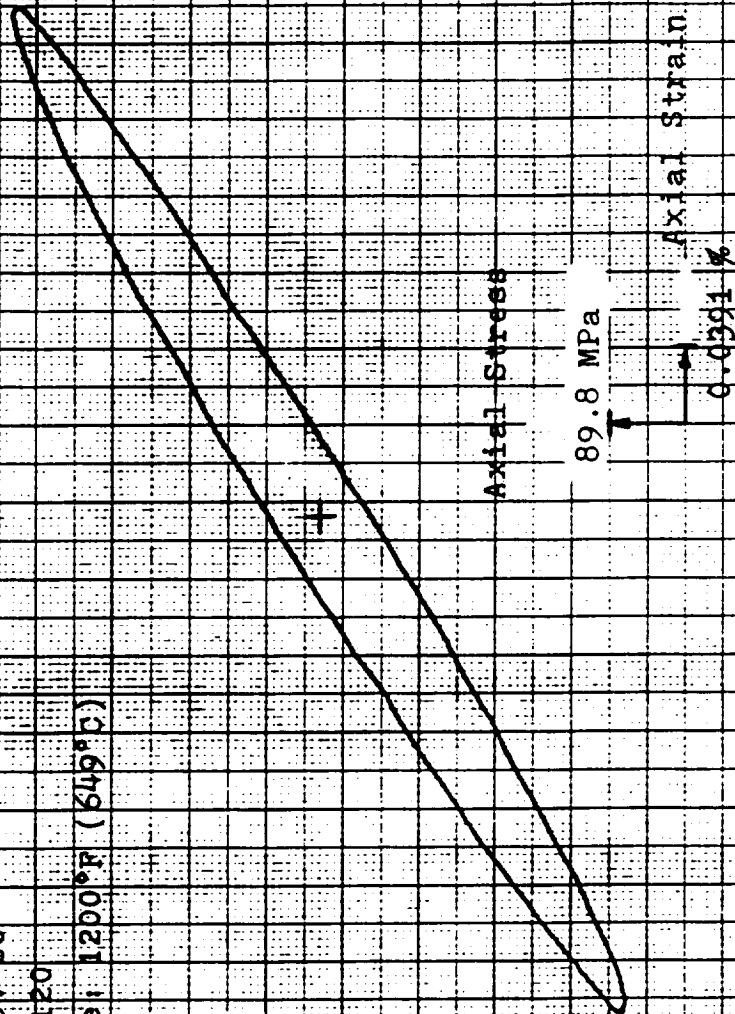
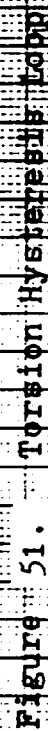


Figure 50. Axial Hysteresis Loop

90



Specimen No. 27

Cycle # 265

Temperature: 1200°F (649°C)

$\lambda = 1.5$

Non-proportional loading consisted of alternate torsion and torsion with a tensile mean stress during the torsion cycle.

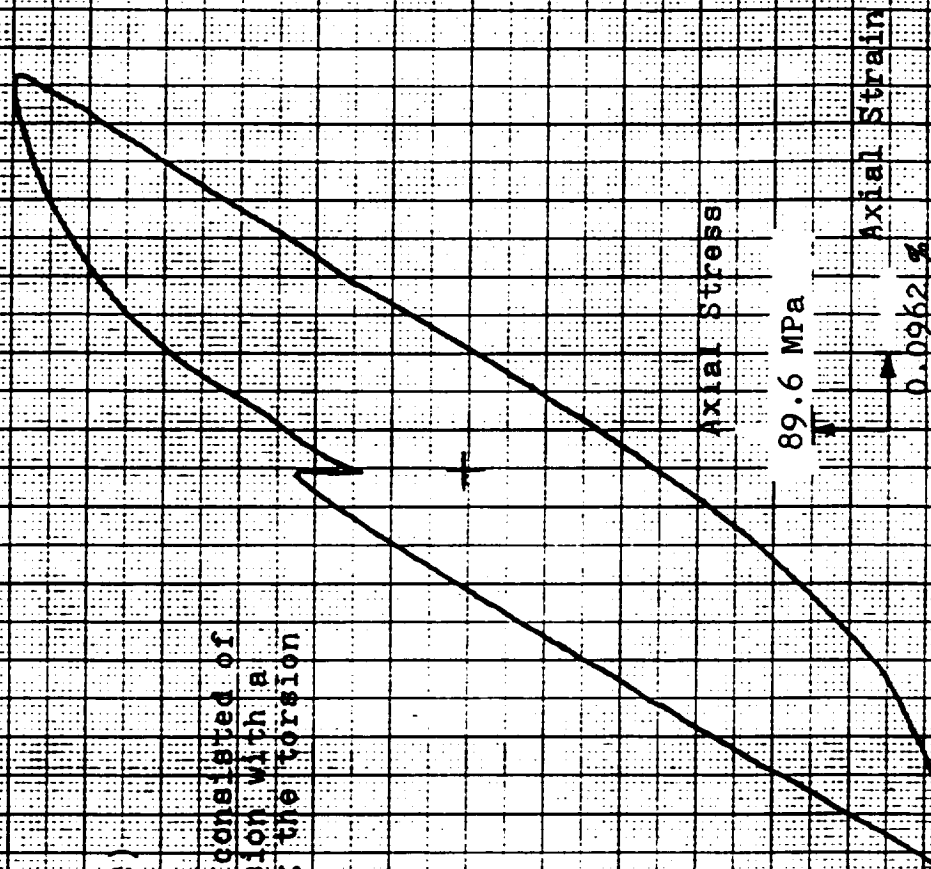


Figure 52. Axial Hysteresis Loop

Specimen No. 27

Cycle # 786

Temperature: 1200°F (649°C)

 $\lambda = 1.5$

Non-Proportional loading consisted of alternate tension and torsion with a tensile mean stress during the torsion cycle.

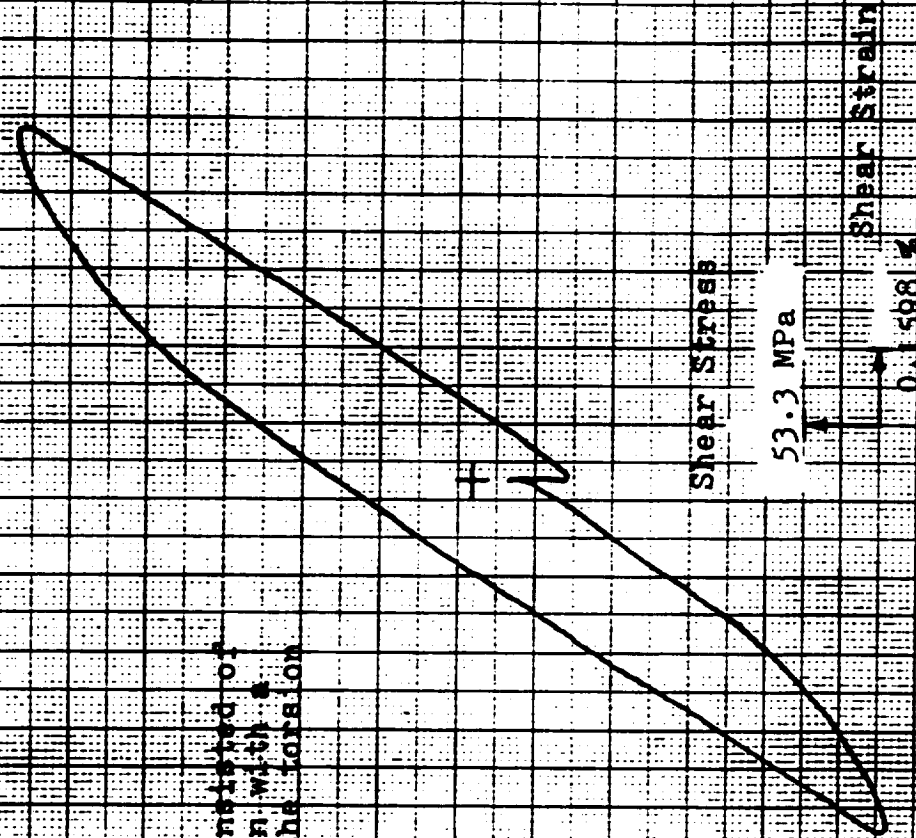


Figure 53. Torsion hysteresis loop

Specimen No. 28

Cycle # 699

Temperature: 1200°F (649°C)

$\lambda = 1.5$

Non-Proportional Loading: consisted of alternate tension and torsion with a compressive mean stress during the torsion cycle.

T

N

Axial Stress

89.8 MPa

Axial Strain

0.0962 %

Figure 54. Axial Hysteresis Loop

Specimen No. 28

Cycle # 700

Temperature: 1200°F (649°C)

$\lambda = 1.145$

Non-proportional loading, consisted of alternate tension and torsion with a compressive mean stress during the torsion cycle.

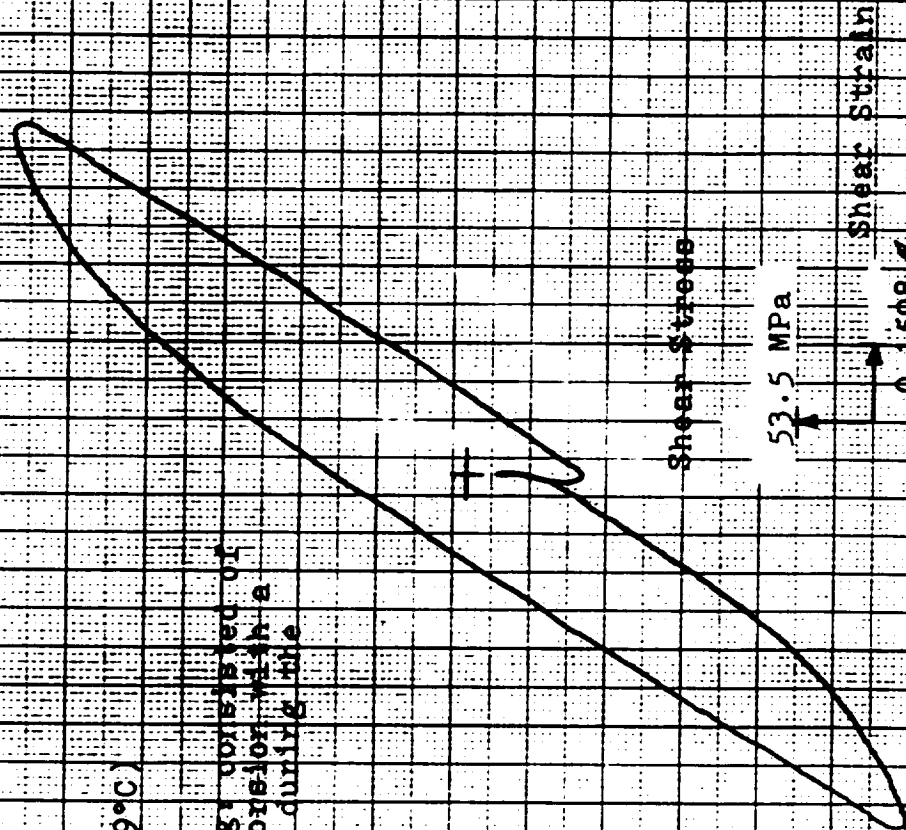


Figure 55. Torsion Hysteresis Loop

Specimen No. 30

Cycle # 1,700

Temperature: 1200°F (649°C)

$\lambda = 1.5$

Non-Proportional loading: applying
intermittent axial half cycles with
a period of one tenth that of the
applied torsion but of the same
frequency.

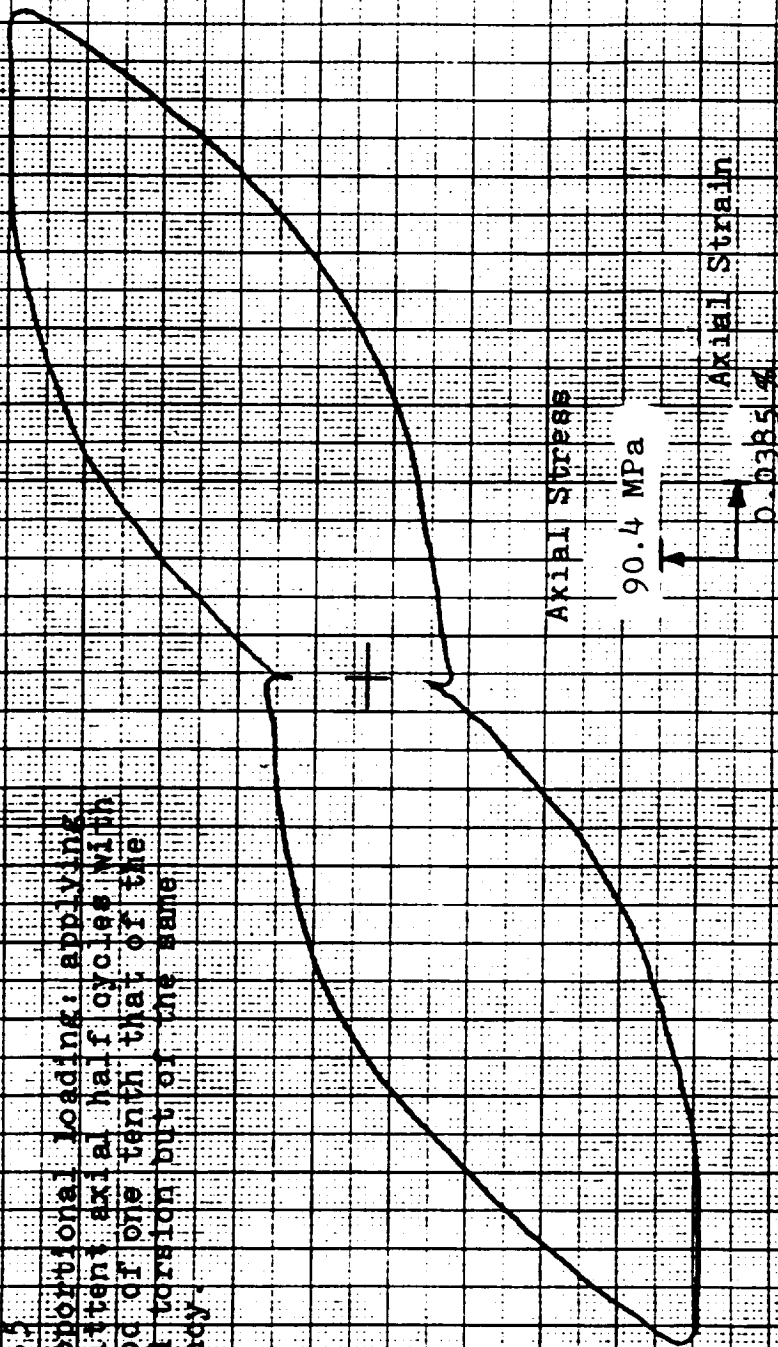


Figure 56. Axial Hysteresis Loop

Specimen No. 30

Cycle # 1,700

Temperature: 1200°F (649°C)

 $\lambda = 1.5$

Non-Proportional Loading: applying intermittent axial half cycles with a period of one tenth that of the applied torsion but the same frequency.

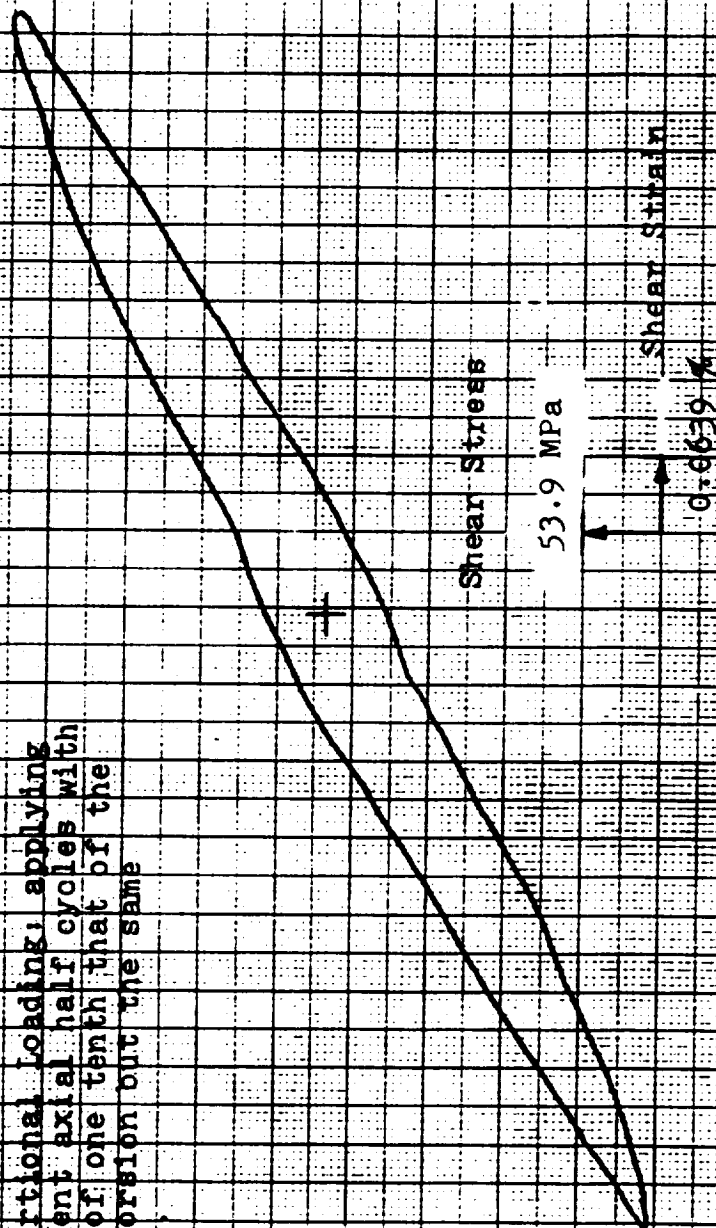


Figure 57. Torsion Hysteresis Loop

Specimen No. 12

Cycle # 1, 140

Temperature: 1200°F (649°C)

 $\lambda = 1.5$

Non-Proportional Loading: applying
intermittent axial half cycles with
a period of one fifth that of the
applied tension but of the same
frequency.

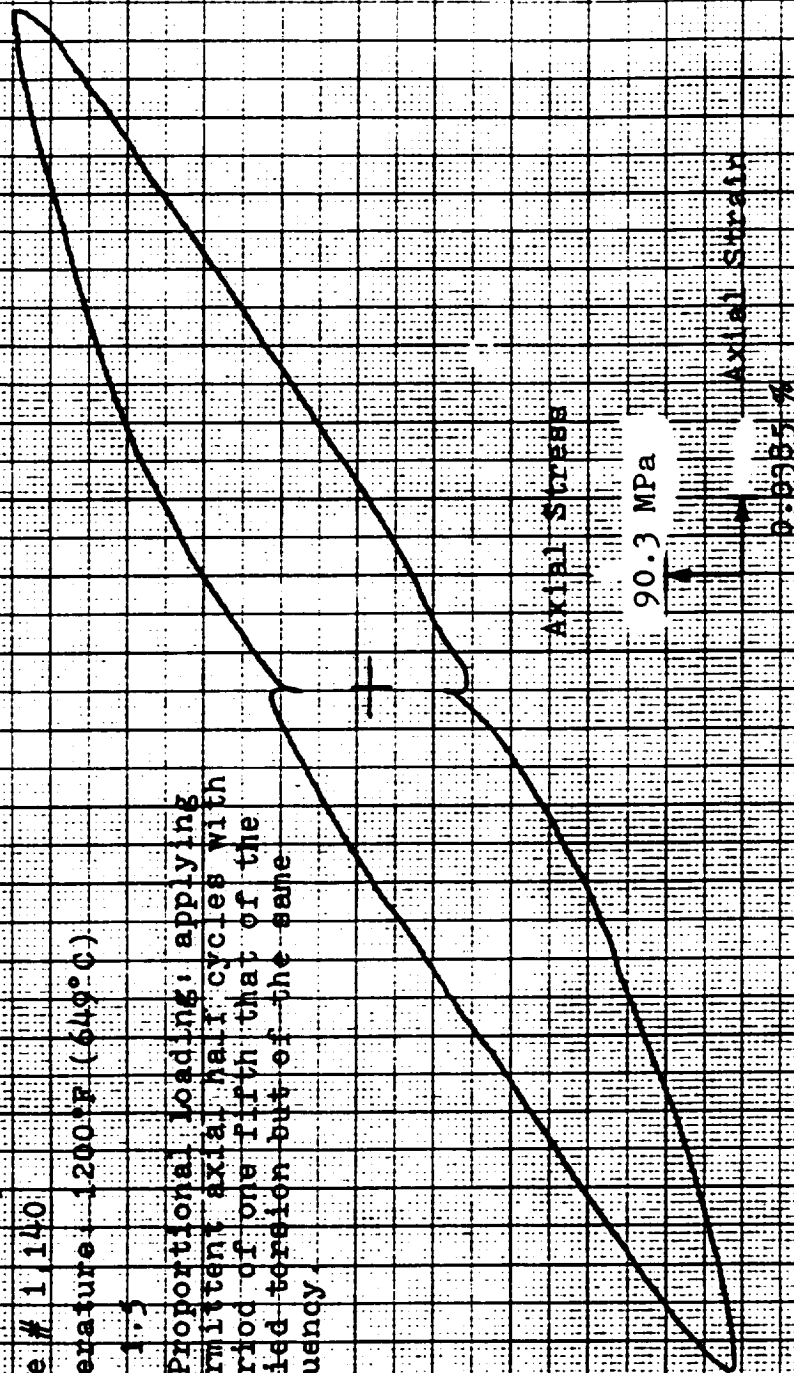


Figure 58. Axial Hysteresis Loop

Specimen No. 32

Cycle # 1.140

Temperature: 1200°F (649°C)

$\lambda = 1.5$

Non-Proportional Loading, applying
 intermittent axial half cycles with
 a period of one fifth that of the
 applied torsion but of the same
 frequency.

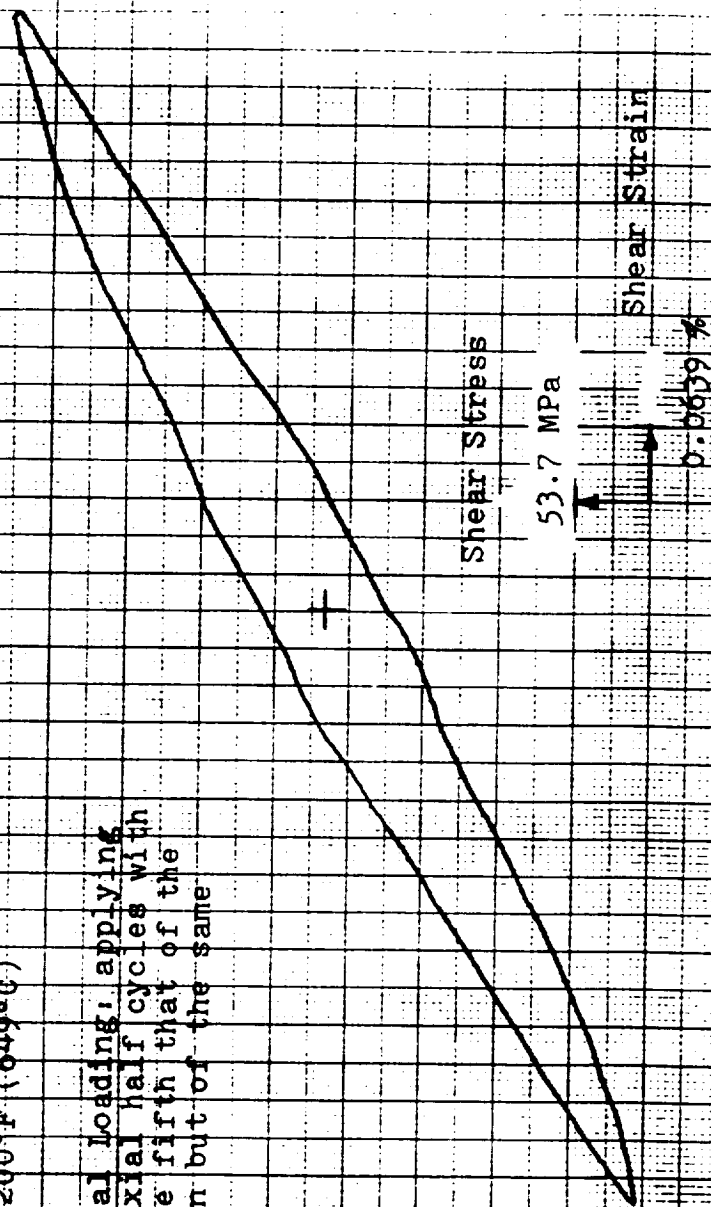


Figure 59. Torsion Hysteresis Loop

Specimen No. 8

Room Temperature

$\lambda = 0$

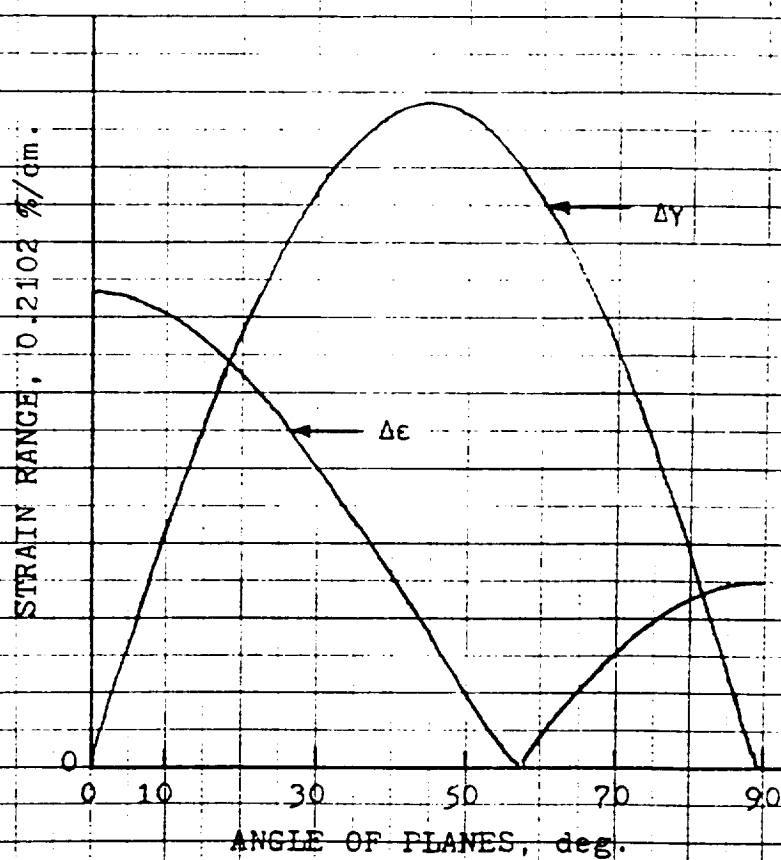


Figure 60. Shear strain range and normal strain range versus angle of planes.

Specimen No. 34

Temperature: 1200°F. (649°C)

$\lambda = 1.5$

$\phi = 0$

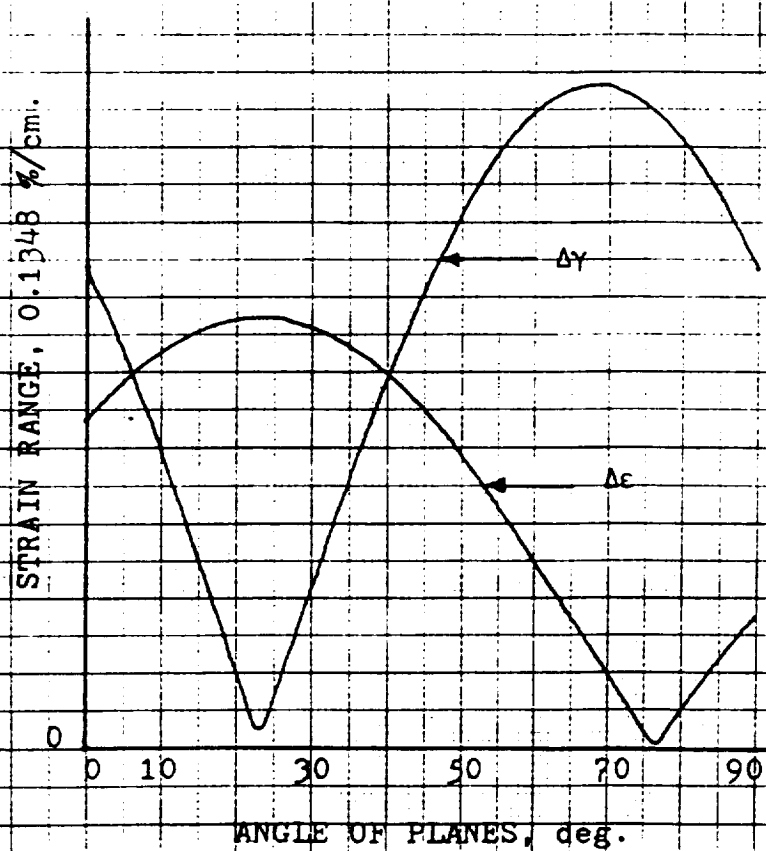


Figure 61. Shear strain range and normal strain range versus angle of planes.

Specimen No. 14

Room Temperature

$\lambda = 4$

$\phi = 0$

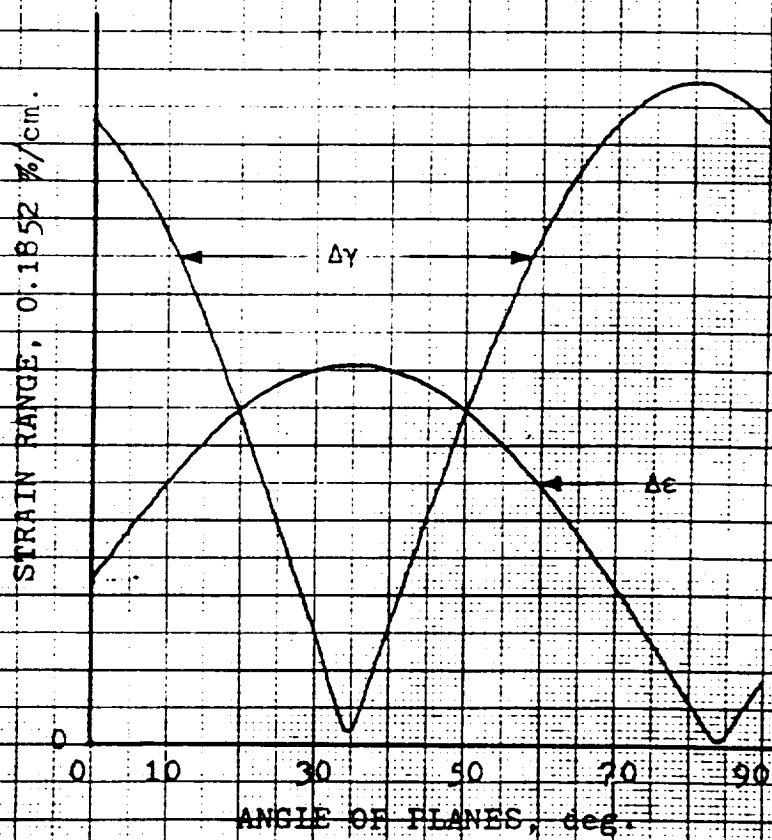


Figure 62. Shear strain range and normal strain range versus angle of planes.

Specimen No. 19

Temperature: 1200°R (649°C)

Using Band Heater

$\lambda = \infty$

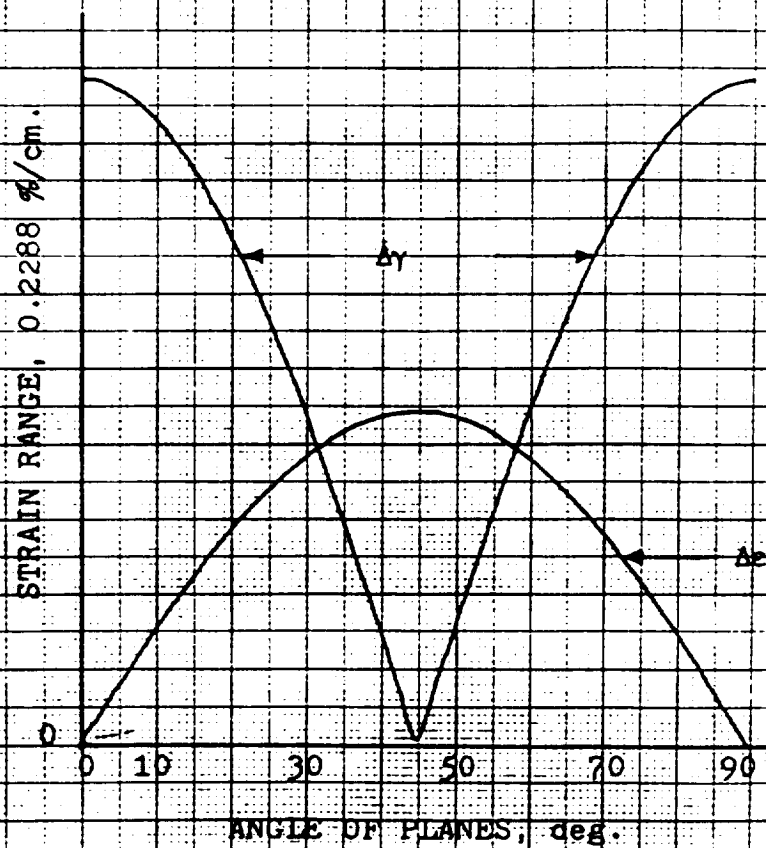


Figure 63. Shear strain range and normal strain range versus angle of planes.

Specimen No. 36

Temperature: 1200°F (649°C)

Using Induction Heater

$\lambda = \infty$

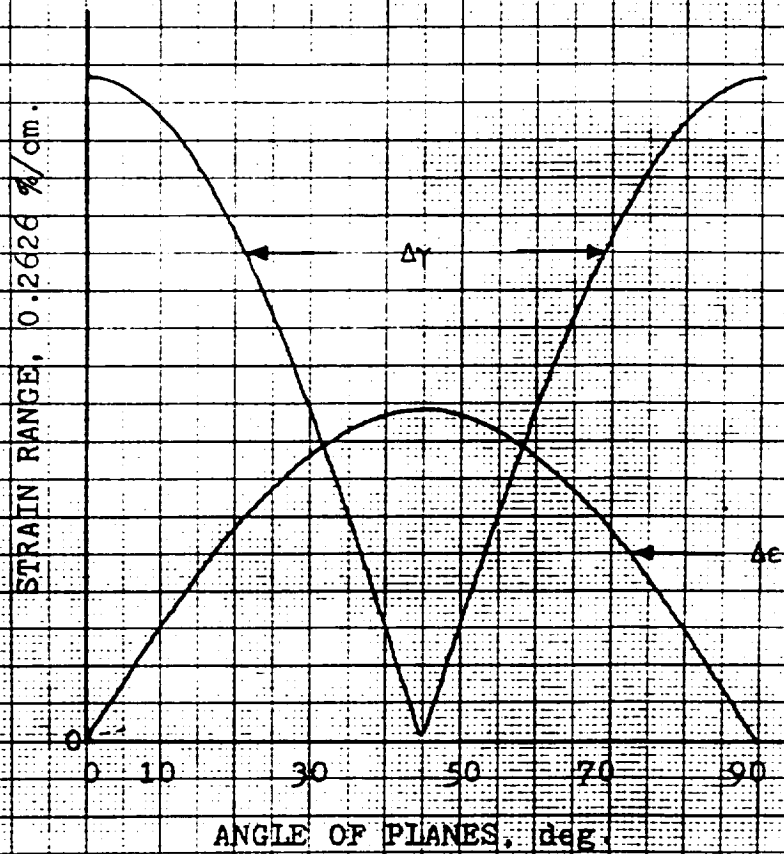


Figure 64. Shear strain range and normal strain range versus angle of planes.

Specimen No. 20

Temperature: 1200°F (649°C)

$\lambda = 1.5$

$\phi = 90^\circ$

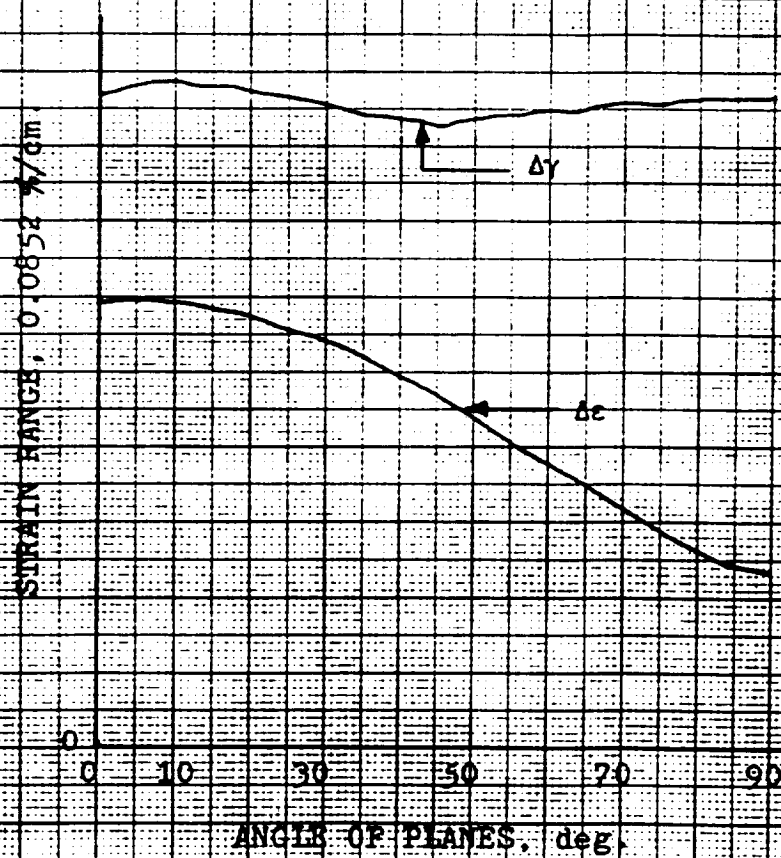


Figure 65. Shear strain range and normal strain range versus angle of planes.

Specimen No. 27

Temperature: 1200°F (649°C)

$\lambda = 1.5$

Non-Proportional Loading: consisted of alternate tension and torsion with a tensile mean stress during the torsion cycle

@ Tension Cycle

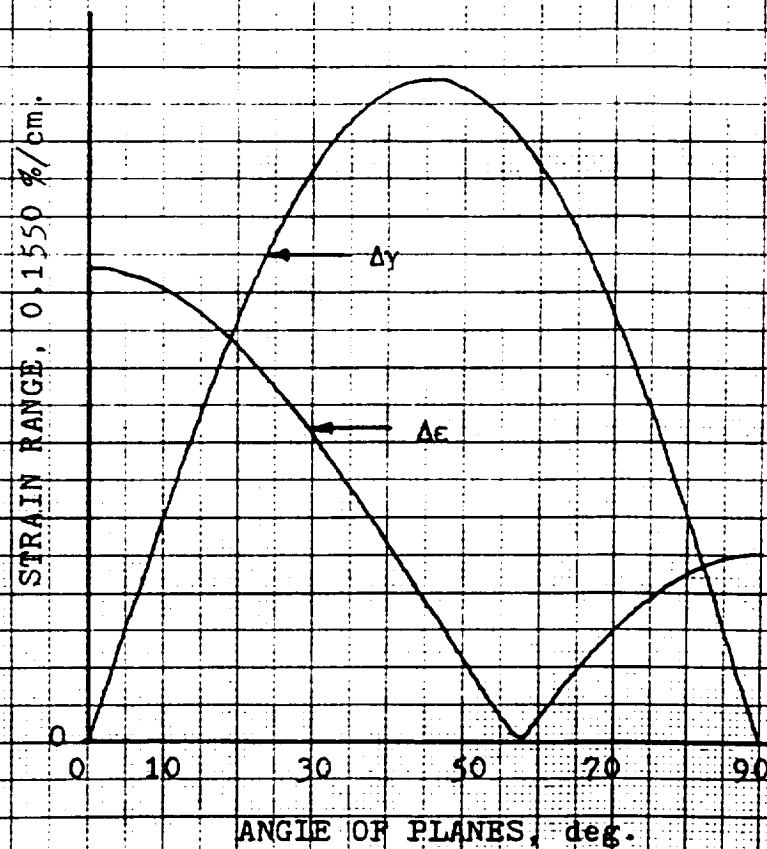


Figure 66. Shear strain range and normal strain range versus angle of planes.

Specimen No. 27

Temperature: 1200°F (649°C)

$\lambda = 1.5$

Non-Proportional Loading: consisted of alternate tension and torsion with a tensile mean stress during the torsion cycle.

@ Torsion Cycle

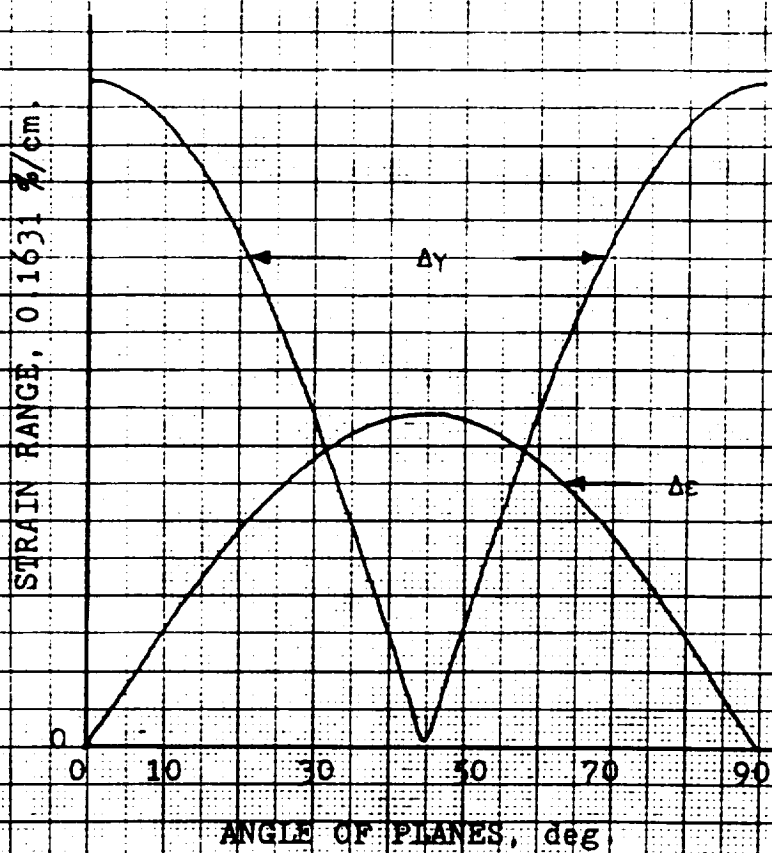


Figure 67. Shear strain range and normal strain range versus angle of planes.

Specimen No.: 28

Temperature: 1200°F (649°C)

$\lambda = 1.5$

Non-Proportional Loading: consisted of alternate tension and torsion with a compressive mean stress during the torsion cycle.

@ Tension Cycle

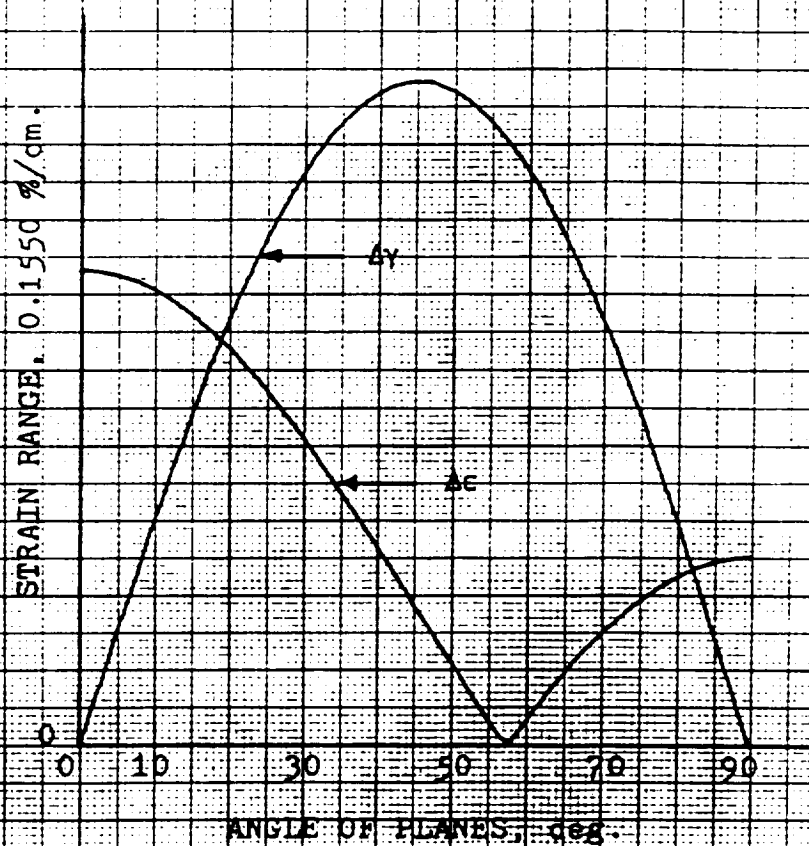


Figure 68. Shear strain range and normal strain range versus angle of planes.

Specimen No. 28

Temperature: 1200°F (649°C)

$\lambda = 1.5$

Non-Proportional Loading: consisted of alternate tension and torsion with a compressive mean stress during the torsion cycle.

@ Torsion Cycle

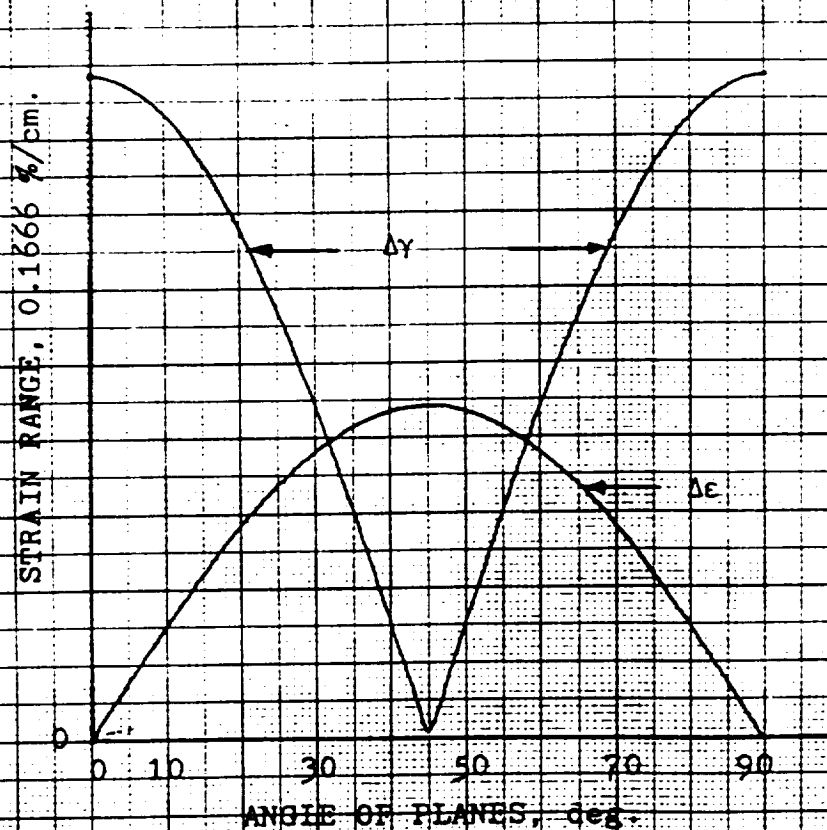


Figure 69. Shear strain range and normal strain range versus angle of planes.

Specimen No. 30

Temperature: 1200°F (649°C)

$\lambda = 1.5$

Non-Proportional Loading: applying intermittent axial half cycles with a period of one tenth that of the applied torsion but of the same frequency.

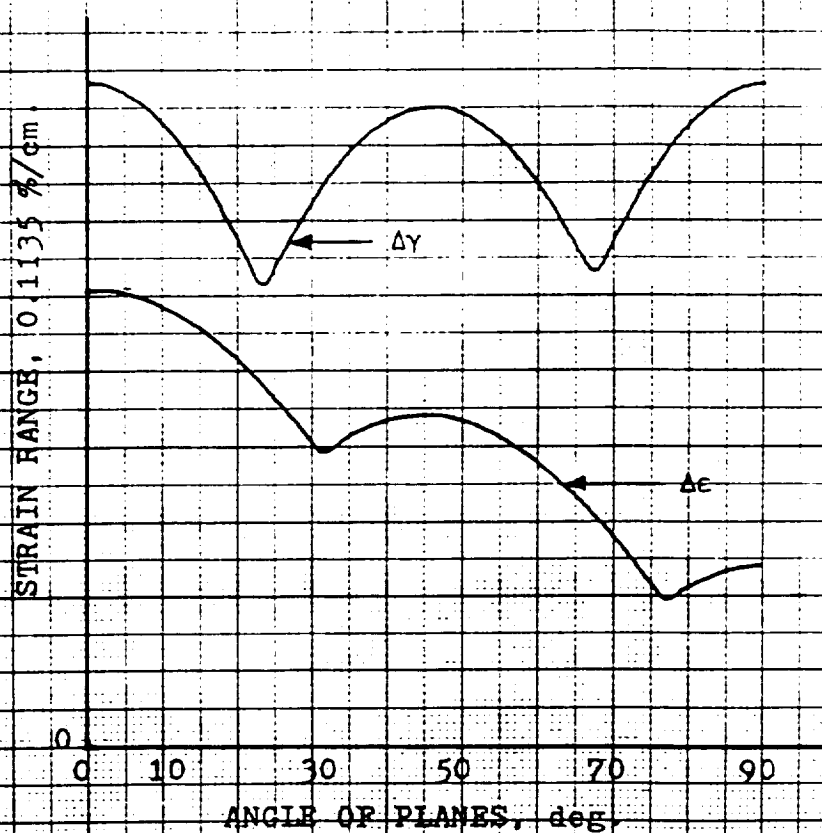


Figure 70. Shear strain range and normal strain range versus angle of planes.

Specimen No: 32

Temperature: 1200°F (649°C)

$\lambda = 1.5$

Non-Proportional Loading: applying intermittent axial half cycles with a period of one fifth that of the applied torsion but of the same frequency.

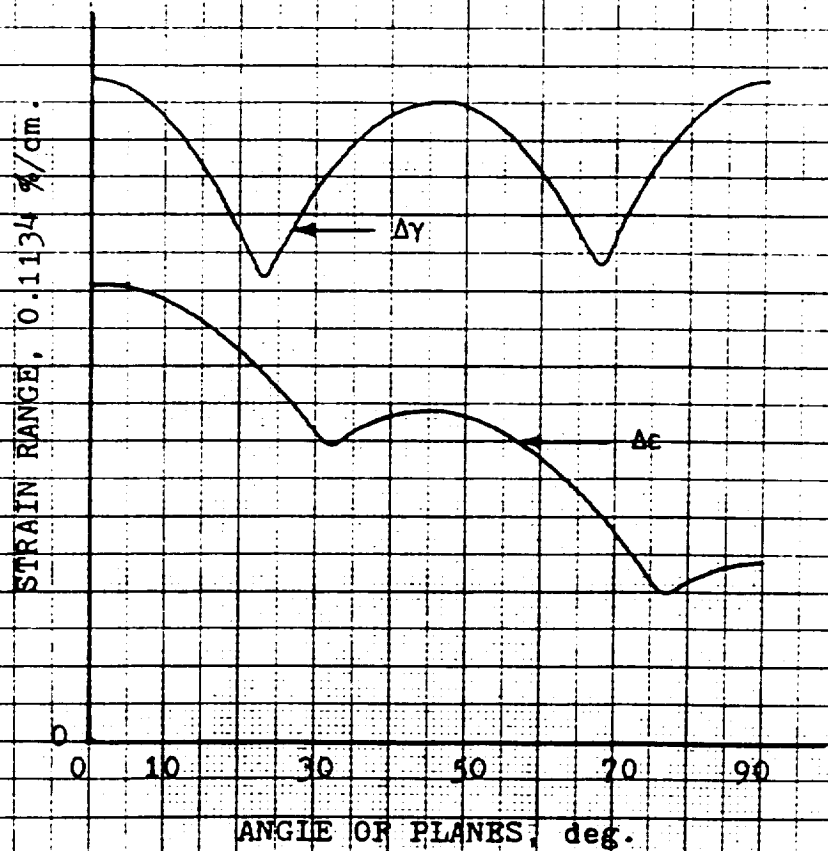


Figure 71. Shear strain range and normal strain range versus angle of planes.

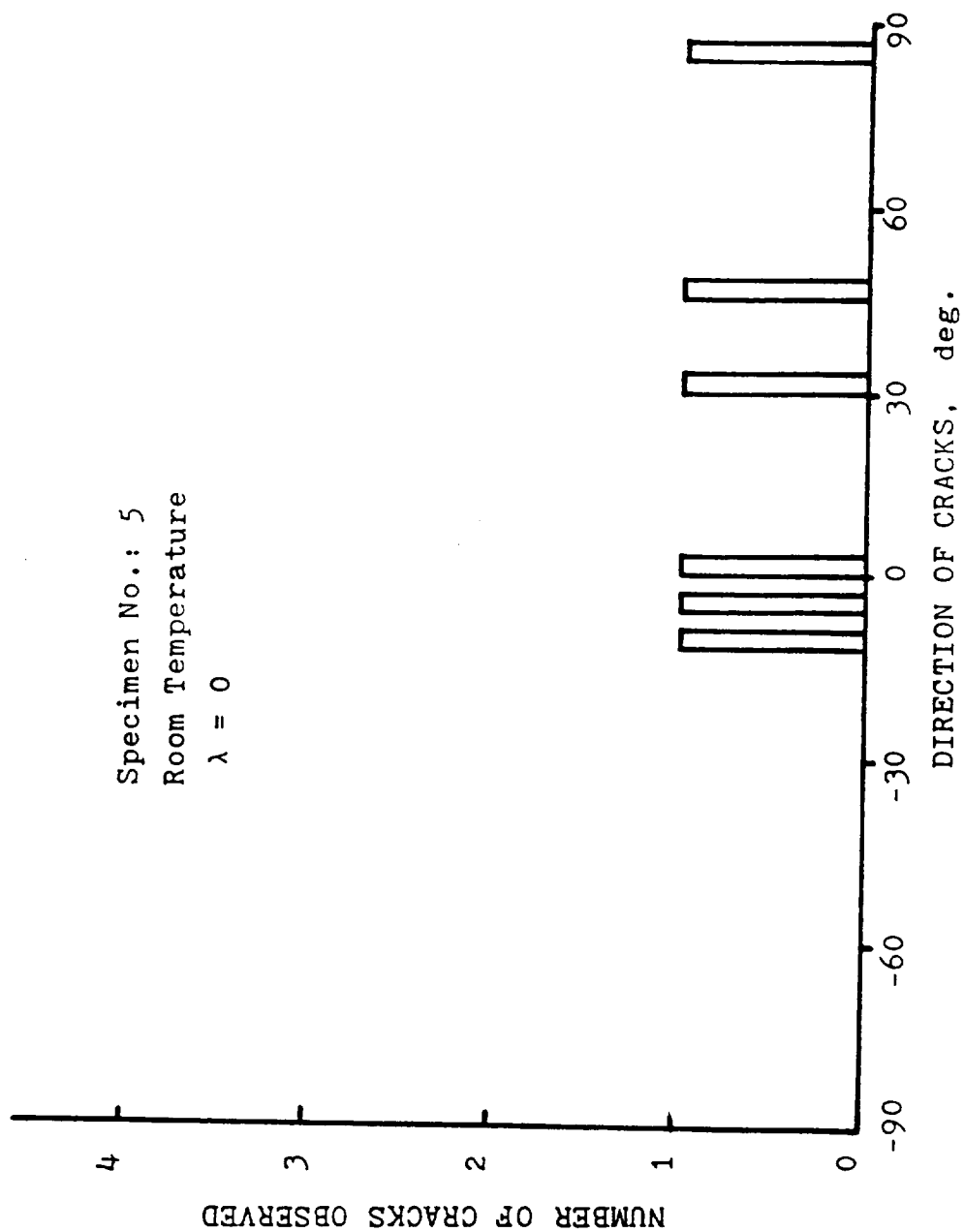


Figure 72. Distribution of crack directions

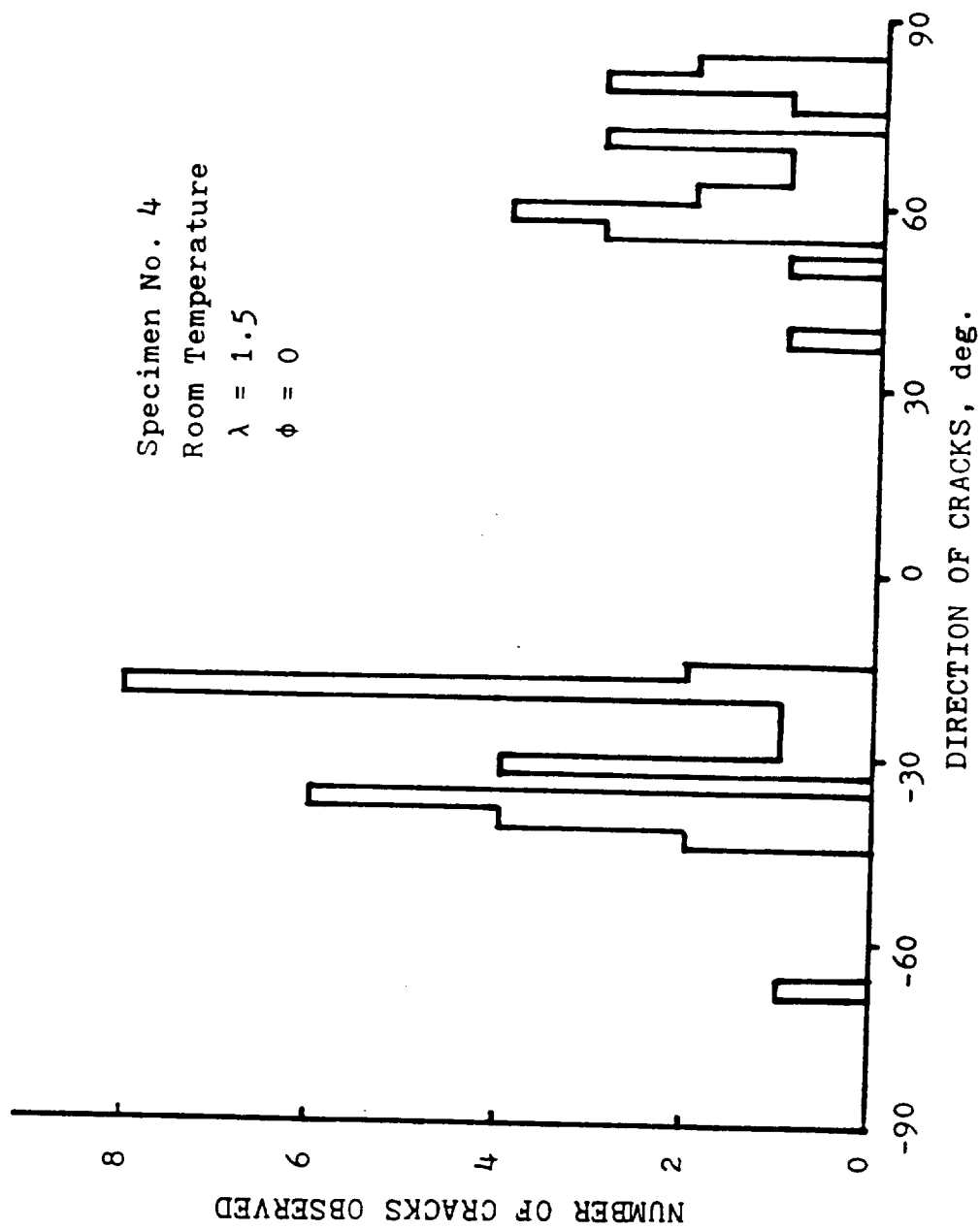


Figure 73. Distribution of crack directions

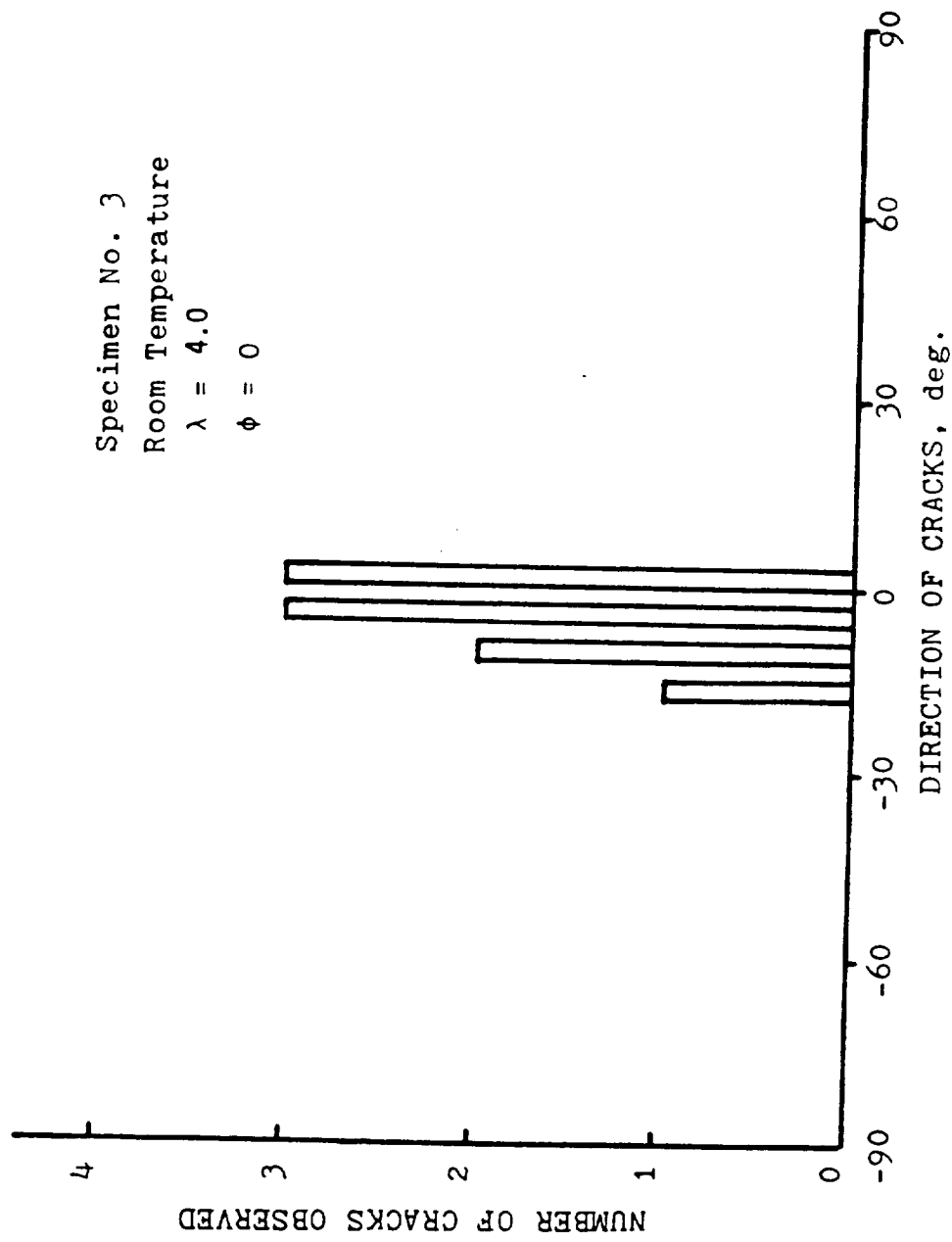


Figure 74. Distribution of crack directions

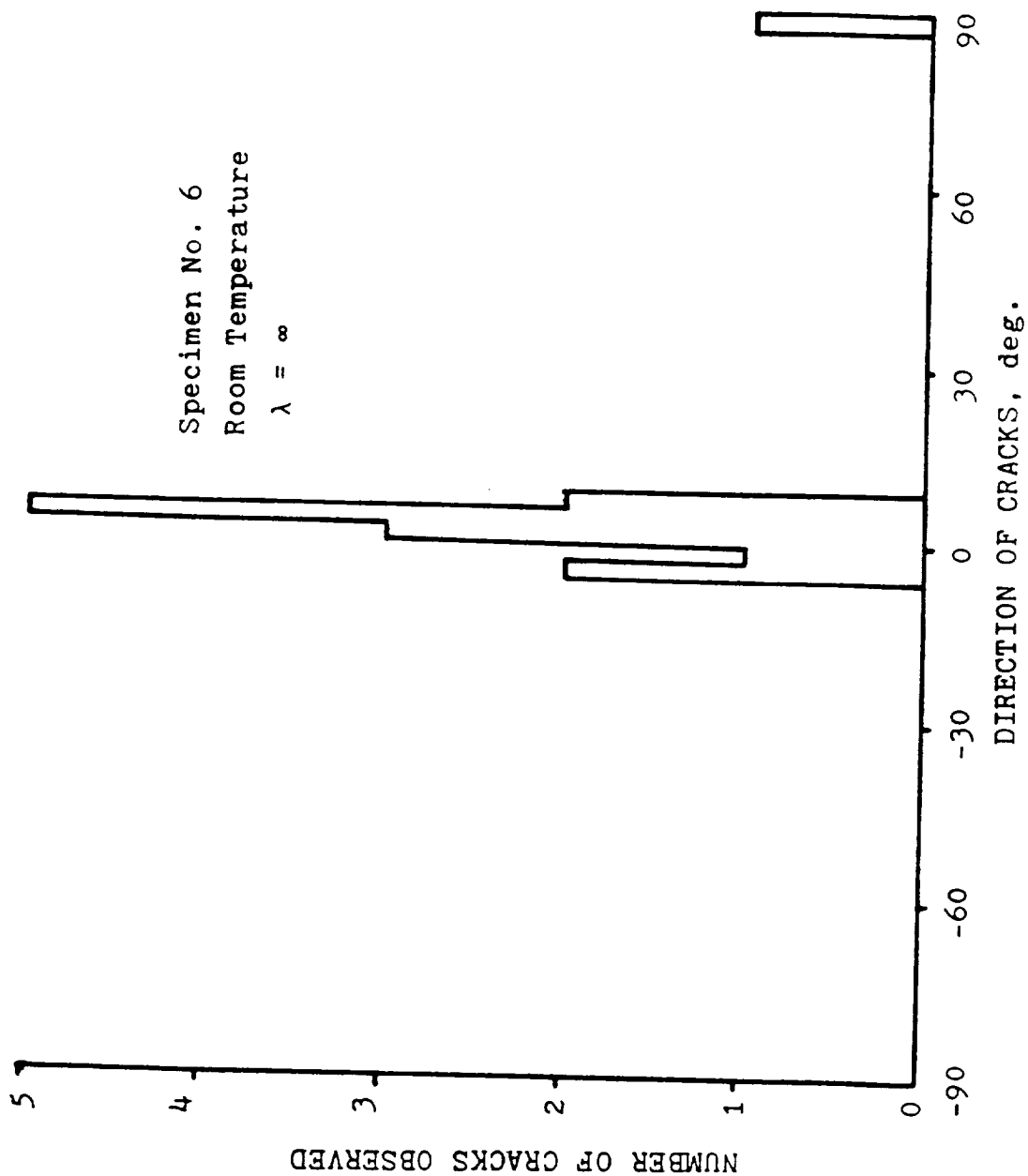


Figure 75. Distribution of crack directions

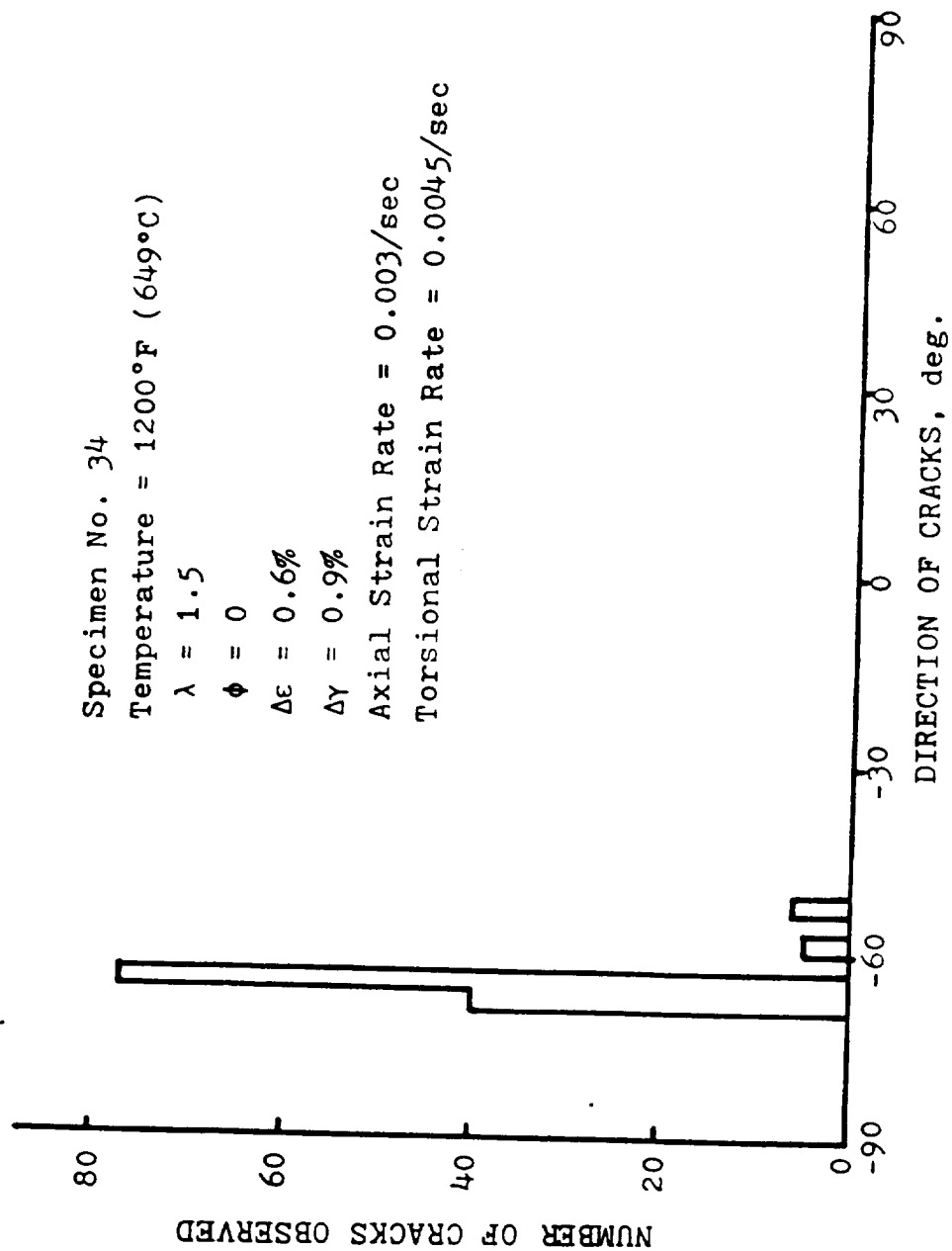


Figure 76. Distribution of crack directions

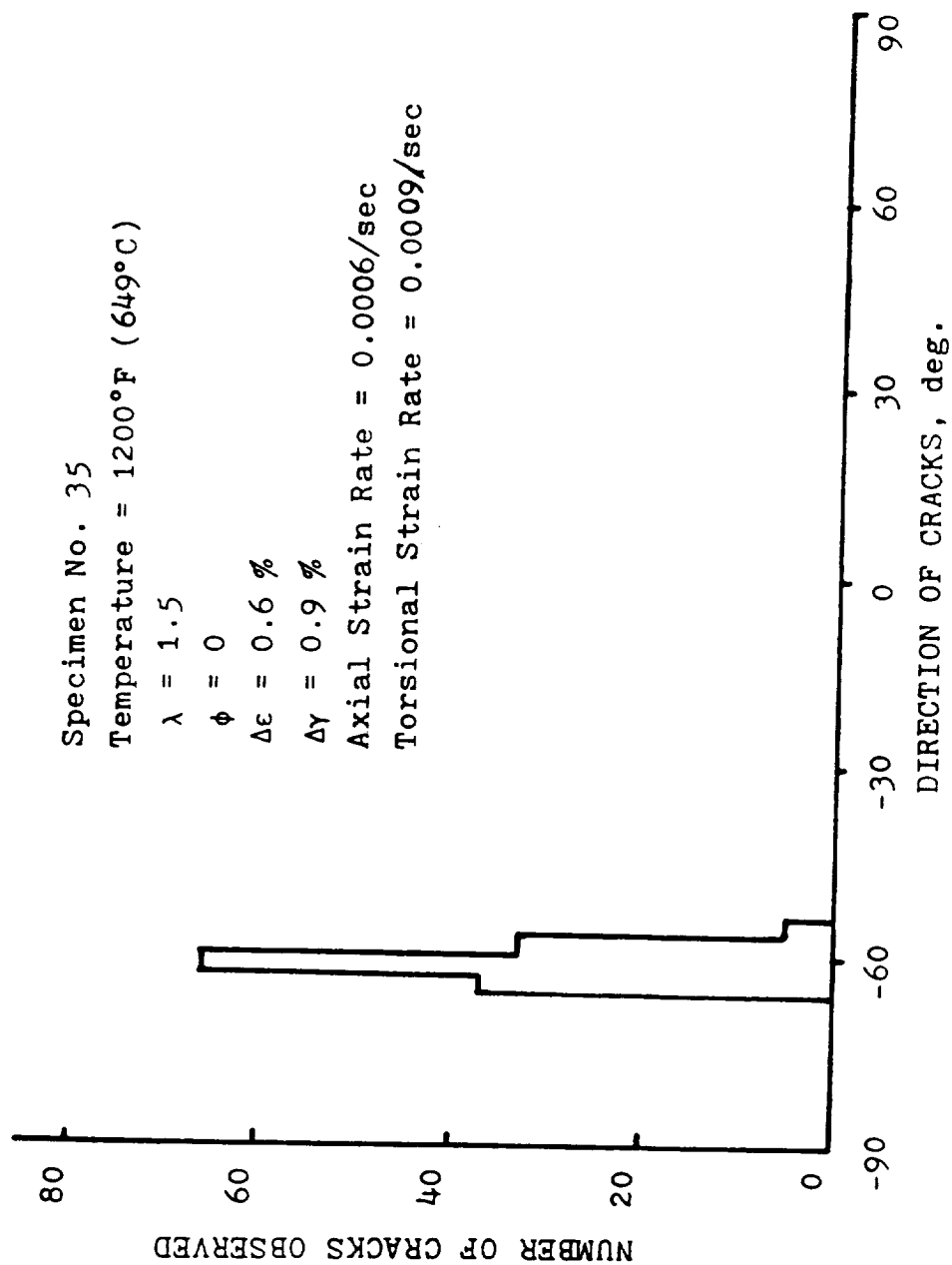


Figure 77. Distribution of crack directions

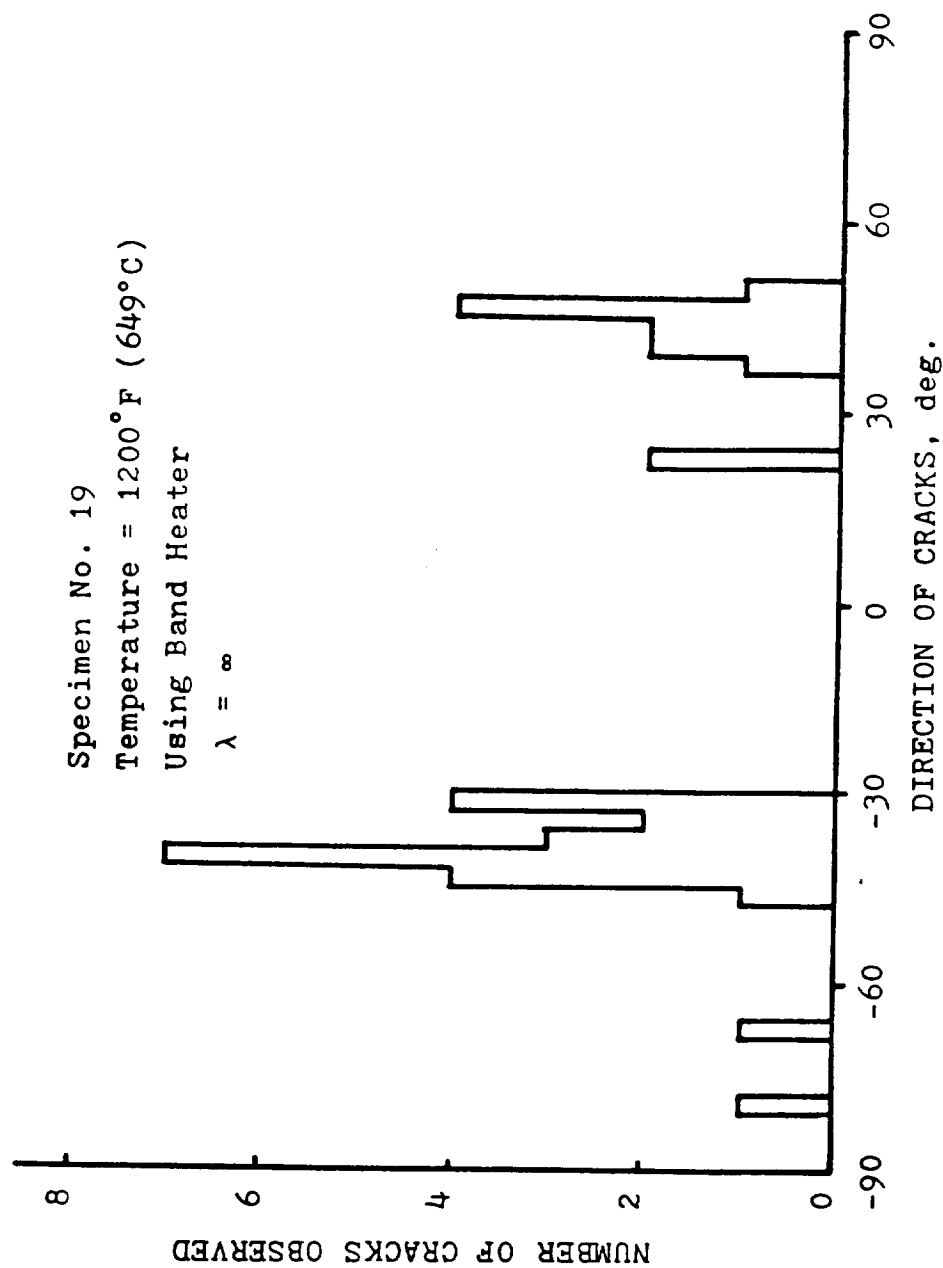


Figure 78. Distribution of crack directions

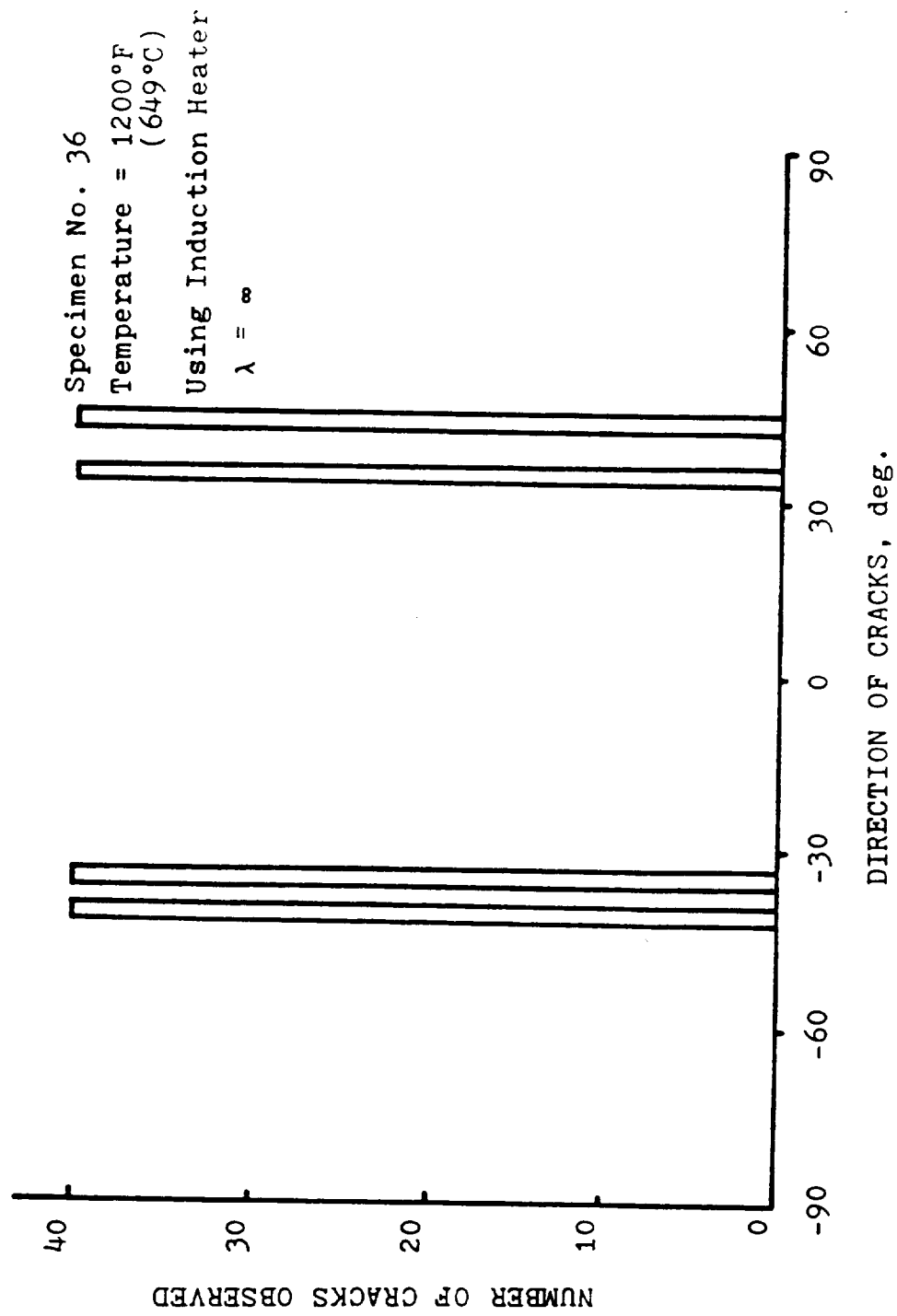


Figure 79. Distribution of crack directions

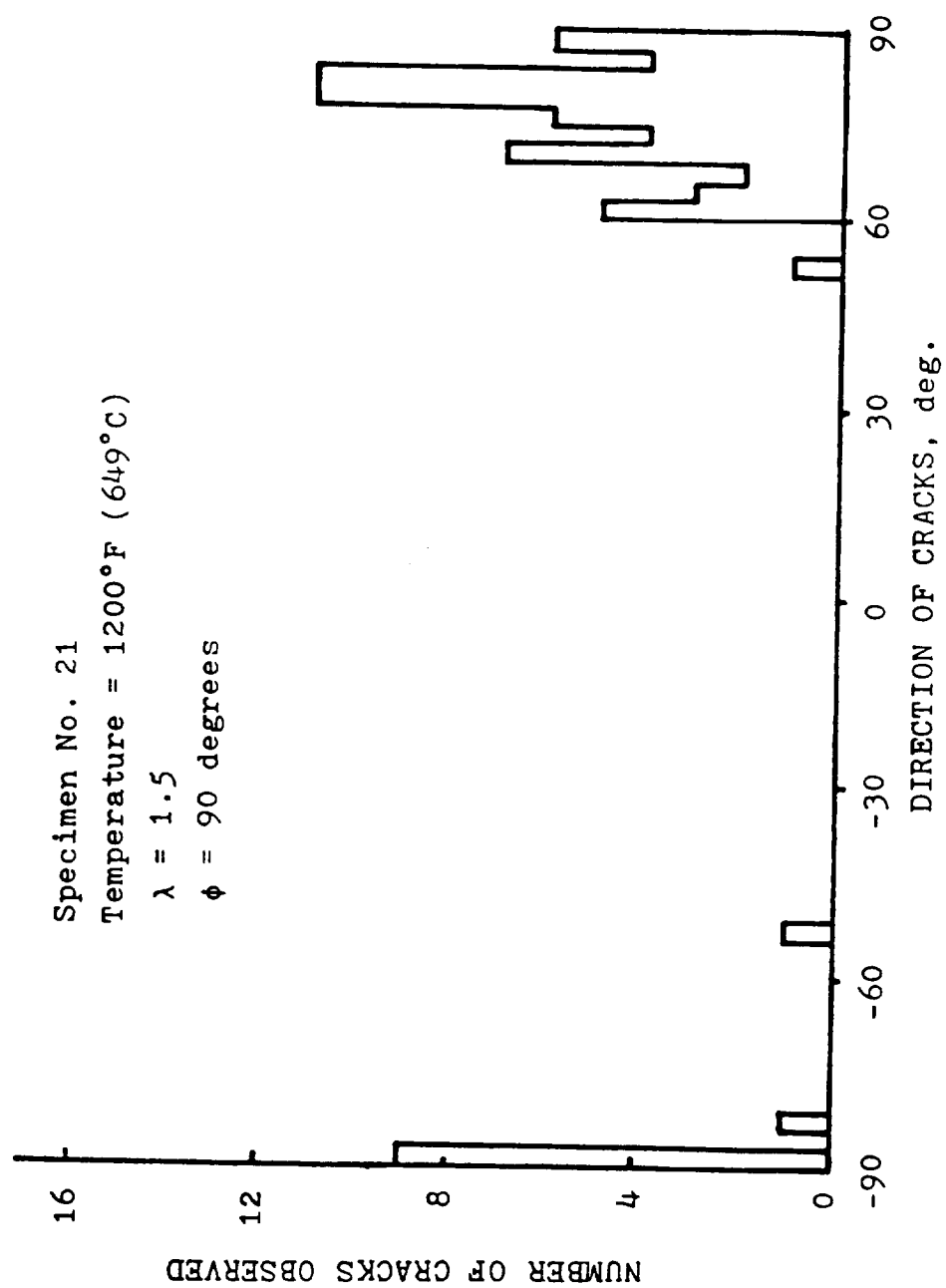


Figure 80. Distribution of crack directions

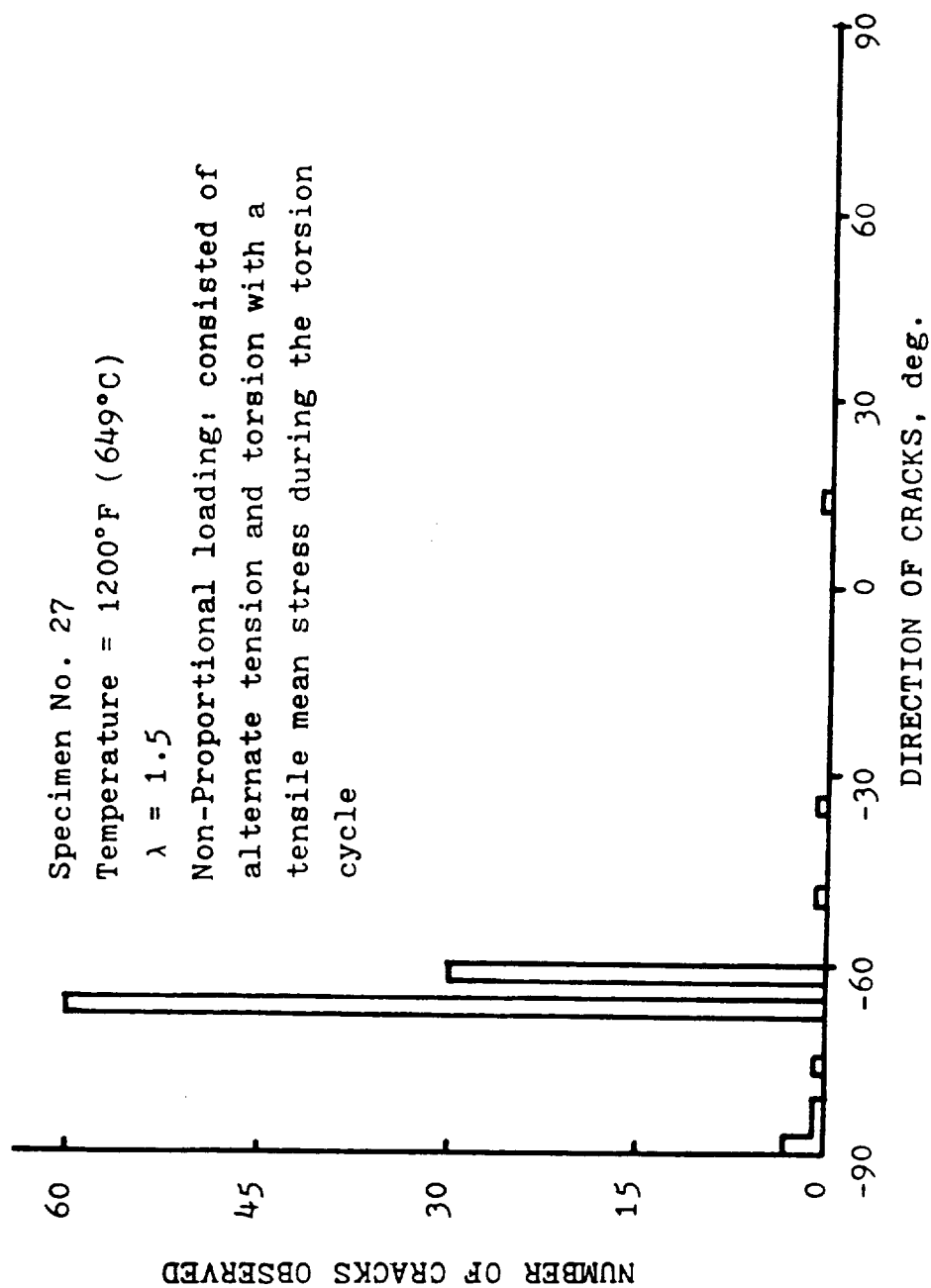


Figure 81. Distribution of crack directions

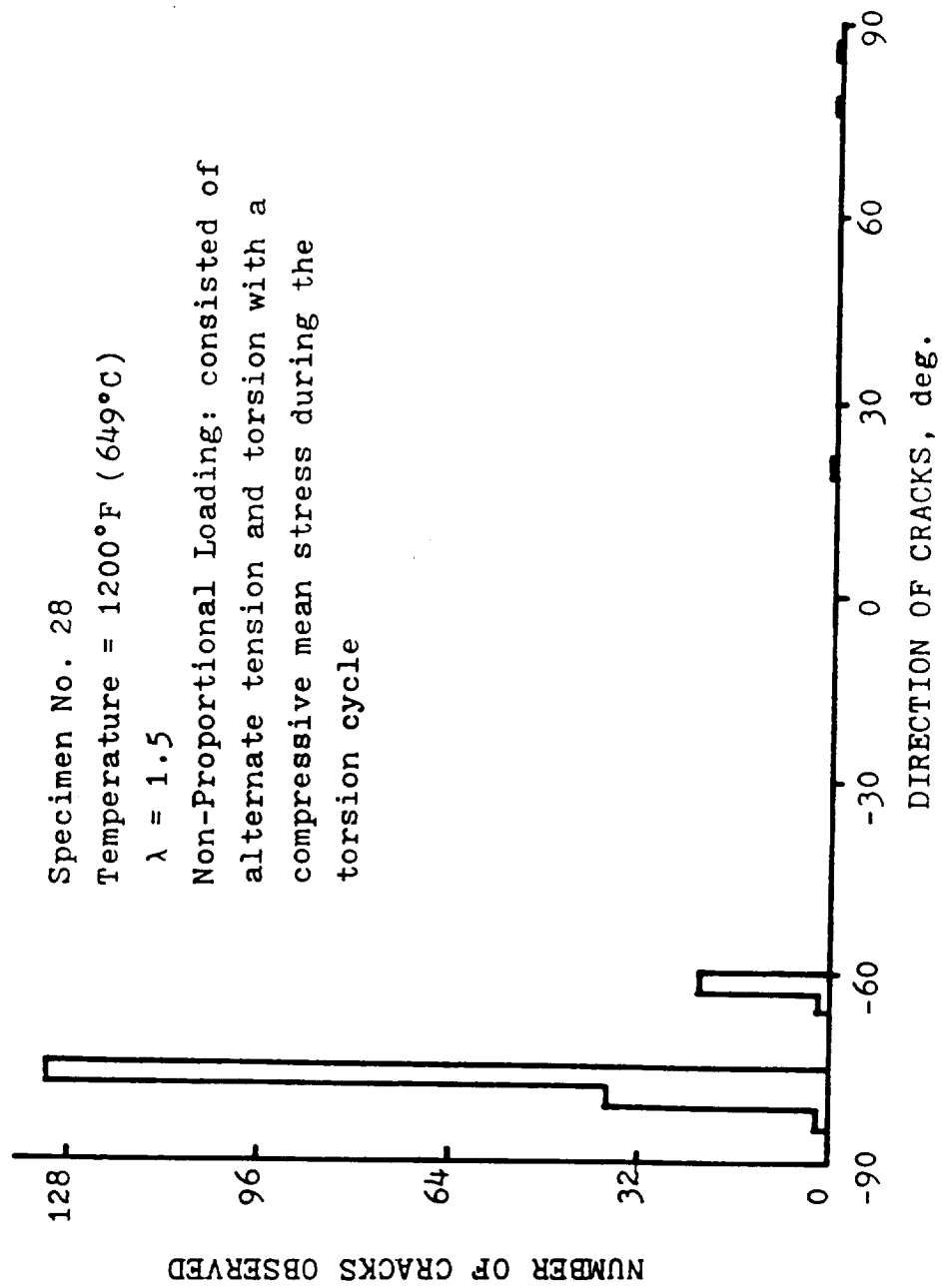


Figure 82. Distribution of crack directions

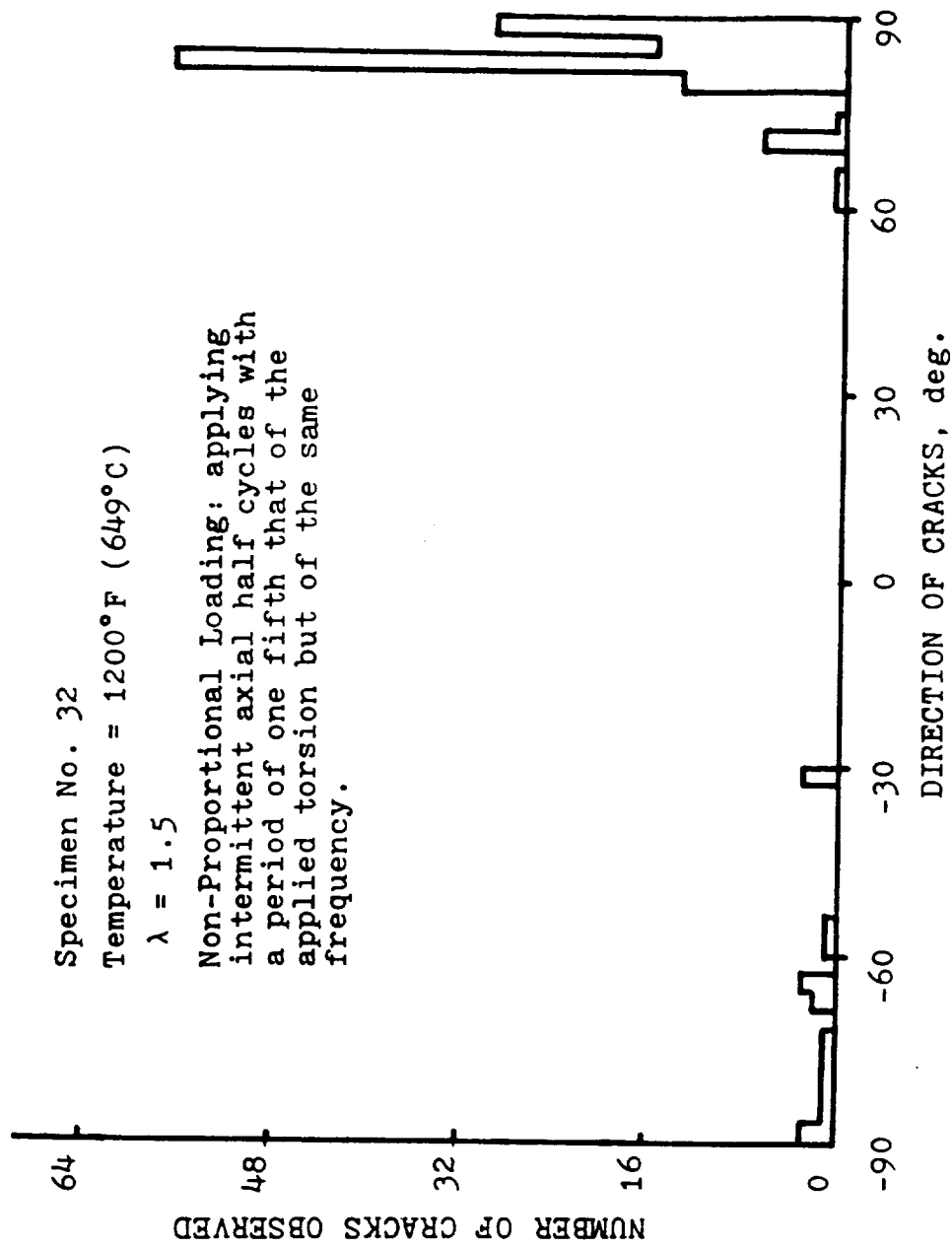


Figure 83. Distribution of crack directions

Appendix I

INTACT

Input the specimen dimension, calibration factors of load, torque and strains, limits of A/D or D/A board, form and amplitudes of the command signals and the desired cycle numbers from which the test data will be stored. This program created three data files of INTER.DAT, WAVE.DAT and FILES.DAT for running the TEST program.

TEST

Connected with the INTACT program, this is a program for generating the command signals and running the data acquisition. Enter the desired strain rate to run the fatigue tests and also monitored the torque applied to the specimen. If the torque drops too low the test will be terminated and all the data put into two kinds of data files for storage. OOSS.DT includes all the test informations and SS means the specimen number (e.g. 0032.DT). SSCC.DT contains integer data of load, torque and strains, where SS means the specimen number and CC is the cycle number (e.g. 3213).

RTEST

A modified TEST program for checking the behaviors of ring probes, only for single cycle tests.

PLAS

Compute the applied strain ratio, ranges of applied load, torque, stresses and strains, cyclic plastic work and Garud's modified cyclic plastic work.

PROC

Compute the strain parameters of fatigue life prediction, such as octahedral shear strain range, maximum shear strain range/the corresponding normal strain range on the plane of maximum shear strain, maximum plastic shear strain range and maximum normal strain range/the corresponding shear strain range on the plane of maximum normal strain.

STRESS

To calculate the stress parameters of fatigue life prediction, such as maximum principal stress range/the corresponding shear stress range to the plane of maximum principal stress range, maximum shear stress range/the corresponding normal stress range to the plane of maximum shear stress range, octahedral shear stress range/the corresponding octahedral normal stress range and the equivalent stress range.

LOHR

To calculate the Lohr-Ellison maximum shear strain range/the corresponding Lohr-Ellison normal strain range and the Lohe-Ellison parameter range.

LIFE/LEAST

To calculate the correlation coefficient of fatigue parameters for fatigue life prediction.

IN

Input and create data files for general plotting.

PLOT

Does the general plotting in the X-Y plotter.

PLOT1

Plotting: the shear strain range and normal strain range versus the angle of plane ($0^\circ - 90^\circ$).

PLOT2

Plotting: the axial strain vs. torsional strain for checking the "phase shift angle".

PLOT3

Plotting: (1) applied axial stress vs. axial strain. (2) applied shear stress vs. torsional strain for a selected cycle.

Several programs above were modified to run tests and do data reduction for some special non-proportional loading tests. XINTA, XTEST, PLAS4, PROC4, STRES4 and LOHR4 are modified versions of INTACT, TEST, PLAS, PROC, STRESS and LOHR respectively for test # 25, 27, 28 and 29. NINTA, NTEST, PLASN, PROCN, STRESN and LOHRN are modified versions of INTACT, TEST, PLAS, PROC, STRESS and LOHR respectively for test # 30, 31, 32 and 33.

Appendix II

σ : stress amplitude

ϵ : strain amplitude

τ : shear stress amplitude

γ : shear strain amplitude

$\epsilon_1, \epsilon_2, \epsilon_3$: principal strains ($\epsilon_1 \geq \epsilon_2 \geq \epsilon_3$)

$\sigma_1, \sigma_2, \sigma_3$: principal stresses ($\sigma_1 \geq \sigma_2 \geq \sigma_3$)

(a). Plastic work theory

$$\Delta W_p = \int \sigma d\epsilon_p + \int \tau d\gamma_p$$

(b). Modified plastic work theory

$$\Delta W_p^* = \int \sigma d\epsilon_p + \frac{1}{2} \int \tau d\gamma_p$$

(c). Maximum shear strain theory

$$\gamma_{\max} = \frac{\epsilon_1 - \epsilon_3}{2}$$

(d). Maximum plastic shear strain theory

$$\gamma_{\max}^p = \gamma_{\max} - \frac{\tau_{\max}}{G}$$

(e). Octahedral shear strain theory

$$\gamma_{\text{oct}} = \frac{2}{3} [(\epsilon_1 - \epsilon_2)^2 + (\epsilon_2 - \epsilon_3)^2 + (\epsilon_3 - \epsilon_1)^2]^{1/2}$$

(f). Maximum normal strain theory

$$\epsilon_1$$

(g). Gama plane theory

$$\frac{\epsilon_1 - \epsilon_3}{2} = f\left(\frac{\epsilon_1 + \epsilon_3}{2}\right)$$

for $N_f = \text{constant}$

where

$$\frac{\epsilon_1 - \epsilon_3}{2} = 1/2(\text{maximum engineering shear strain})$$

$$\frac{\epsilon_1 + \epsilon_3}{2} = \text{tensile strain on plane of maximum shear}$$

(h). Maximum principal stress theory

$$\sigma_1$$

(i). Maximum shear stress theory

$$\tau_{\max} = \frac{\sigma_1 - \sigma_3}{2}$$

(j). Octahedral shear stress theory

$$\tau_{\text{oct}} = \frac{1}{3} [(\sigma_1 - \sigma_2)^2 + (\sigma_2 - \sigma_3)^2 + (\sigma_3 - \sigma_1)^2]^{1/2}$$

(k). Lohr-Ellison's parameter

$$\text{Lohr} = \gamma^*/2 + 0.2 \epsilon_n^*$$

REFERENCES

- (1). Jordan, E.H., "Fatigue-Multi-axial Aspects", a chapter in Pressure Vessels and Piping Design Technology-1982-A Decade of Progress, eds. S.Y. Zamrik and D. Dietrich, PVP of ASME, 1982, PP. 507-518.
- (2). Brown, M.W. and Miller, K.J., "A Theory for Fatigue Failure under multi-axial stress-strain conditions.", Proceedings of the Institution of Mechanical Engineers, Vol. 187 65/73, 1973, PP. 745-755.
- (3). Garud, T.S., "Multi-Axial Fatigue: A Survey of the State of The Art," Submitted to ASTM for publication.
- (4). Havard, D.G. and Topper, T.H., "A Criterion for Biaxial Fatigue of Mild Steel at Low Cycle Fatigue," Proceeding of the First International Conference on Material, ASME, New York, 1968, pp. 551-562
- (5). Findley, W.N., "A Theory for the Effect of Mean Stress on Fatigue of Metals under Combined Torsion and Axial Load or Bending," J. of Engineering Industry, Transactions of ASME, Ser. B., Vol. 81, 1959, pp. 301-306. Cited by Kanazawa, K., Miller, K. J. and Brown, M.W., "Low-Cycle Fatigue under Out-of-Phase Loading Condition," Transaction of the ASME, Ser. H., J. of Engineering Materials and Technology, Vol. 99, July 1977, pp. 222-228.
- (6). Taira, S., Inoue, T. and Yoshida, T., "Low Cycle Fatigue Under Multi-axial stresses (in the case of Combined Cyclic Tension-Compression and Cyclic Torsion Out-of-Phase at Elevated Temperature)," Proceedings of the 11th Japan Congress on Materials Research, 1968, pp. 60-65.
- (7). Kanazawa, K., Miller, K.J. and Brown, M.W., "Low Cycle Fatigue under Out-of-Phase Loading Condition," Transactions of the ASME, Ser. H. J. of Engineering Materials and Technology, Vol. 99, July 1977, 222-228.
- (8). Garud, Y. S., "A New Approach to the Evaluation of Fatigue under Multi-Axial Loadings," Proceedings of the Symposium on Methods for Predicting Materials Life in Fatigue, Ostergren, W.J. and Whitehead, J.R., Eds., New York, pp. 113-125.
- (9). Gross, J.H. and Stout, R.D. (1955) Plastic fatigue properties of high strength pressure vessel steels. Weld. J. Lond. 34, Research Supplement, 161.
- (10). McLaren, S.W. and Terry, E.L. (1963) Characteristics of aerospace material subjected to biaxial static and fatigue loading conditions. ASME publ. 63-WA-315, 1963

(11). Pascoe, K.J. and de Villier, J.W.R. (1967) Low cycle fatigue of steels under biaxial straining. J. Strain Analysis 2, 117.

(12). Parsons, M.W. and Pascoe, K.J. (1974) Low cycle fatigue under biaxial stress. Proc. Instn mech. Engrs 188, 657.

(13). Miller, K.J. (1977) Fatigue under complex stress. Metal Sci. 432.

(14). Frost, N.E. and Sharples, J.K., "The Prediction of the Fatigue Behavior of Cylinders Subjected to a Repeated Internal Fluid Pressure", Engineering Fracture Mechanics, Vol. 10. 1978, pp. 371-379.

(15). Joshi, S.R. and Shewchuk, J., "Fatigue-Crack Propagation in a Biaxial-Stress Field," Experimental Mechanics, Vol. 10, No. 12 1970, pp. 529-533.

(16). Tanaka, K., Hoshide, T., Yamada, A., and Taira, S., "Fatigue Crack Propagation in Biaxial Stress Fields," Fatigue of Engineering Materials and Structures, Vol. 2, pp. 181-194.

(17). Plumbridge, W.J. (1972) Review: Fatigue-crack propagation in metallic and polymeric materials. J. Mater. Sci. 7, 939.

(18). Blass, J. J., "Multiaxial Creep and Fatigue Damage Estimation for Type 304 Stainless Steel," Oak Ridge National Report, ORNL/PM-6438.

(19). Brown, M. W. and Miller, K. J., "A Biaxial Fatigue Machine for Elevated Temperature Testing," J. of Testing and Evaluation, JTEVA, Vol. 9, No. 4, July 1981, pp. 202-208.

(20). Kanazawa, K., Miller, K. J. and Brown M. W., "Low-Cycle Fatigue Under Out-of-Phase Loading Conditions," J. of Engineering Materials and Technology, July 1977, pp. 222-228.

(21). Wood, W., "Yield and Second-order Effects Induced by Cyclic Strain in Copper Under Tension," Acta Metallurgical, Vol. 15, May 1967, pp. 841-846.

(22). Lohr, R. D. and Ellison, E. G., "A Simple Theory for Low Cycle Multiaxial Fatigue," Fatigue of Engineering Material and Structures Vol. 3, pp. 1-17.

(23). Zamrik, S. Y. (1967), "An Investigation of Strain Cycling Behavior of 7075-T6 Aluminium Under Combined State of Strain," Third annual progress report, Pennsylvania State University.

(24). Jordan, E. H., Brown, M. W. and Miller, K. J., "Fatigue Under Severe Non-proportional Loading," American Society for Testing and Evaluation, STP 853, pp. - 585.

(25). Kaufman A., "Evaluation of Inelastic constitutive models for nonlinear structural analysis," NASA conference publication # 2271 Nonlinear Constitutive Relations for High Temperature Applications, 1983, pp. 89-105.

(26). Reuchet, J. and Remy, L., Jan. 1983, "Fatigue Oxidation Interaction in a Superalloy-Application to Life Prediction in High Temperature Low Cycle Fatigue", Metallurgical Transactions A, Vol. 14A, pp. 141-148.

(27). Reuchet, J. and Remy, L., 1983, "High Temperature Low Cycle Fatigue of MAR-M 509 Superalloy I and II, Materials Science and Engineering, pp. 19-32 and 33-41.

1. Report No. NASA CR-175009		2. Government Accession No.		3. Recipient's Catalog No.	
4. Title and Subtitle Elevated Temperature Biaxial Fatigue				5. Report Date October 1985	
				6. Performing Organization Code	
7. Author(s) Eric H. Jordan				8. Performing Organization Report No. None	
				10. Work Unit No.	
9. Performing Organization Name and Address School of Engineering University of Connecticut Storrs, Connecticut 06268				11. Contract or Grant No. NAS 3-160	
				13. Type of Report and Period Covered Contractor Report	
12. Sponsoring Agency Name and Address National Aeronautics and Space Administration Washington, D.C. 20546				14. Sponsoring Agency Code 505-63-11	
15. Supplementary Notes Final report. Project Manager, Albert Kaufman, Structures Division, NASA Lewis Research Center, Cleveland, Ohio 44135.					
16. Abstract A 3-year experimental program for studying elevated temperature biaxial fatigue of a nickel-based alloy Hastelloy-X has been completed. A new high-temperature fatigue test facility with unique capabilities has been developed. Effort was directed toward understanding multiaxial fatigue and correlating the experimental data to the existing theories of fatigue failure. The difficult task of predicting fatigue lives for nonproportional loading was used as an ultimate test for various life prediction methods being considered. The primary means of reaching improved understanding were through several critical nonproportional loading experiments. The direction of cracking observed on failed specimens was also recorded and used to guide the development of the theory. Cyclic deformation responses were permanently recorded digitally during each test. This constitutive data is now being used for constitutive modeling studies by a colleague at another institution and will contribute to our understanding of the constitutive response of this material. It was discovered that the cracking mode switched from primarily cracking on the maximum shear planes at room temperature to cracking on the maximum normal strain planes at 649 °C. In contrast to some other metals, loading path in nonproportional loading had little effect on fatigue lives. Strain rate had a small effect on fatigue lives at 649 °C. Of the various correlating parameters the modified plastic work and octahedral shear stress were the most successful.					
17. Key Words (Suggested by Author(s)) Multiaxial testing; Biaxial fatigue; Structures			18. Distribution Statement Unclassified - unlimited STAR Category 39		
19. Security Classif. (of this report) Unclassified	20. Security Classif. (of this page) Unclassified		21. No. of pages 161	22. Price* A08	

